Institut für Kern und Teilchenphysik

Fakultät Matematik und Naturwissenschaften

Technische Universität Dresden

A High-Resolution Time-of-Flight Spectrometer for Fission Fragments and Ion Beams

Dissertation
zur Erlangung des
Doktorgrades der Naturwissenschaften
(Doctor rerum naturalium)

vorgelegt von
Krasimir Milchev Kosev
geboren am 26. August 1975 in Gorna Oriahovica, Bulgarien

Dresden 2007

Eingereicht am 12. December 2007

1. Gutachter: Prof. Dr. E. Grosse

2. Gutachter: Doz. Dr. Kai Thomas Brinkmann

3. Gutachter: Prof. Lars Westerberg

Verteidigt am 31. Juli 2008

Contents

Chapter 1

Introduction and motivation

Most of the heavy elements are thought to be created by the rapid capture of a series of neutrons in type-II supernovae (see Fig. 1.1) in the presence of an enormous neutron flux for a very short period of time. This process is known as r-process. The r-process pathway lies far from the line of stable nuclei. Once the neutron flux has declined, the nuclei far from the line of stability approach to the heavy nuclei on the stability line by a series of β decays. Therefore, the β-decay process is considered to play a decisive role in the production rate of nuclei in the universe.

A quantitative understanding of the nucleosynthesis process requires the knowledge of the production rates, the masses and the β-decay characteristics of the exotic nuclei. The spectroscopic data of such nuclei can provide valuable information on their structure. That is important for the various theoretical models used for the precise estimate of the stellar processes of the nucleosynthesis.

Figure 1.1: The brightest star in the picture is the supernova 1987A in the Large Magellanic Cloud (LMC). It was discovered in February 1987 and is the first supernova visible to the unaided eye for the last 400 years.

Nuclear fission turns out to be a convenient way of producing neutron-rich nuclei with masses from 60 - 150. This process nearly preserves the neutron-to-proton ratio of the fissioning nuclei. That is because the emitted neutrons can carry off energy from the fragment but almost no angular momentum. Therefore, even if the fragment excitation energy is larger than the neu-

tron binding energy, the probability for neutron decay becomes even lower than that for γ-ray emission due to the relatively large spin of the fragments [Cyri91]. If we consider fissioning of ^{238}U with a neutron-to-proton ratio approximating 1.59, then the fission products are also likely to have similar neutron-to-proton ratios, which is too high for nuclei near the middle of the mass range (1.3 - 1.4 typically). The so formed neutron-rich nuclei are highly unstable and can undergo a chain of β decays until they reach the valley of stability.
An example photo-fission yield picture of ^{238}U is given in Fig. 1.2.

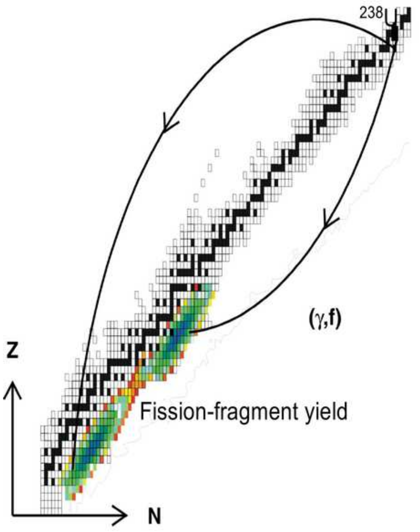

Figure 1.2: Photo-fission yield of ^{238}U. The fissile products are neutron rich exotic nuclei which tend to reach the line of stability by a series of β decays.

For better understanding the fission process it is helpful to look at its time scale as presented in Fig. 1.3.

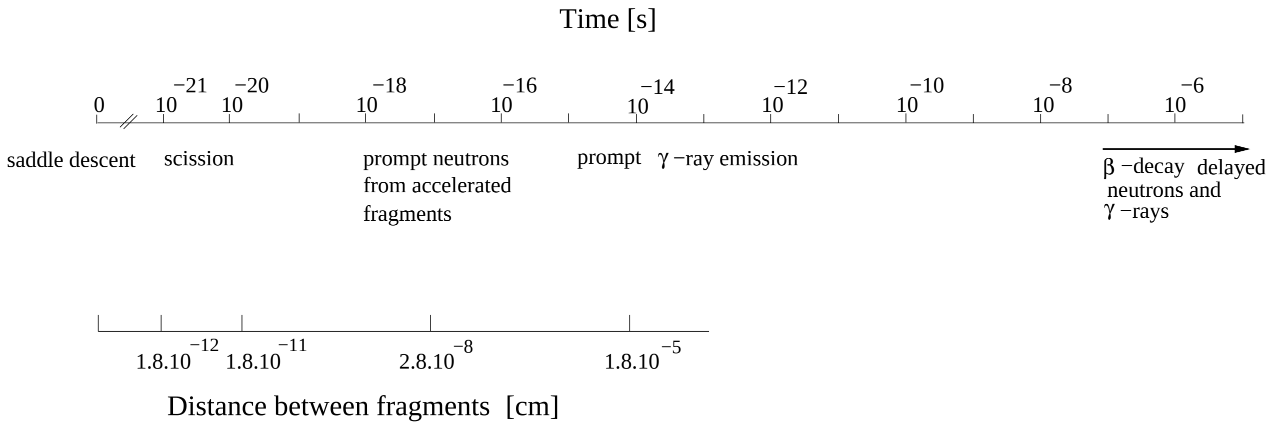

Figure 1.3: Time scale in fission after [Cyri91].

The total kinetic energy released in binary low-energy nuclear fission is in the order of 180-240 MeV, depending on the fissioning system [Cyri91]. This energy is distributed between the total kinetic energy of the two fission fragments, the energy released by neutron and γ-ray emission, and lastly by the β decay or electron conversion accompanied by the delayed emission of neutrons and γ-rays. A fraction of about 8 % of the total available energy is released in the β-decay and subsequent delayed γ-ray and neutron emission. The rest - 75 to 85 % is distributed as fragment kinetic energy. Only 10 % and 3 to 4 % are left for the prompt neutron and γ-ray emission processes, respectively.

The exact fission mechanism is detailed discussed in references like [Cyri91]. Here, we will only mention that after the prompt neutron and γ-ray emission, the fragments are β-active and will decay via β-decay chains with half-lives between microseconds and days. Such decays are accompanied by delayed neutron and γ-ray emission as well.

Neutron-rich nuclei close to the r-process path can be produced via photo-fission at the Rossendorf superconducting electron linear accelerator of high brilliance and low emittance (ELBE) [Shar02a]. Another way to produce, identify and study nuclei far from stability is by means of nuclear reactions at relativistic energies. The R^3B collaboration within the FAIR project [Fair06] at GSI aims to study a wide class of such reactions. If the fission products are identified and their charge numbers also obtained, it will be principally possible to investigate their nuclear structure by means of beta-gamma spectroscopy. The fission time scale from Fig.1.3 implies that for the purpose of the fission mass fragment identification, the Time-of-Flight (TOF) method is convenient. Such studies necessitate an unambiguous mass separation over a wide energy range for relatively small reaction cross sections. Therefore, the detecting system must have large solid angle and good time resolution. Further, such system has to be compact and withstand high counting rates. Experiments of this type are planned on the basis of a sophisticated TOF spectrometer developed at FZ Dresden-Rossendorf.

In the past, considerable efforts have been made towards constructing TOF systems incorporating multichannel-plate (MCP) detectors, suitable for mass identification studies. The advantage of these detectors is that they are fast and offer optimum time resolution.

G.D'Erasmo and co-workers [Eras85] have developed in the mid-eighties of the last century a transmission time detector for low energy light ions. The operation principle of this device is based on the isochronous transport of electrons stripped from a thin carbon foil towards MCP detector (active are < 4 cm^2) after a 90° deflection off the beam axis by an electrostatic mirror. The overall TOF resolution between two such detectors has been found to be better than 200 ps (FWHM). Similar work describing the development of a compact TOF spectrometer suitable for fission studies based on MCP detectors with electrostatic mirrors is addressed by R.D. Heil *et al.* [Heil85]. Time resolution of 240 ps (FWHM) between two identical mirror detectors is reported for that particular setup. Another spectrometer system for high mass resolution studies utilising fast mirror MCP detectors is revealed in the work of H. J. Whitlow *et al.* [Whit91].

In the above described measuring setups, the stripped electrons are accelerated by applying 2-3 kV potential between a foil sitting perpendicular to the beam axis and a wire grid placed 2-5 mm away from the foil. By inclining the foil at 45° to the incident ions, the liberated electrons can be focused directly on the MCPs [Poll84]. Systems of this type, however, have the disadvantage of introducing flight path differences because of the tilted foil position.

In other TOF experiments, the thin foil remains normal to the incident ions, but the electron transport towards the MCP surface is accomplished through 180° deflection in a homogeneous magnetic field [Saro96]. Some of the achieved operational characteristics are 700 ps time resolution and nearly 100 % detection efficiency. Here, the choice of the magnetic field B is crucial, since it determines the electrons transmission time. All the above described setups were mostly optimised for timing measurements at the cost of no position information and relatively small detector active areas.

As a result of the extra technical effort, a novel photo-fission sensitive spectrometer comprised of large area MCP detectors with electrostatic mirrors and two-dimensional position-sensitive delay-line anodes, capable of providing not only precise timing, but also position information has been developed in FZ Dresden-Rossendorf. In Chapter 2 of this thesis, we will describe its construction in detail. In Chapter 4, follows a demonstration of the first spectrometer experiments performed with α-particle source. How the TOF device responds to various beams of heavy ions delivered by the 5 MV FZ Dresden-Rossendorf tandem accelerator together with some of the electron properties ejected from thin foils will be discussed in Chapter 5. Finally, in Chapter 6, we will present results from the first photo-fission experiments conducted at ELBE accelerator.

Chapter 2

Experimental setup

This chapter will give a detailed description of the fission-fragment TOF spectrometer. At first, we will shortly dwell on the planned experiments at ELBE accelerator. Since MCP detectors play a key role in this work, an overview of their properties will be given. Then we will focus on the different TOF spectrometer components and the relevant methods to optimise them.

2.1 The fission-fragment Time-of-Flight spectrometer

2.1.1 The fission-fragment coincidence setup

Theoretical calculations by Fan [Fan01] have shown the possibility of producing neutron-rich, close to the r-process path exotic nuclei via bremsstrahlung-induced fission of ^{238}U at ELBE accelerator built at the site of Forschungszentrum Rossendorf. The challenging task is to detect low-energy fission fragments (FFs) of approximately 1 MeV/A each with the highest attainable mass and charge resolution [Shar02a]. The key component of the TOF spectrometer is a TOF detector shown in Fig. 2.1.

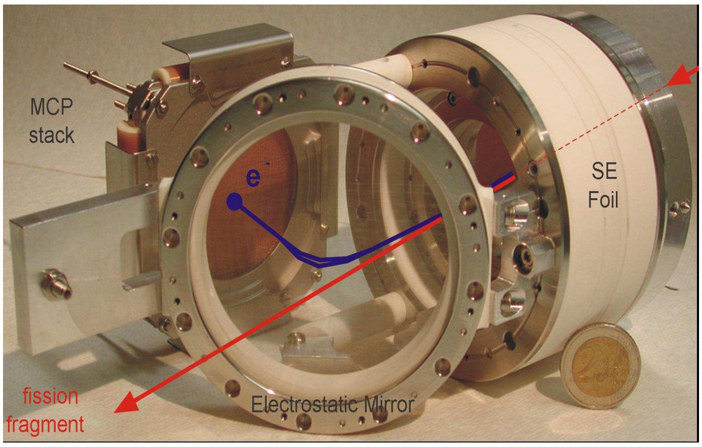

Figure 2.1: The TOF detector consists of a thin foil for secondary electron (SE) production, accelerating grids, an electrostatic mirror, a stack of multichannel-plates and a two-dimensional delay-line position-sensitive anode. The fission fragments are detected by measuring the secondary electrons impinging on the 2D anode after emission and acceleration from the foil and deflection by the electrostatic mirror. A detailed overview of the different detector components will be presented in Section 2.4.

The TOF measurements (see Fig. 2.2) can be carried out with high precision due to the very good time structure of the electron beam at ELBE. In the double arm TOF spectrometer, both the charge and the mass of each fragment are determined by two independent TOF measurements [Shar04b]. Briefly, the first TOF measurement (between the fission target and

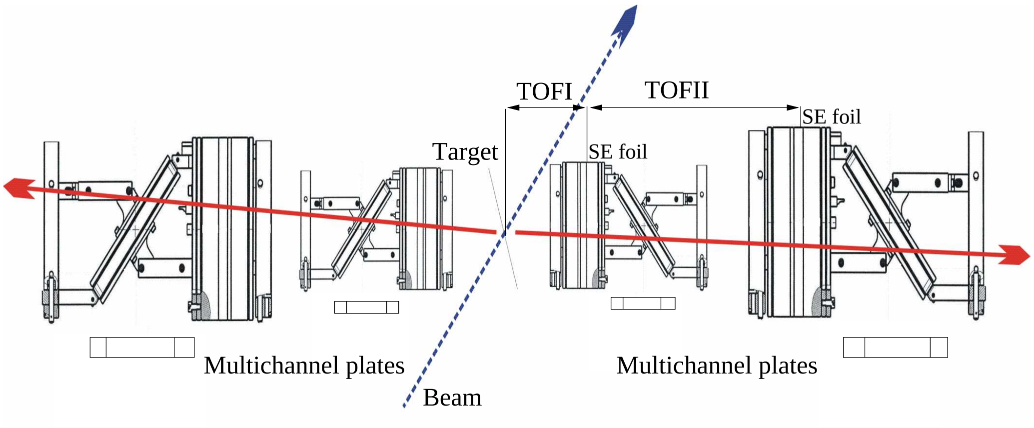

Figure 2.2: The TOF spectrometer.

the first MCP) determines the velocities and hence the masses of the two fission fragments. The energy loses in the SE-foils are proportional to Z^2 of the fission fragments, so the second TOF measurement (between the two MCPs) gives their charge numbers. The position information from the delay-line anode is used to correct the TOF spectrum for different flight paths due to the initial angular spread of the particles. After proper identification, their structure can be studied by the means of decay spectroscopy. The β decay will be measured by an array of CsI-scintillators and the γ-ray detection will be performed by an array of HPGe (cluster) detectors [Wagn05a].

2.2 General properties of multichannel-plate detectors

• Operation principle

A multichannel-plate comprises of a number of miniature electron multipliers fused together and parallelly oriented to one another as shown in Fig. 2.3.

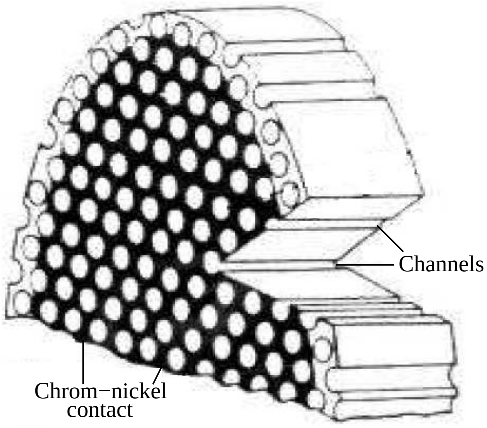

Figure 2.3: A microchannel plate.

The individual MCP channels have diameters in the order of 10-100 μm and length to diameter

ratios (α) between 40 and 100. Channel axes are normally biased at a small angle (6-8°) relative to the MCP surface [Wiza79]. The channel matrix is produced from a lead glass optimised for secondary electron emission of each channel with elemental composition given in Table 2.1. This is achieved by treating the inner surface of the channels with a semiconductor materials. Each channel can be considered like a continuous dynode structure which acts as its own resistor chain [Kana69]. Since the electrical performance characteristics of channel multipliers are not dependent on the channel length - l, or the channel diameter - d, but only on the ratio $l/d=\alpha$, an almost arbitrary size reduction is possible [Wiza79].
The deposition of a metallic coating like Nichrome or Incotel on the front and rear surfaces of the MCP serves as a parallel electrical contact to each channel. In general, these contacts are evaporated to uniformly penetrate into the channels. The total resistance between the MCP electrodes is approximately 10^8-10^9 Ω.

Z	Element	Weight(%)
82	Pb	47.8
8	O	25.8
14	Si	18.2
19	K	4.2
37	Rb	1.8
56	Ba	1.3
33	As	0.4
55	Cs	0.2
11	Na	0.1

Table 2.1: Elemental composition of MCP glass after [Wiza79].

Originally, the idea of a continuous dynode electron multiplier (see Fig. 2.4), dates back to 1930, after suggestion from Farnsworth [Wiza79]. The actual implementation, however, is postponed until 1960s when experimental works from Adams and Manley [Adam66] in U.K and Goodrich and Wiley [Good62] at the Bendix Research Laboratories in the USA are carried out. These achievements are based on the knowledge of the secondary electron emission as well as on the technique of production of conductive surfaces in lead glass by high temperature reduction (250-450 °C) in a hydrogen atmosphere [Wiza79].

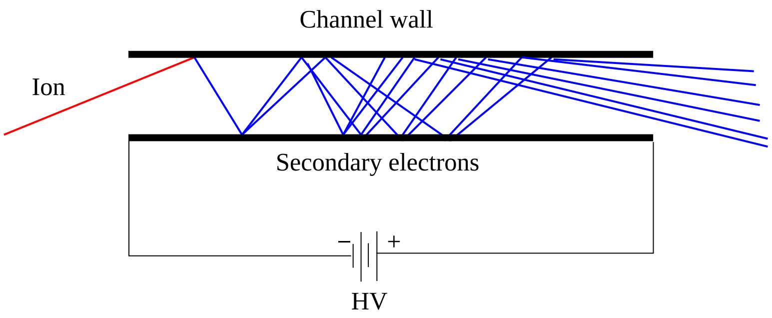

Figure 2.4: Channel electron multiplier. The blue lines indicate the electron multiplication process caused by an incident particle striking the channel wall.

If a single incident particle (ion, electron, photon etc.) enters a channel, then subsequent emission of electrons follows. An electric field applied between the both contacts of the MCP accelerates the liberated secondary electrons which travel along parabolic trajectories until they in turn collide with the channel surface, thus, producing more secondary electrons. As a result of the repetition of this process, thousands of electrons emerge from the rear of the plate [Knol89].

Supposing that an incident electron produces δ secondary electrons, one can write the relation [Wiza79]:

$$\delta = AV_c^{\frac{1}{2}}, \tag{2.1}$$

where V_c is the electron collision energy in eV, and $A \sim 0.2$ is a proportionality constant.

If the overall gain is g, then:

$$g = e^{G\alpha}, \tag{2.2}$$

where G (0.3 - 0.5) represents the secondary emission characteristics of the channel, called gain factor and α is the channel length-to-diameter (l/d) ratio. The gain factor is an intrinsic characteristic of the channel wall material, depending also on the electric field intensity inside the MCP channel. Usually, α is designed to be 40-100 which results in a gain of 10^4-10^5 with an applied voltage of 1000 V.

The statistics of the channel multiplication process govern the charge pulse height distribution from MCP with straight channels to approximate negative exponential [Gues71]. As the gain goes up, so does the probability of producing positive ions in the high charge density region at the output of the channel. They come as a result of electron collisions with residual gas molecules. This effect is especially predominant by pressures greater than 10^6 torr. Such ions will be swept back to the channel input, causing ion after pulses (ion feedback) [Adam66] if they have enough energy to produce secondary electrons. This is an undesired effect which may be minimised by bending or twisting the channels [Eva65, Schm66, Some69].

In case higher gain is required, one can operate two or more MCPs in series. This tremendously increases the electron yield up to 10^8-10^9. Multiple-stage MCP gains are not the simple product of the gain of each MCP though. At higher gains - 10^8 or more, the charge pulse height distribution changes from negative exponential to a quasi-Gaussian shape with a full width at half maximum (FWHM) of 50 % or better [Schm66]. Here, an essential role plays the gain saturation [Adam66, Schm66] caused by a space charge effect near the output region of the channels. When the gains are high, the space charge density near the channel output is so large, that the kinetic energy of the electrons interacting with the channel walls decreases, thus, approximating the secondary electron yield δ to zero. If the space charge density drops down, then the electron kinetic energy will go higher and subsequently, the δ value will increase. This is how a state of equilibrium is formed. From here, one can conclude, that the overall channel gain is limited by the space charge density which itself is determined by the channel geometry and the channel voltage. Moreover, Schmidt and Hendee [Schm66] together with Loty [Loty71] have shown that the maximum gain from a space charge saturated channel with fixed voltage and α ratio is dependent on the channel diameter. In general, the idea is that the MCPs should be operated in the space charge saturated mode, so that the pulse height distribution becomes peaked.

The Chevron configuration illustrated in Fig. 2.5, turns out to be a common method of obtaining high gain and space charge saturated output pulses. The plates are separated by 150-200 μm and are individually operated in the 10^4 gain range. They are oriented so that the channel bias angle provides large directional change, prohibiting the positive ions produced at the

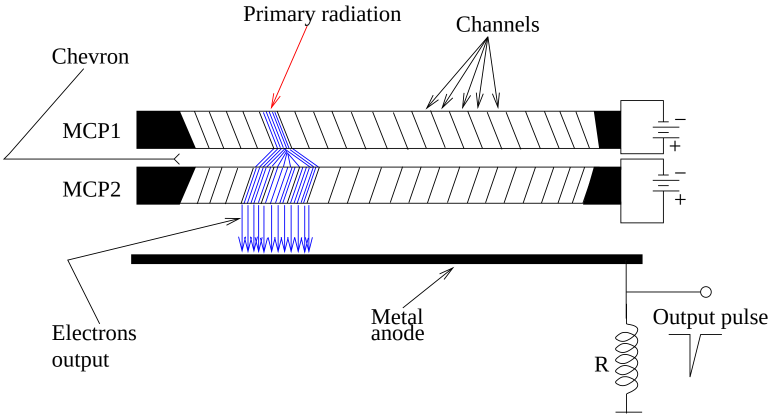

Figure 2.5: Chevron configuration consisting of two MCPs separated by 150-200 μm.

output of the rear plate from reaching the input of the second plate. In many pulse processing schemes, it is advantegous to get narrowing in the pulse height distribution. Studies have shown, that this can be achieved if accelerating potential between the plates is applied. In this case, the charge cloud coming from the first MCP plate has less time to spread radially and then as a result, fewer MCP channels from the second plate will react, but the excited ones will be driven with higher probability into space charge saturation which leads to a narrowing (FWHM < 60 % [Timo74]) of the pulse height distribution. Still, the Chevron exhibits high saturated gains ($> 10^7$) due to the multiplicity of the channels excited in the second channel plate by a single channel in the first one. Another interesting solution is reported by Henkel *et al.* [Henk78]. They propose introducing a mesh between the stacked MCPs. The idea is that the mesh restricts the charge spreading between the channel plates with an effect similar to applying interplate bias voltage.
Table 2.2 represents properties of MCPs when operated in different modes - single, Chevron, Z-Stack (three MCPs stacked together).

Configuration	l/d Ratio	Maximum Voltage	Gain	Pulse Height
Single MCP	40:1	1000 V	$> 4\text{x}10^3$	Neg.Exp
	60:1	1200 V	$> 1\text{x}10^4$	Neg.Exp
Chevron	40:1	2000 V	$> 4\text{x}10^6$	$< 175\%$
	60:1	2400 V	$> 1\text{x}10^7$	$< 100\%$
Z-stack	40:1	3000 V	$> 3\text{x}10^7$	$< 120\%$
	60:1	3600 V	$> 2\text{x}10^8$	$< 60\%$

Table 2.2: MCP performance characteristics after [Kore00]. Depending on the channel length-to-diameter ratio and type of detector configuration, narrowing better than 60 % (FWHM) of the pulse height distribution is possible.

As mentioned above, the ion feedback effect can be also avoided, if the MCP channels are twisted or bended. These MCPs are called curved channel MCPs [Timo77] and are mainly manufactured by Galileo Electro-Optics Corp. The first experimental works, however, concerning such devices are performed by Henkel *et al.* [Henk78]. They have typical α value of 80 and

channel diameters in the range of 12-40 μm. Since the Galileo MCP is based on the scaling of single channel, saturated gains much greater than 10^6 can not be expected.
Timothy [Timo74] from his work in 1974 proposes a plate which employes an angled electrostatic field to prevent the ion feedback. This is done by insertion of insulating strips inside each channel plate. The method shows saturation at high gain, but the charging of the insulating strips causes a time dependent gain reduction. Consequently such MCPs are used in limited applications.

• Detection efficiency

The MCP detection efficiency is an important performance parameter. It is basically determined as the ratio of the incoming and detected particles. Some of the intrinsic MCP features that affect it are: the open-area ratio (OAR), bias angle, metallic coating deposition.
The detection efficiency of single channel multipliers in respect to different kinds of primary radiation is presented in Table 2.3.

Type of radiation	Energy	Detection efficiency (%)
U.V. radiation	300-1100 Å	5-15
	1100-1500 Å	1-5
Soft X-rays	2-50 Å	5-15
Diagnostic X-rays	0.12-0.2 Å	~ 1
Electrons	0.2-2 keV	50-85
	2-50 keV	10-60
Positive ions	0.5-2 keV	5-85
(H^+, He^+, A^+)	2-50 keV	60-85
	50-200 keV	4-60

Table 2.3: Detection efficiency of channel multipliers after [Scha74].

The channel plates have surface work functions which allow photoelectron generation at incident wavelengths shorter than 2000 Å. Literature studies [Wiza79] report MCP efficiencies ranging from 5 % at 4.1 Å (3 keV) to 27 % at 14 Å (0.86 keV). Paresce [Pare75] in his work notes, that the most favorable configuration for photon detection is Chevron with $\alpha = 80$. It is also shown [Wiza79], that the efficiency increases as the angle of incidence decreases until a critical angle is reached, after which a rapid fall of the efficiency is observed. The maximum is reported to occur in the 1°- 6° region. The energy variation of the efficiency is explained by the variation of the X-ray absorption coefficient, and of the photo and Auger-electron ranges. Finally, one has to mention that efficiency improvements can be made by the deposition of various, high yield photo-cathode materials on the input face of the MCP. These can be for example: Au, LiF, MgF_2, BeO, SrF_2, KCl and CsI.
As the photon energies increase, the primary interaction then takes place throughout the MCP rather than at its surface. In order a photoelectron to interact with a channel wall, the channel-to-channel spacing must be small enough.
Other works [Wiza79], addressing the problem of the current and pulse response of single Galileo channel plates to X-rays in the energy range from 8-100 keV, reveal efficiency variation from 1 % to 26 % .

It is known, that as a result of further developments by Galileo [Wiza79], thick (5-10 mm) channel plates for enhanced efficiencies in gamma-ray imaging applications are fabricated. The quoted numbers are 25 % at energies just below the K-absorption edge of lead at 88 keV.
Other authors [Gala71] have observed maximum electron efficiency values (70 %) for electrons impinging at 20° angle of incidence on the MCP having energies of 1 keV. Of course, the worst case from the point of the efficiency view is when the electron trajectories are nearly parallel to the channel axes since, since then the probability for interaction will be very low. When the incident electrons are of energies much below 1 keV, the efficiency value is mainly determined by the OAR of the MCP, which is typically around 50 - 60 %. However, electrons striking the MCP with energies of 1 keV or above have sufficient probability to produce secondaries, which in term would excite neighboring channels.
Most positive ion detection efficiencies reported in literature are of the same order of magnitude as those for electrons [Tatr69].

• Response time

The transit time of MCP assemblies is very small. Due to the shorter electron transit distance compared to the discrete dynode used in the conventional PMTs, the transit time of the electron avalanche in MCP channels is in the 100 ps range or below. The timing characteristics of the MCP for a given voltage and length-to-diameter ratio are proportional to the channel diameter [Wiza79]. For example, channel plates in Chevron configuration with 12 μm diameter pores are capable of delivering pulses less than 2 ns wide, and rise time smaller than 500 ps [Wiza79]. Decreasing more the channel diameter, brings further enhancements in the timing properties of the MCP. An example Scanning Electron Microscope (SEM) image of an MCP wafer is represented in Fig. 2.6.

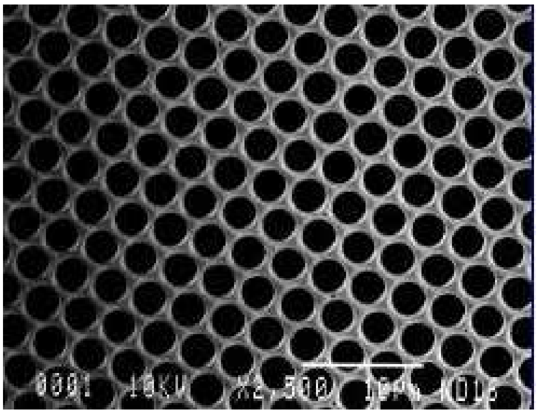

Figure 2.6: Scanning Electron Microscope image of BURLES's [Burl00] 2 μm pore MCP. The smaller channel diameter enhances the MCP timing properties due to the reduced channel path length.

The smaller channel diameter results in a decreased path length across the channel and consequently shorter transient time. In addition, if the overall length of the MCP channels is reduced, further decreasing of the transient time occurs. Such MCPs also exhibit faster recovery time due to more channels per area.
Sometimes, when ultimate timing is required, the MCP signal can be coupled to 50 Ω conical anode. The coaxial design suppresses pulse reflections, and eliminates any subsequent ringing of the outcoming signal. The following equation [Beck76] holds the relation between the impedance Z, the semi-angle of the inner cone (α_1) and the semi-angle of the outer cone (α_2):

$$Z = 60 \ln(\cos(1/2\alpha_1)/\cos(1/2\alpha_2))\,\Omega \tag{2.3}$$

Thus, time resolutions smaller than 200 ps can be obtained. In some applications, however, the limiting factor turns out to be the registration electronics. For example, if the anode capacitance is 4 pF and $R = 50\ \Omega$, then $RC = 200$ ps. This implies, that in order not to have a serious timing degradation, the subsequent electronics should not have time constant much larger than RC.
Table 2.4 represents the temporal response for a variety of detector configurations.

Detector Type	Detector Voltage	Pulse Width	Rise time
10 μm Chevron	1870 V	1.8 ns	283 ps
25 μm Chevron	2000 V	2.5 ns	640 ps
Typical channeltron	3000 V	18-20 ns	3000-5000 ps
Discrete Dynode Multiplier	2000-3000 V	30-50 ns	6000-10000 ps

Table 2.4: Temporal responses after [Kore00]

• Dead time

If one considers a 20 mm diameter MCP which is 1 mm thick with volume material between the electrodes having Dielectric constant of 8.3 F/m (Corning glass) like a parallel plate capacitor, then the total capacitance is approximately 20 pF. If the channel diameter is 20 μm, then the MCP channel number at OAR of 50 % is estimated to be $5{\times}10^5$ with a capacitance of $4{\times}10^{-17}$ F per channel. Assuming that the typical electrode to electrode resistance is in the order of $3{\times}10^8\ \Omega$, the associated each channel resistance will be $1.5{\times}10^{14}\ \Omega$. After a channel is activated, the charge in the channel walls must be replenished which means that an effective channel capacitance $C_c = 4{\times}10^{-17}$ F should be recharged through a channel resistance $R_c = 1.5{\times}10^{14}\ \Omega$. Consequently, the channel recovery time T_c is given by: $T_c = R_c C_c \sim 6$ ms. Although dead times in the order of 10^{-2} s for each channel are calculated, the fact that the MCP consists of $\sim 10^5$-10^6 channels which operate independently, makes the effective dead time of the MCP around 10^{-7}-10^{-8} s. This would imply, that at countrates of 10^6 Hz, no serious gain degradations are expected, provided that no single channel is excited more frequently than once every 10^{-2} s.

• Spatial resolution

The ability of the multichannel-plate to resolve spatially two adjacent events can be referred as its position (spatial) resolution. The channel diameter and center-to-center (c-c) spacing (channel pitch) are usually the limiting factor, since each channel of the MCP acts like an independent electron multiplier. MCPs with channel diameters ranging from 5 μm (6 μm c-c) to 15 μm (18 μm c-c) are typical. In Chevron mode, the spatial resolution would be deteriorated as compared to a single MCP because the electrons coming out from the first stage spread out into many channels as they enter the second MCP stage. Besides, the increased gain causes greater space electrostatic repulsion when the electrons are emitted from the MCP. In general, MCPs with channel diameters of 8 μm or less are considered best for position measurements [Wiza79]. Methods of event localization which make use of phosphorus screens are available. The phosphorus screen is coated with Al [Mult05] which acts as a regular metal anode and is capable of providing a time resolved signal. The metal layer ensures an uniform electric field between the MCP output electrode and the phosphorus screen. New faster phosphors materials with decay time better than 80 ns are being developed. Such methods, however, require high gain MCP configurations, a Chevron or curved channel MCP. Another popular event location technique employs a resistive anode encoder. One can put electrodes at the four corners of the resistive sheet and process x and y information independently. Some experiments (like the one described in the present work) utilize MCP detectors with a delay-line anode. It serves for a high resolution 2D-imaging. The position of the detected particle is encoded by the signal arrival time difference at both ends of each delay line.

• Dark count

The dark count from MCPs arises from several factors: thermionic and electric field emission from the channel walls, the ionization of residual gases, local discharge by a high electric field, natural and cosmic background. Noise has been known to be reduced by cooling. The intensity of the electric field can be reduced by increasing the channel diameter and the length while keeping the gain constant. A typical MCP shows extremely low dark current density (less than 0.5 pA/cm^2) at an applied voltage of 1 kV per stage. At room temperature, the dark count from a Chevron is somewhat 1-3 count/cm^{2}s. This is due to the high work function of the lead glasses, so that the thermal emission rates of electrons resulting in high gain output pulses are extremely low. Dark count rates, however, increase at pressures bigger than 10^{-6} mbar because of ion feedback effects. Also, contaminations by Na and Rb contribute to the higher dark count background. Therefore, better manufacturing process can lead to a reduction in the dark noise.

• Dynamic range

A definition of the MCP dynamic range is the range of detectable signal level over which the detector linearly amplifies a signal. This is an important performance feature of each channel plate detector, depicted in Fig. 2.7.

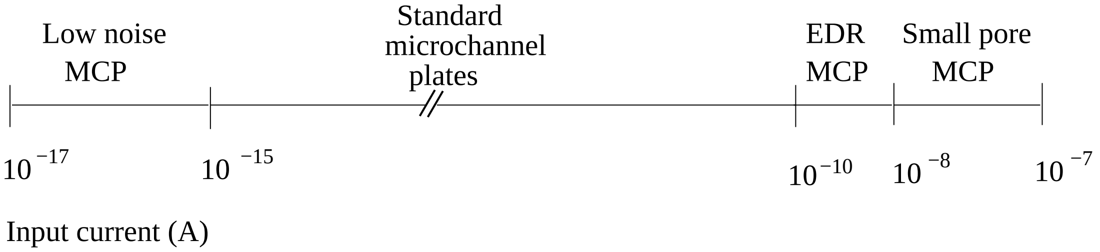

Figure 2.7: Scale of the smallest and largest detectable input signals after [Kore00].

The detection of extremely low signals is limited mainly by the background noise (dark current). One of the ways to overcame this problem is the use of specialised low noise glass formulations. The upper limit of the dynamic range is dominated by charge saturation effects taking place in the individual channels. Lowering the resistance of the channels forming the MCP, results in diminishing their dead time, since their RC constant becomes effectively smaller. This allows for higher count rates - a critical factor for some applications. Low resistance microchannel plates are also called Extended Dynamic Range MCPs or EDR plates [Kore00]. Another solutions is to increase the OAR by decreasing the channel diameter, thus, lowering the probability of ionisating particle to interact with a channel within its dead time. In other words, the threshold for a low signal detection is enhanced by lower noise glass composition, while going to higher count rates demands low resistance microchannel plates and smaller pore MCPs.

• Durability

Changes in the channel wall secondary emission coefficients determine the operation time of a MCP detector. If the conversion efficiency decreases over time, then the useful operation time of the multiplier is also compromised. The gain drop can be expressed as a function of the accumulated counts or the charge extracted. This is presented in Fig. 2.8.

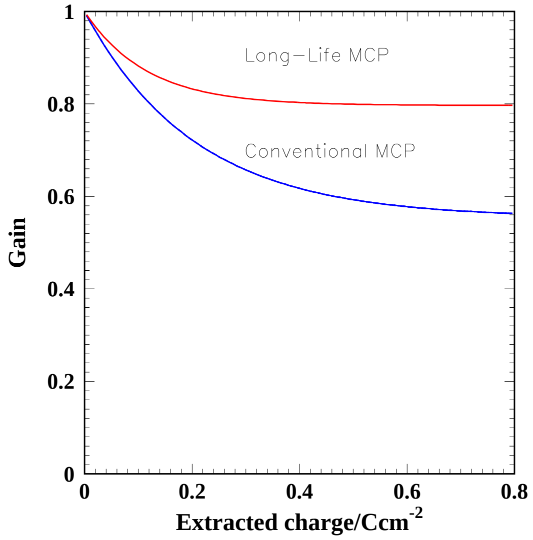

Figure 2.8: A comparison after [Kore00] of the gain drop between a conventional and non-standard (long-life) MCP detectors as a function of the extracted charge. The figure shows efficiency drop down to 60 % for an extracted charge of 0.4 C/cm^2.

Because of their structure and the nature of the materials used in manufacture, other issues concerning the MCPs durability are their storage, handling and operation. Among these is the necessity of oil free storage and pumping environment, desiccator type filled with argon or nitrogen storage cabinets. No physical objects should come in contact with the active area of the wafer. Poor vacuum conditions will most probably shorten MCP life or change its operating characteristics. It is well known, that voltages should not be applied at atmospheric pressure. A pressure of $< 10^{-6}$ or better is desired, otherwise damaging due to ion feedback or electrical breakdown may occur. Only when a satisfactory vacuum level is achieved, voltages may be carefully applied. Maximum allowable voltages across a single MCP according to Burle [Burl00] manufacturer depending on the l/d ratio are:

- α 40:1 requires 1000 V
- α 60:1 requires 1200 V
- α 80:1 requires 1400 V

The operating voltage is defined as the potential difference between the input and output side of a multichannel-plate. It strongly depends on the length-to-diameter ratio α. A rule of a thumb is that multiplying α by 25 gives the maximum allowable bias voltage. Operating the MCP at higher potentials may result in irreversible damage. One should also bare in mind, that when biasing the MCP detector, extreme care should be taken to avoid unwanted discharges. This may happen not only in poor vacuum conditions, but also along unclean detector isolating surfaces or in the presence of deposits from pumps or ion sources materials. Therefore, placing safety resistors in the corresponding circuits that will limit the maximum average current is a must. For example, a resistance value of 10^6 Ω at an applied voltage of 3 kV limits the average current to 3 mA. Signal connectors should be wired to anode through a High Voltage rated (3-4 kV) capacitor with typical capacitance $\sim$ 1-3 nF.

• Applications

The field of MCPs applications is quite broad. One can mainly distinguish between two groups:

- detection quality MCPs
- image quality MCPs

Detection quality MCPs are exploited in signal detection applications like TOF mass spectrometry, astronomy, residual gas analysis and others.

Image quality MCPs are designed for imaging or position sensing applications. When supplied with the proper readout, they are capable of providing an intensified high resolution image. This makes them suitable for use as second generation image intensifier tubes, ultra cathode ray tubes, magnetic sector mass spectrometry, ESCA (Electron Microscopy for Chemical Analysis), VUV (Vacuum Ultraviolet) spectrometry. Other relevant fields of applications are the high speed photography, space applications (reliability and the stable performance are critical) and others.

2.3 A time coincidence test setup with multichannel-plate detectors

In order to study the microchannel plates and to investigate their functionality better, two MCP detectors as shown in Fig. 2.9 have been assembled in our lab with the following parameters:

- thickness - 1 mm
- MCP active diameter - 25 mm
- MCP channel diameter - 10 μm
- single MCP gain - 10^4
- MCP anode diameter -25 mm
- MCP operating pressure $< 2\times10^{-6}$ mbar

The timing properties of these detector prototypes are also revealed in the works of Dmitriyev *et al.* and Lukyanov *et al.* [Dimi79, Luky86], where they are incorporated as an important part of TOF spectrometer.

In our measurements, we operate the MCPs in Chevrone mode, so that the gain and timing signals are most optimal.

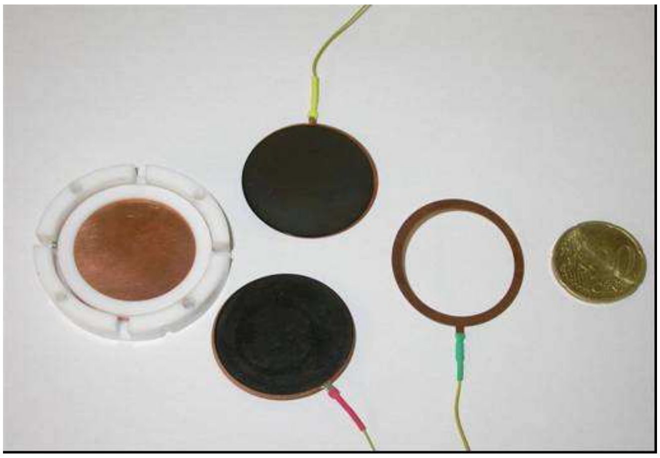

Figure 2.9: The picture represents a disassembled MCP stack detector. On the most left, one sees the copper anode used for signal decoupling. In the middle are depicted the two MCP crystals comprising the Chevron stack. On the right is shown a copper contact rings which also serves for high voltage supply.

The MCPs are used as SE multipliers in a complex zero-time detector [Shar02b], depicted in Fig 2.10. Similar setup is also described elsewhere [Gira77].

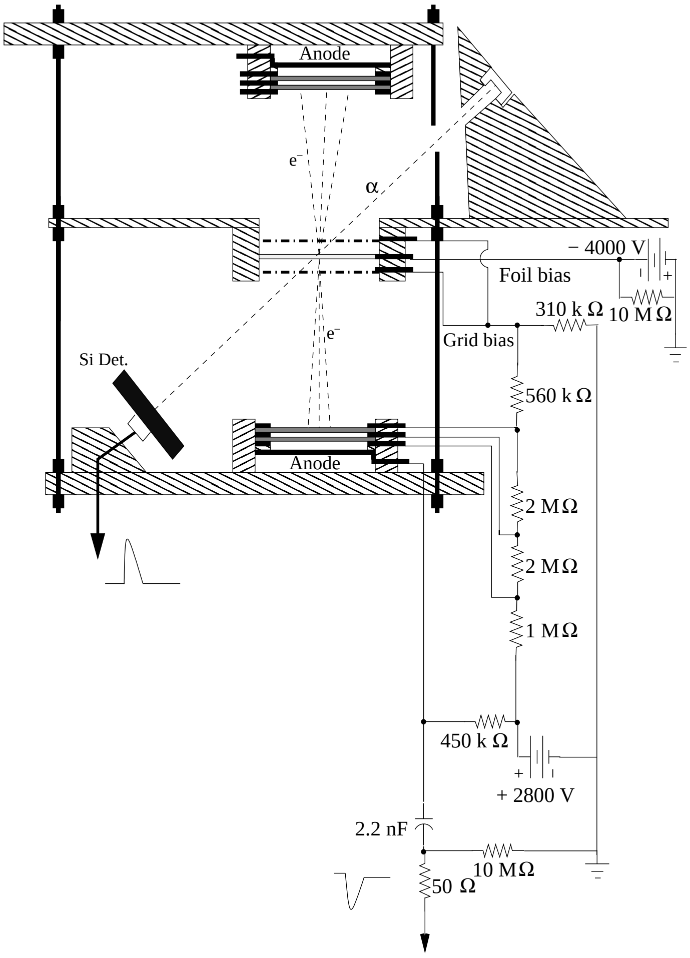

Figure 2.10: The provisional setup. Alpha particles hitting the negative biased foil eject electrons out of it in opposite directions. They are accelerated by the slightly positive potentials applied at the foil grids. After certain flight path, the liberated electrons produce signals in the MCP stacks. In order to prevent collecting events generated by noise, the MCPs are operated in coincidence with the Si detector. A dedicated resistor chain provides the necessary bias voltages for the MCPs, the foil and accelerating grids.

The provisional setup consists of a silicon detector (segment part of the RoSiB silicon ball [Paus00]), a collimated mixed radioactive (^{239}Pu, ^{241}Am, ^{244}Cm) α-source, foil with accelerating grids and two MCP detectors [Shar02b]. The distance between the alpha source and the silicon detector is kept about 80 mm and the distance between the foil and MCPs approximately 45 mm. The alpha particles impinging on a thin (2 μm thick) aluminium biased at -4 kV foil at an incidence angle of 45°, eject SE electrons out in forward and backward directions. These are attracted by the small positive (+200 V) potential applied at the grids and finally detected by the MCPs. The anode, the MCPs and the accelerations grids are biased with a single positive bias supply by using a resistor chain. Only the foil is biased separately. The elements of the resistor chain are chosen such that the potential difference between each channel plate is around 1000 V. The potential difference anode - last stage MCP is set at +500 V which ensures better electron collection. The MCP signals are derived through a 2.2 nF capacitors and 10 MΩ grounded resistor. Figure 2.11 represents a typical oscillograph picture of the MCP anode signal.

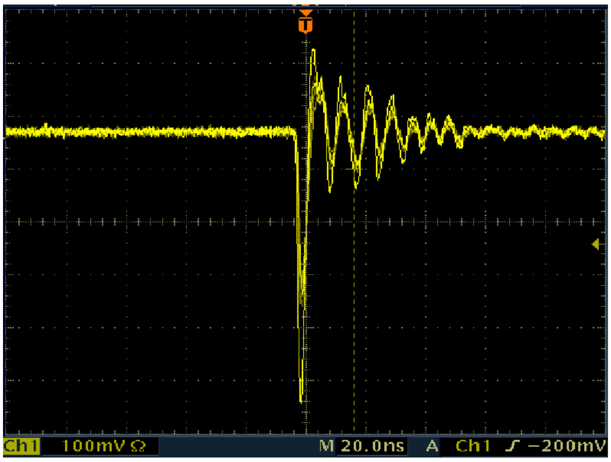

Figure 2.11: Oscillograph picture of the MCP anode signal. At full bias voltage applied, the observed amplitude reaches up to more than 400 mV. The estimated signal rise time is about 1 ns. Non-optimal impedance matching causes signal ringing which decays within 40 ns.

To test the performance of the setup, coincidence measurements between the two MCPs and the Si detector have been carried out. A standard fast-slow coincidence setup as shown in Fig. 2.12 is applied.

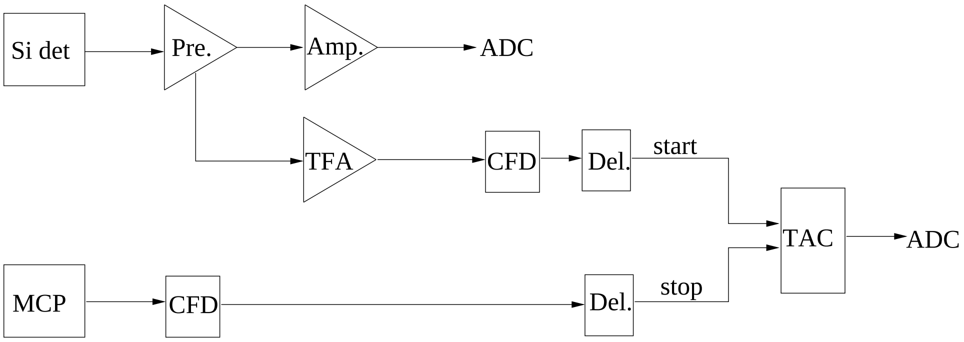

Figure 2.12: Block diagram of the fast-slow coincidence setup.

The signals from the channel plates are directly processed by Philips [Phil00] Constant Fraction Discriminators (CFD), whereas the signals from the Si-detector are fed to a charge-sensitive preamplifier. Its energy output is distributed to an ORTEC[1] 671 Spectroscopic Amplifier while its timing signal is routed to an ORTEC 474 Timing Filter Amplifier (TFA). The ORTEC 567 Time-to-Amplitude Converter (TAC) module serves for accumulating the timing spectrum. In order to avoid any pickup in the Si detector caused by high voltage discharges, the MCPs and

---

[1] ORTEC, 801 South Illinois Avenue, Oak Ridge, TN 37839, U.S.A.

the foil are supplied with metallised grounded surfaces.
The data is acquired using a Multi-Channel Analyser. The obtained Time-to-Amplitude (TAC) spectra are shown in Fig. 2.13.

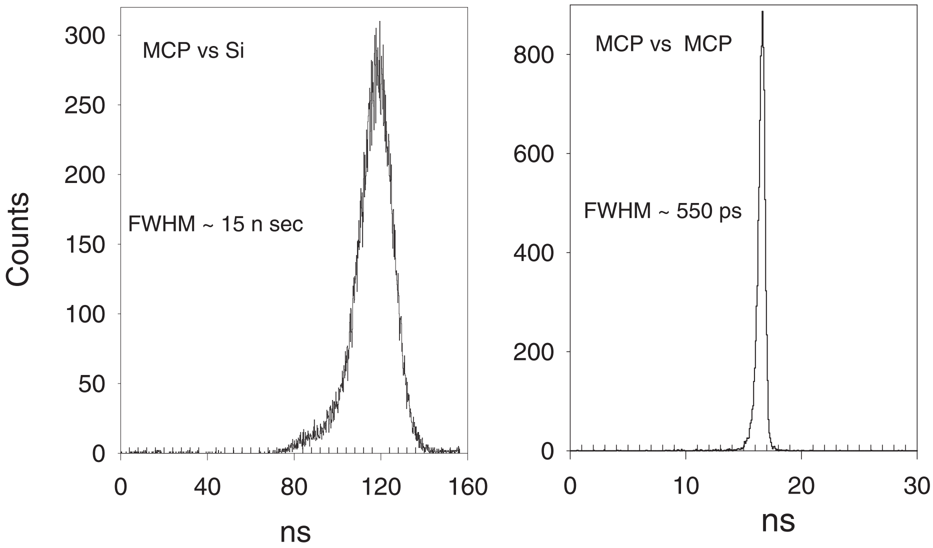

Figure 2.13: The TAC spectrum results in 15 ns for MCP versus Si detector (left) and 550 ps for MCP versus MCP (right). We consider that the Si-MCP timing is dominated by the properties of the Si detector.

The currently achieved time resolution between the two MCPs is mainly influenced by the type of projectiles ejecting the foil electrons. It is known, that α-particles are capable of producing below 10 electrons in the 2π hemisphere when interacting with a thin foil [Cler73]. So, the obtained result is in agreement with the expectation that the time resolution should be proportional to $\sqrt{n_e}$ [Wiza79], where n_e denotes the electron number. Besides, a better readout electronics, improved MCP impedance matching circuit and better vacuum conditions could additionally enhance the timing properties of the setup.

2.4 Components of the Time-of-Flight spectrometer

Generally, the TOF detector suited for fission studies, which is depicted in Fig. 2.1 can be divided into three main functional parts:

- foil for SE emission
- electrostatic mirror
- MCP detector with position-sensitive delay-line anode

Each of them will be treated individually in a separate subsection.

2.4.1 Foil for secondary electrons production

In this work, thin Al-metallised polyethylene terephthalate (PETP) as well as Al-metallised lexan foils for SE production with an optimised thickness allowing the unambiguous fission-fragment Z separation are used. The aluminium layer, typically 100 Å thick, serves for ohmic

contacting. We have to mention, that the SE emission is a surface effect, involving only a very thin target foil material (2.5 μg/cm^2 in case of carbon [Cler73]). The SEs knocked out from the foil are accelerated by an electrostatic field of more than 7 kV/cm, so that their angular spread is minimal. It is formed by applying small positive potential at two electrostatic grids (+200 - +300 V) sitting in front and behind the foil, and high negative one (-2 - 4 kV) at the very foil for a grid to foil distance of 5 mm. The grids function is not only to ensure positive attraction of the electrons, but also to prevent the foil from mechanically bending.
Because of their high fragility, special techniques to mount the foils in the detector setup are required. This has been done under clean room conditions at the site of FZR Rossendorf with the help of dedicated instrumentarium. Some of the preparation steps are depicted in Fig. 2.14, 2.15 and Fig. 2.16.

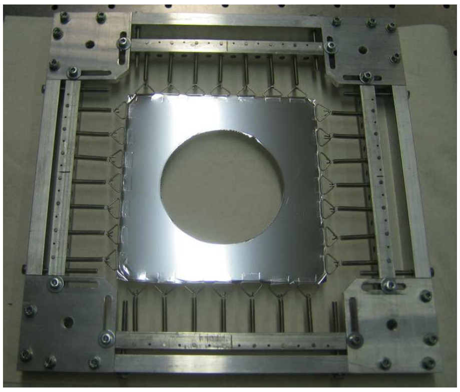

Figure 2.14: The foil sample is mounted on a special holder with the help of supporting springs. Once carefully tensed, it is precisely cut out. Attention is taken to avoid micro foil mechanical damages. Before mounting on the detector system, all foil dust particles and impurities are removed.

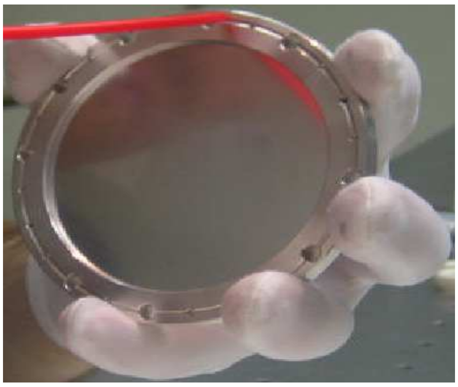

Figure 2.15: The cut out foil is placed between two supporting metal rings.

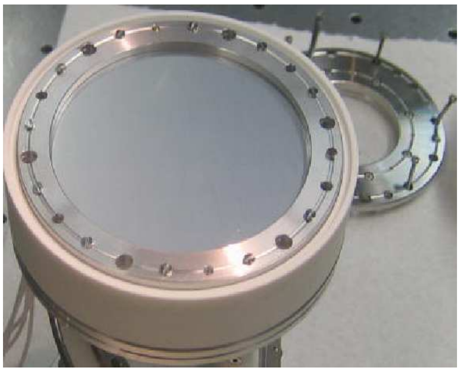

Figure 2.16: Finally, the prepared construction is nested inside a dedicated ceramic holder.

A schematic overview of the prepared setup is also presented in Fig. 2.17.

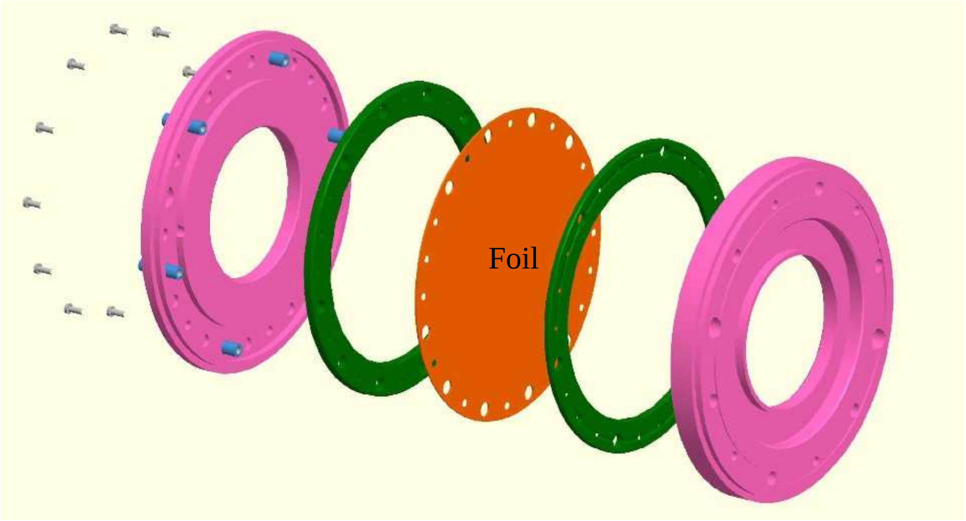

Figure 2.17: The foil (useful diameter of 40 mm) sits between two metal grids (green) and is isolated from the rest of the spectrometer by two ceramic units (pink).

2.4.2 Foil thickness measurements

As already mentioned, the energy loss information in the SE foils is a tool to extract the Z numbers of the fission-fragments. Therefore, the knowledge of the precise thickness profile of these foils is an important requirement for the TOF spectrometer [Kose02]. In order to extract such information, energy-loss measurements have been carried out using a collimated mixed (^{239}Pu/^{241}Am/^{244}Cm) α-source.

A 4 μm thick PETP foil with dimensions of 46×70 mm has been prepared. To measure its thickness profile, it is mounted on a frame, in between the alpha source and a silicon detector inside a vacuum chamber, set at about 6.7×10^{-6} mbar. The foil frame is moved along two dimensions with the help of two stepper motors, remotely controlled as shown in Fig. 2.18.

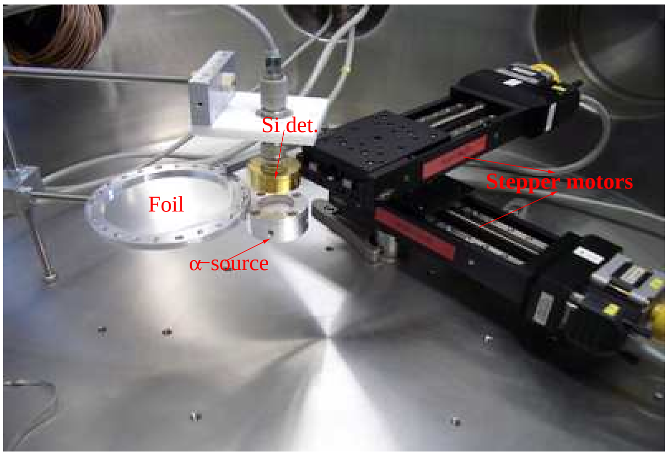

Figure 2.18: The figure gives principle overview of the foil thickness measuring setup. The motors are displayed on the right side. The foil structure which for this particular setup is different than the one described above, sits in a metal ring and is seen on the right. The silicon detector and the alpha source are displayed in the middle.

The setup position resolution is in the order of a few μm. For each run, 24 measurements are taken with a step of 2 mm while keeping the other direction fixed.

A spectroscopic electronics setup is used to determine the rest energy of the alpha particles after passing the foil. Figure 2.19 shows a comparison spectra taken with and without the foil.

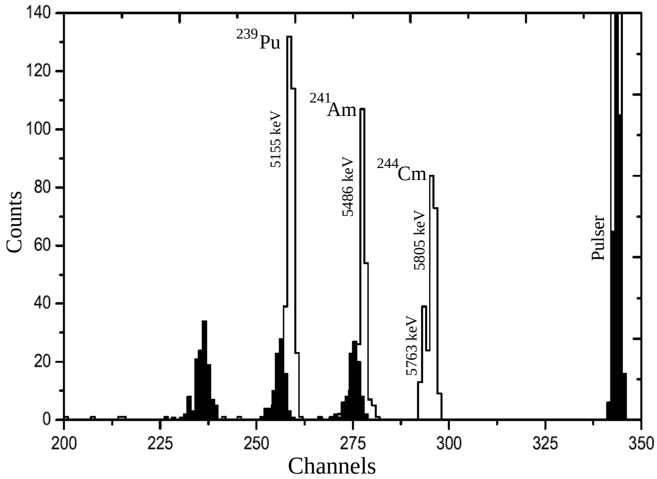

Figure 2.19: Comparison between a calibration spectrum (hollow peaks) and a spectrum with foil (full peaks). For monitoring any gain shift in the electronics, an ORTEC 440 research pulser is applied.

The silicon detector (type EURISYS[2] LEC 200-4000) with a sensitive area of 200 mm^2 and an useful thickness of 4.25 mm is connected to a ZfK-VV5 preamplifier and an ORTEC 570 main amplifier set at shaping time of 0.5 μs. Energy resolutions better than 0.6 % are typical for this detector. The data is acquired using Interwinner MCA. More than 1200 spectra are collected while scanning the whole area of the foil. A dedicated program has been developed for an automated analysis which locates the peaks and fits them with Gaussian distributions. The energy-loss of the alpha particles in the foil is determined and the thickness derived from the centroid of the peak. The result of the foil thickness measurements is presented in Fig. 2.20.

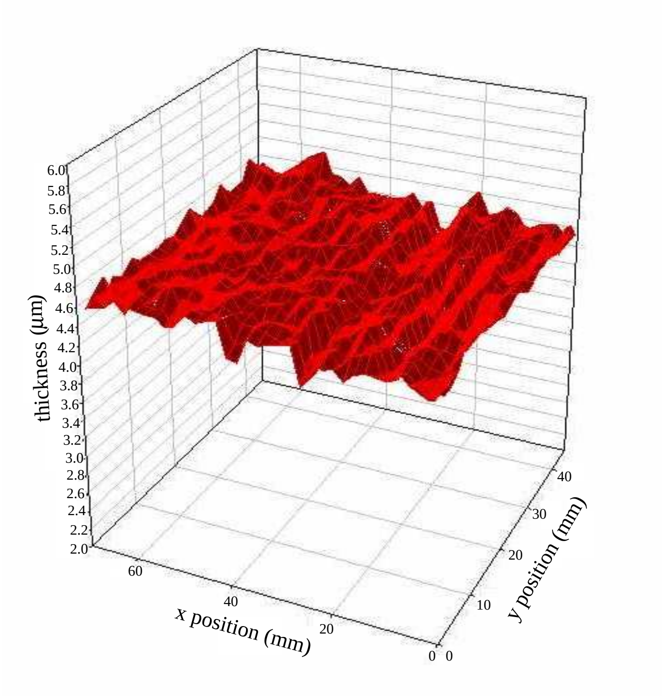

Figure 2.20: Two dimensional distribution of the foil thickness profile using energy loss of alpha particles.

The measurement shows a satisfactory uniform thickness distribution of the foil as demonstrated in Fig. 2.21.

---

[2] EURISYS MEASURE, Parc des Tanneries 1, Chemin de la Roseraie 67383, Lingolsheim Cedex, France.

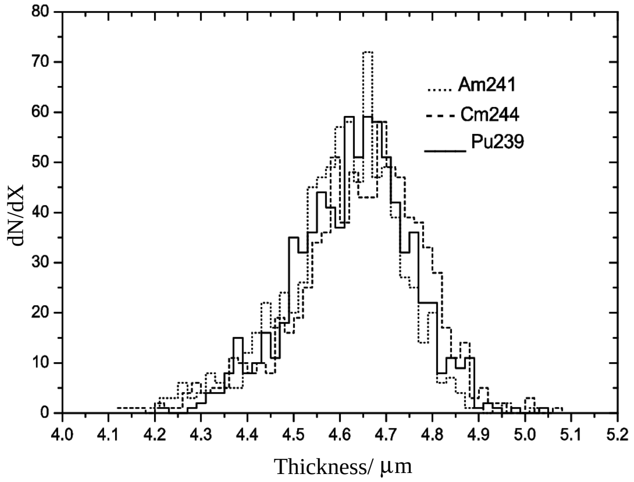

Figure 2.21: Foil thickness distribution showing good agreement between the derived thicknesses for the three alpha energies.

2.4.3 The electrostatic mirror

The main function of the electrostatic mirror is to deflect the secondary electrons towards the MCP surface isochronously [Shar02c].

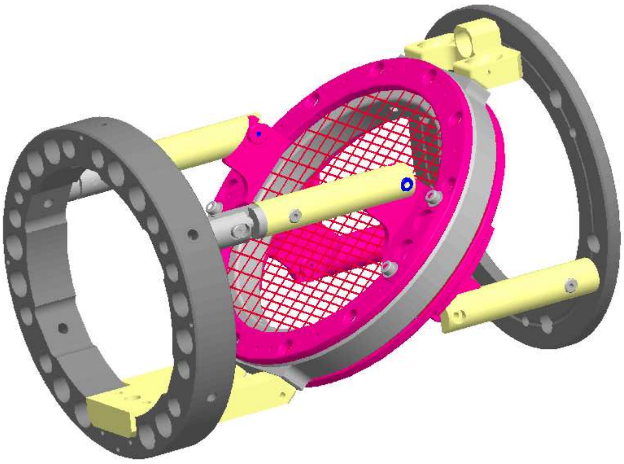

Figure 2.22: The electrostatic mirror.

The mirror consists of two stainless-steel frames and two grids made of stainless steel crossed wires with a diameter of 31 μm and a pitch distance of 0.25 mm. A ceramic ring [Vitr00] provides 10 mm separation between the two grids. The mirror is bended under 45° with respect to the MCP detector so that the flight path of the SE emitted from the foil is approximately 120 mm. In order to ensure proper mirror functionality, high voltage potentials are applied at the two wire grids. These are not arbitrary, but rather have values depending on the foil and the accelerating grids potentials [Shar02c].

This issue together with the mirror transparency problem will be discussed in the following two subsections.

2.4.4 Enhancement of the time and space resolution of an electrostatic mirror

In order to obtain higher time and space resolution for a given geometry, detailed calculations of the mirror potentials are required. Distribution of the field potentials simulated with SIMION 3D [Simi00] is presented in Fig. 2.23 [3].

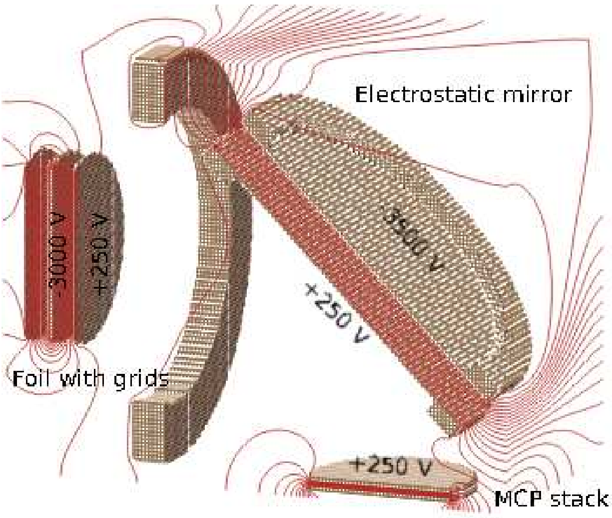

Figure 2.23: Distribution of the field potentials at given voltages simulated with SIMION 3D.

One can principally divide the whole system into three regions [Nank04a]. The first one extends from the foil to the mirror front side. It is treated like field free drift region. The second one is between the mirror surfaces. In first order approximation the electric field inside the mirror is considered homogeneous. The third region is between the mirror front side and the MCP. It is assumed to be field free also. The above quoted assumptions for the three regions enable us to carry out exact calculations of the SEs TOF.

Three particles with the same starting point and direction, but with different energies are traced inside the system. The exact solution of the equations of motion for the three regions gives the following relation for the TOF of the probe particles [Nank04a]:

$$T = T_0 + \left(\mp \frac{L_1 + L_2 - d\sqrt{2}\Delta V_f/\Delta V}{v_0} \pm \frac{2m_e v_0 d \sin\theta}{e\Delta V} \right) \delta, \tag{2.4}$$

where T_0 is the mean TOF, L_1 and L_2 are the distances between the mirror and the foil and between the mirror and the MCP, respectively, d is the mirror height, ΔV_f and ΔV are the foil acceleration potential and the mirror deflection potential, v_0 and δ are the mean velocity of the secondary electrons and their spread, θ is the angle between the flight direction and the mirror plane and m_e is the electron mass (see Fig. 2.24).

Taking that θ is 45°, then the TOF of the secondary electrons will be independent on their initial velocity spread only when the factor before δ from Eq. (2.4) vanishes. This leads to the following condition [Nank04a]:

---

[3] The SIMION 3D simulations are performed by Dr. N. Nankov.

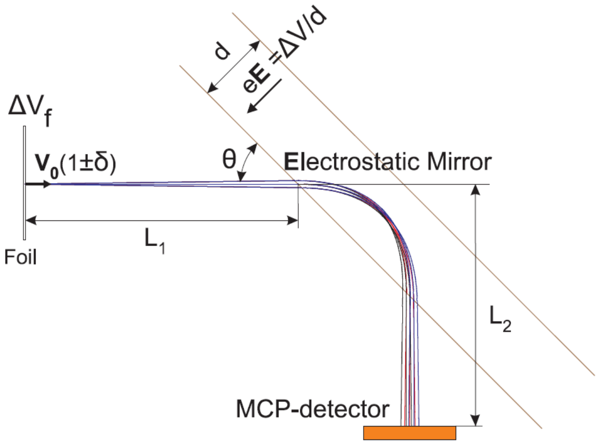

Figure 2.24: Time spread due to the initial energy spread of the SEs.

$$d/(L_1 + L_2) = 0.236(\Delta V/\Delta V_f). \tag{2.5}$$

Relation 2.5 enables us to optimise the foil acceleration and mirror deflection potentials such that the SEs reach the MCP isochronously. However, the latter condition can be only partially fulfilled with our present geometry, since as will be demonstrated in Chapter 5, the needed appropriate accelerating potentials become an issue for the system efficiency and position resolution.

2.4.5 Mirror transmission and the scattering problem

Another two important system parameters to be investigated are the mirror transparency and the scattering of the beam particles when impinging on the electrostatic mirror grids. To study this two phenomena, the following setup as depicted in Fig. 2.25 is proposed.

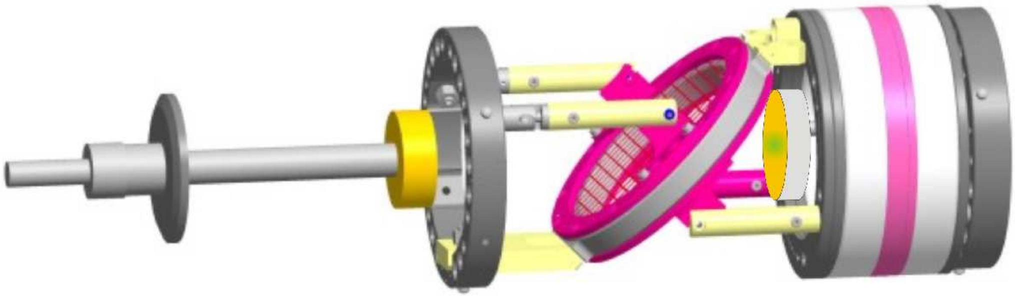

Figure 2.25: Alpha particles emitted from a mixed radioactive (^{239}Pu, ^{241}Am, ^{244}Cm) α-source (green spotted), and penetrating through the mirror grids are detected by a 300 μm with an active area of 600 mm^2 ORTEC silicon detector (yellow cylinder). The mirror is positioned 45° relative to the beam direction.

The obtained energy spectrum provides information about the degree of scattering and mirror transmission. The measurements are performed in the following manner: 24 hours calibration run is taken without mirror positioned between the source and the detector, and another 24 hours run with mirror in-between. Two resulting spectra are shown in Fig. 2.26.

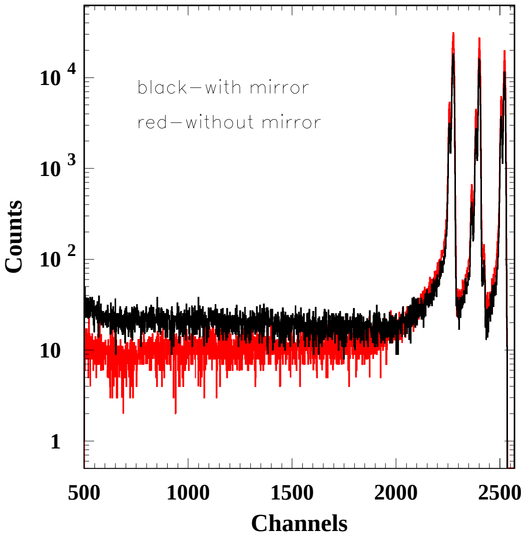

Figure 2.26: Demonstration of two comparison energy spectra with mirror and without mirror positioned between the source and the detector. Information about the particle scattering can be obtained from the difference of the counts in the peak tails. The ratio of the peak counts derives the transmission value.

The tails counts difference related to the useful counts in the three alpha peaks of the calibration spectrum gives us the amount of scattered particles which turns out to be 2.0(9) %. Similarly, from the ratio of the counts in the alpha peaks of the two spectra, we estimate, that the grids transmission is 79.0(7) %. The quoted transmission value, however, does not only reflect the properties of the mirror, but also accounts for a certain geometrical effect. To prove that, measurements as displayed in Fig. 2.27 are conducted.

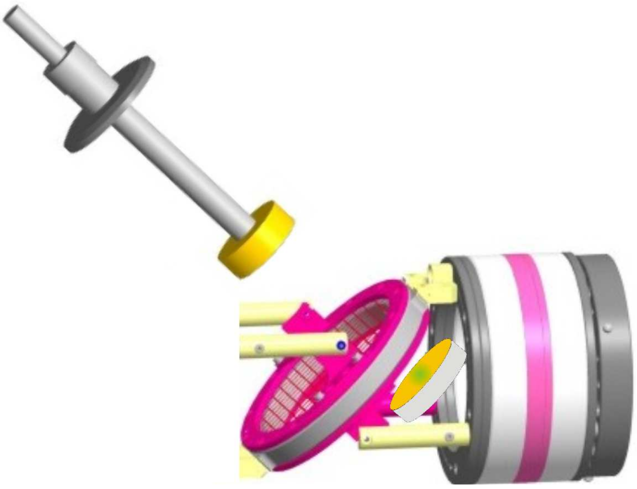

Figure 2.27: The mirror positioned 90° relative to the beam axis.

In this case the grids transmission raises up to 83.0(1.4) %, while the scattering value remains almost unchanged - 2.(1) %. One possible solution to enhance the transparency is to introduce serpentine like grids with larger wires pitch. To estimate the impact of such grids on the position resolution of the detector, simulations with a realistic detector geometry have been performed using the computer code SIMION3D. The obtained results for SEs accelerating potential of 3250 V and deflection potential of 2950 V are presented in Fig. 2.28.

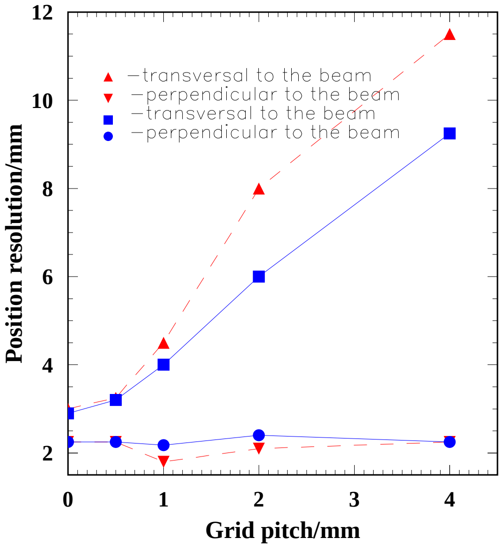

Figure 2.28: Estimated position resolution related to the wires pitch. The dashed lines correspond to particles deflected at the edge of the electrostatic mirror, while the solid ones to particles deflected in its center.

The simulation shows that the increase of the wires pitch affects mostly the transversal beam component, while the perpendicular one for particles deflected in the mirror middle or its edges remains relatively constant. Serpentine like wires with pitch distance of 1 mm are capable of providing transparency of more than 97 %. According to the simulation the time resolution is not affected by varying the pitch distance, which is mainly due to the high SEs acceleration.

2.4.6 The position and time sensitive multi-hit multichannel-plate delay-line detector

The MCP detector together with the position-sensitive delay-line anode is the heart of the spectrometer system. Here, we will dwell on their most important properties.

The RoentDek MCP detector [Roen00] with delay-line anode is a high resolution 2D-imaging and timing device suitable for charged particle or photon detection. It withstands high rates and has multi-hit capability. It consists of pair of rimless MCPs in chevron configuration supported by a pair of partially metallised ceramic rings (2 mm thick, 65 mm in outer diameter) and a 2D-position sensitive delay-line anode (helical wire pair). The ceramic rings are Nickel metallised with additional metal contacts. The MCP stack is mounted on a support plate (holder) as displayed in Fig. 2.29. The operation affords two DC voltages for MCP front and back contacts and three voltages for the holder and the anode wires. They are supplied through a dedicated high voltage divider module.

Two MCP detectors produced from different manufacturers (Burle [Burl00] and Photonis [Phot00]) are utilised in our experiments. Some of their physical characteristics when operated in chevron mode are displayed below:

- α Burle MCP: 60:1
- α Photonis MCP: 80:1
- Thickness: 1.5 mm
- Useful diameter: 40 mm
- Pore size Burle MCP: 25 μm
- Pore size Photonis MCP: 12 μm
- Center-to-center spacing: 25 μm
- Bias angle: 7°± 2°
- Open are ratio: $>$ 50 %
- Operating temperature range: -50 to 70 °C
- Operating pressure: $< 2\times10^{-6}$ mbar

The electrical properties of the MCP detectors together with their typical performance features are summarised in the following:

- Operating voltage Burle MCP: 2500 V
- Operating voltage Photonis MCP: 2700 V
- Electron gain: $> 1\times10^{-7}$
- Position resolution: $<$ 0.1 mm
- Rate capability: 1 MHz
- Multi-hit resolution: 20 ns

The MCP from Photonis requires a thin contacting rim placed in between. It provides a small space between the two plates, which is sufficient enough to ensure a proper angle orientation of the front and back plate channels. Burle MCPs on the other hand are placed in direct contact without the support of an intermediate contact ring. Special triangle marks on their outer rim side indicate the tilt angle direction of the MCP pores. It is possible to increase the overall gain by using triple stacks of these MCPs.

From the above quoted specifications, it becomes apparent that each MCP plate has a different operating voltage range, correlated to its particular α ratio. For example, the MCP from Burle ($\alpha \sim$ 60:1) needs 1300 V maximum, whereas the Photonis MCP ($\alpha \sim$ 80:1) accepts voltages up to 1500 V per plate. The optimal potentials of the MCP front and back side depend on the type of particles to be detected. Two general modes are destinguished - electron and ion detection (see Table 2.5).

	Ion or Photon Detection	Electron detection
MCP front	-2400 V	+300 V
MCP back	0 V	+2700 V
Anode holder	+150 V	+2850 V
Reference wires	+480 V	+3180 V
Collecting (Signal) wires	+500 V	+3200 V

Table 2.5: Ion and photon detection modes after [Roen00].

For most ion species, it is suitable to operate the MCP back side on ground potential, while keeping the front side at -2400 V relative to it. Electron detection, on the other side, requires minimum 300 V electron preacceleration ensuring optimal efficiency. Thus, the MCP front side is biased +300 V in respect to the electron source. In the course of our work, however, we have found out that lower bias voltages also yield sufficient detector performance. Operating the MCPs at the highest possible potentials is often at the cost of their exploitation period. In order to avoid possible discharges, the bias voltage is applied in steps of 100 V to these detectors. This also serves as a protective measure for the connected electronics. High voltage power supplies modules type 19"-3U HV from the company Iseg [Iseg00] with current limitation and fast shutdown functionality are used. They have as well in-built current monitoring function enabling the experimenter to observe possible current deviations in the course of measurements. Currents in the order of 300-600 μA are typical. Sparks are also avoided by not allowing dust particles settling in between the MCPs during assembly or other kinds of manipulation. The excellent vacuum conditions (7.8×10^{-8} - 1.7×10^{-7}mbar in our case) achieved with VARIAN TURBO-V 301 [Vari00] turbomolecular pump contribute additionally to the proper operation of the whole setup.

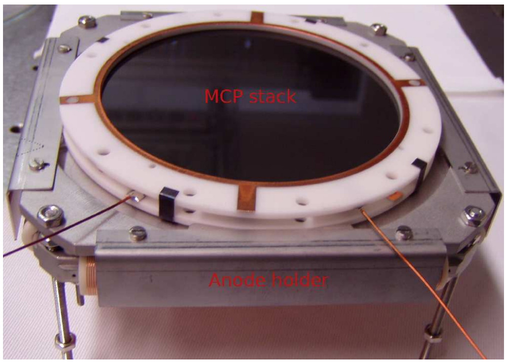

Figure 2.29: Overview of the position and time sensitive MCP delay-line detector. The MCP stack and the delay-line anode are supported by anode holder. Electrical contacting between them is prevented by means of ceramic insulations. Two read-out signals (front and back) are directly extracted from the MCPs through copper wires.

The anode wire array consists of two double delay-line helical propagation lines depicted in Fig. 2.30. For each dimension, a wire pair is formed by a collection and a reference signal wire. A potential difference of about +20 V of the signal wire in respect to the reference one is required, thus, ensuring that the electron cloud emerging from the MCP is collected mainly on the signal wires. The wires are also supposed to have about 500 V more positive potential in respect to the MCP back side. The anode holder is biased about of +150 V referenced to MCP back. The whole combination of voltages provides a proper charge cloud propagation and spatial broadening in the drift zone between MCP and anode wires. Yet, we have to mention that the choice of the optimal potentials depends on the distance between the MCP holder plate and the anode wires as well.

The four ends of the two delay lines are connected from the corner contacts of the anode to vacuum feedthroughs by a twisted-pair wire configuration. From the feedthroughs, the signals are routed to a differential amplifier.

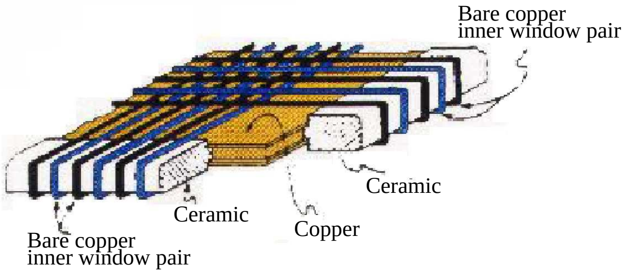

Figure 2.30: Position sensitive delay-line anode.

A schematic overview of the whole setup - detector plus position-sensitive delay-line anode is given in Fig. 2.31.

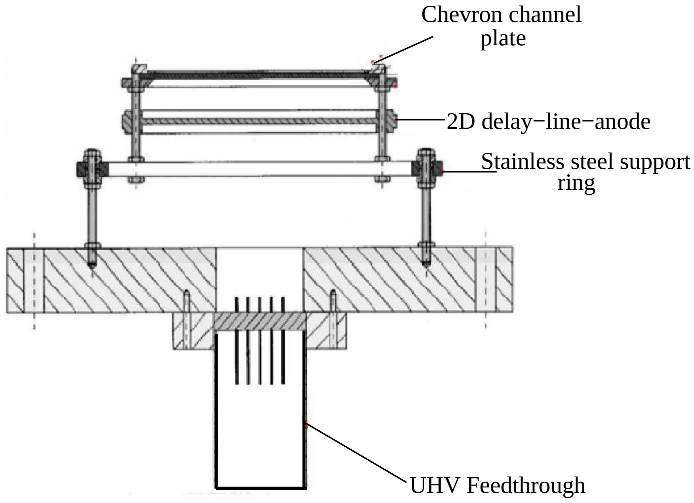

Figure 2.31: Overview of the MCP delay-line detector system. The whole unit is connected to a 12-pin CF35 UHV-feedthrough flange fitting in CF100-adapter-flange. The feedthrough pins serve not only for delivering the required high volatges to the MCP front and back, and to the anode wires and holder, but also for signal decoupling. The supporting rods for the stainless steel ring, the anode and MCP stack are supplied with ceramic insulations, thus, preventing electrical contact between the different system components.

2.4.7 Position encoding

The position of the registered particle is encoded by the signal arrival time difference at both ends for each parallel pair delay-line, for each dimension independently. The time sequence of the signals is measured by time-to-digital converter (TDC). As time reference (start of the TDC), the signal on MCP front or rear side can be used. The digital encoding to obtain a 2D image (X/Y) is:

$$X = x_1 - x_2 \text{ and } Y = y_1 - y_2, \tag{2.6}$$

where x_1, x_2, y_1 and y_2 denominate the TDC channel number for each event. The single path signal propagation time on the delay line is about 0.71 ns/mm which corresponds to 1.42 ns/mm for the 2D case. We have to note that the above quoted value has accuracy within 5 % dominated by wires crosstalk, etc.

2.4.8 Methods of high voltage supply and signal decoupling

In order to operate the system correctly, appropriate high voltage potentials have to be applied to the MCP back and front, the anode wires, the holder, the foil for SE production, the grids and the mirror parts. These can be done by using individual high voltage supply channel for each spectrometer component or by implementing high voltage divider modules with a dedicated in-built resistor chains. The second method suits better our needs, first, because it

is cost effective, since the total number of the needed high voltage channels is less, and second, but not least, we consider it safer. If for example, MCP front and back are biased separately and one of them trips accidently, at certain circumstances this may irreversibly deteriorate the functionality of the whole detector stack. There are also other scenarios which show that it is disadvantegous to have some system components suddenly at pretty low potential because of high voltage trip, while the others remaining highly biased. A high voltage divider on the other hand solves the problem by ensuring simultaneous up and down bias for all detector parts. For the MCP stack detector, anode wires and holder, mirror components, foil and grids, separate dedicated resistor chains are utilised. The description of their functionality comes next.
First, we will draw our attention on the MCP stack circuit as presented in Fig. 2.32.

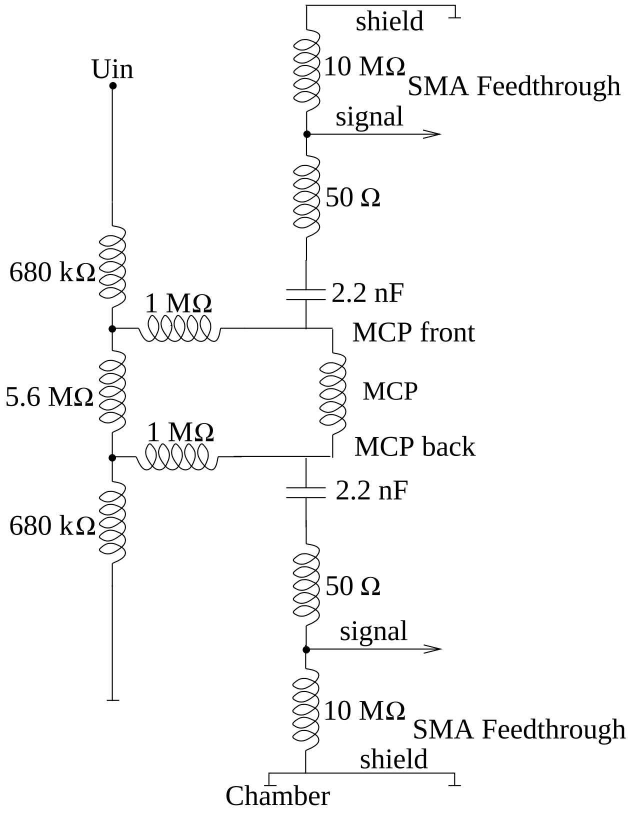

Figure 2.32: MCP bias supply and signal decoupling.

The chosen circuit corresponds to electron detection mode. For simplicity, the MCP stack is depicted like resistor. The high voltage division is accomplished through two 680 kΩ and one 5.6 MΩ resistors in series. Their values are chosen such that MCP front and back sides accept the correct potentials. The two 1 MΩ parallel resistors prevent the useful MCP front and back signals to flow back in the high voltage divider circuit. Instead, they are integrated on 3 kV rated, 2.2 nF capacitors. The 50 Ω resistors serve for impedance line matching. MCP front and back signals are decoupled by 10 MΩ grounded resistors. The setup will function without them, but the charged 2.2 nF capacitors, when applying high voltage, will immediately discharge through the subsequent electronics modules. Our present experience shows that this may sometimes cause serious damages. Therefore, placing such safety resistors is mandatory. Finally, the signal is extracted through a stainless steel 50 Ω Subminature-A (SMA) flange feedthrough and fed for example to a CFD module or an oscilloscope. The choice of the 1 MΩ, 10 MΩ, 50 Ω and the 2.2 nF capacitors turns out to be crucial for many timing applications. At first, discrete elements with the above mentioned values have been implemented. It is known, however, that elements of such type, as well as the cable lengths, introduce additional parasitic capacities and inductivities deteriorating the derived timing signal. To anneal the problem, we switch to surface-mount devices (SMDs) elements, sitting directly in the vicinity of the detector surface. This together with the impedance matching problem will be treated in the following subsections.

Next, we will dwell on the wire anode circuit. It is depicted in Fig. 2.33.

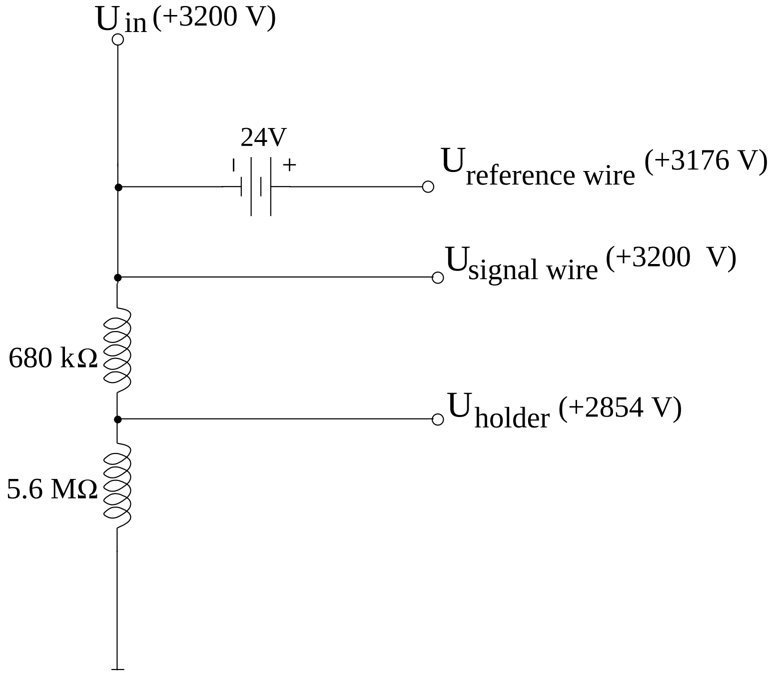

Figure 2.33: Anode and anode holder bias scheme.

Special 24 V battery fulfills the requirement for higher signal wires bias in respect to the reference ones. The anode holder is kept at about 200-300 V lower than the actual anode potentials. This ensures that the electron cloud emerging from the MCPs will be collected mainly by the anode wires.

The obtained from the reference and signal wires signals are processed by a DLATR6-module [Roen00]. This is a 6-fold differential amplifier with integrated CFD circuits NIM module. Each amplifier features two independent channel inputs for differential amplification of a mV-input signal and CFD signal output. Additionally, it offers an automated CFD walk adjustment function. The CFD stages have pulse pair resolution of about 20 ns. The output signal width can be also controlled. The fact that it is a modular device, allows for easy replacement of any amplifier board, if damaged. Its principle of operation is revealed in Fig. 2.34.

The bias scheme for the mirror front and back, foil and grids parts is represented in Fig. 2.35. The high voltage is supplied through two 1 MΩ resistors. They act mainly like current limitators. The role of the 1 nF capacitors is to integrate any possible sparks when the system is under high voltage. Discharges may be caused by impurities on the mechanical parts, bad vacuum conditions or mechanical gaps in the region of the high voltage contacts. This may lead to an abrupt raise of the electrical currents flowing in the nearby circuits or sudden vacuum worsening. Of course, such effects are undesired and care is taken to be avoided.

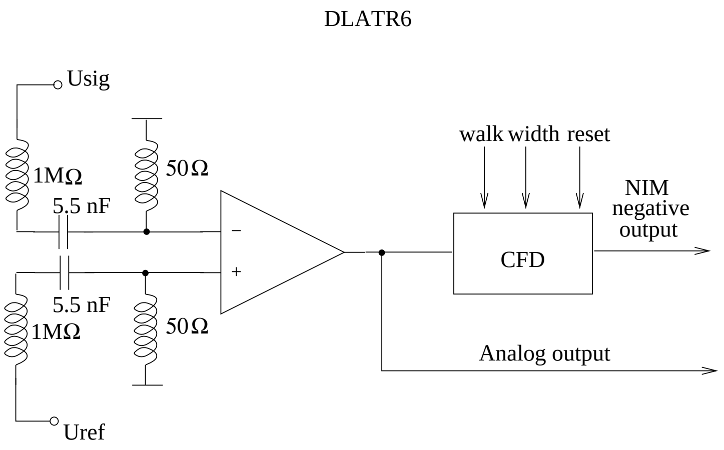

Figure 2.34: DLATR differential amplifier module, designed to read out the signals from the position-sensitive anode. The amplifier has two independent channel inputs for differential amplification of mV signals as well as CFD and analog outputs.

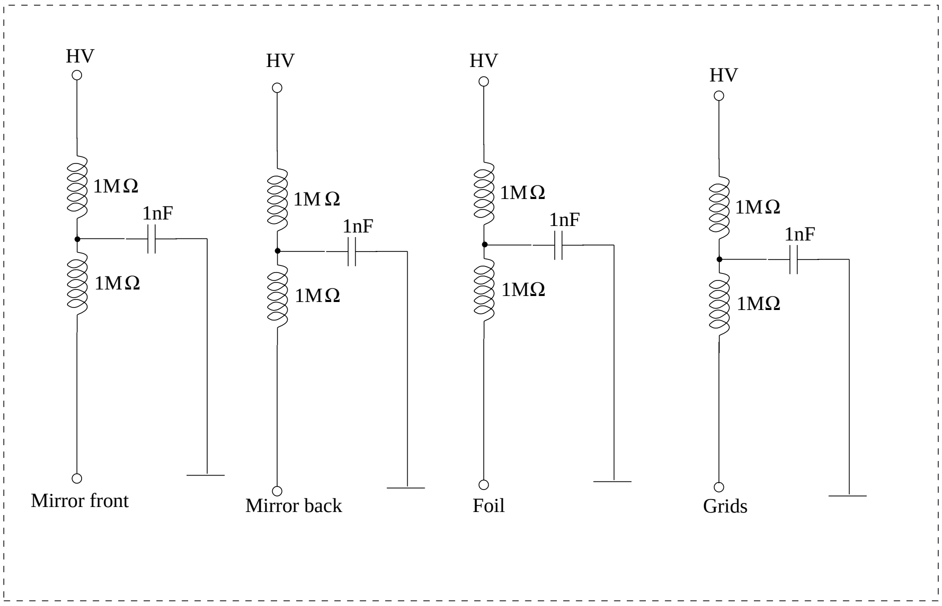

Figure 2.35: Low-pass filter for the mirror bias supply and spark protection.

2.4.9 Determination of the dynamic multichannel-plate resistance

The investigation of the physical properties of our MCP detectors allows for an optimal operation. One important quantity to study is the change of the MCP dynamic resistance as a function of the bias voltage. The measured potential difference on the 5.6 MΩ resistor (see Fig. 2.32) at different bias potentials together with the mean current values, enables us to obtain such dependencies for MCP (Burle) and MCP (Photonis), respectively, as shown in Fig. 2.36. The two curves are linear meaning that the dynamic resistance remains constant for wide range of operating voltages. From the above results, we can deduce the dynamic resistance values for Burle and Photonis stack which are in the order of 70 and 220 MΩ.

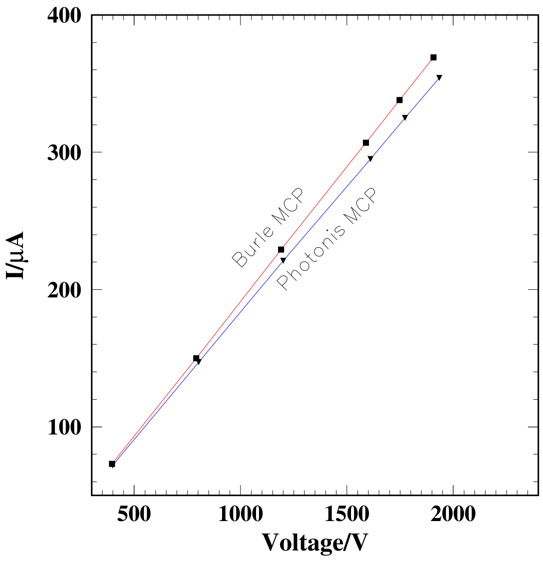

Figure 2.36: Current as a function of the applied voltage. The red line corresponds to MCP (Burle) and the blue one to MCP (Photonis). The current shows linear dependence over a wide range of applied voltages. The uncertainty of the measurements is in the order of 0.05 %.

2.4.10 Signal processing

As already pointed out, the MCP signal decoupling takes place either by means of discrete elements or SMD parts. The latter method has the advantage of avoiding the additional capacities and inductivities introduced by the bulky discrete elements as well as the extra cable lengths. This eventually results in improved timing measurements due to preserving the fast signal component. As a drawback, one can mention the extra effort to find the appropriate miniature elements rated up to 3-4 kV. Pictures of the two possible solutions can be seen in Fig. 2.37.

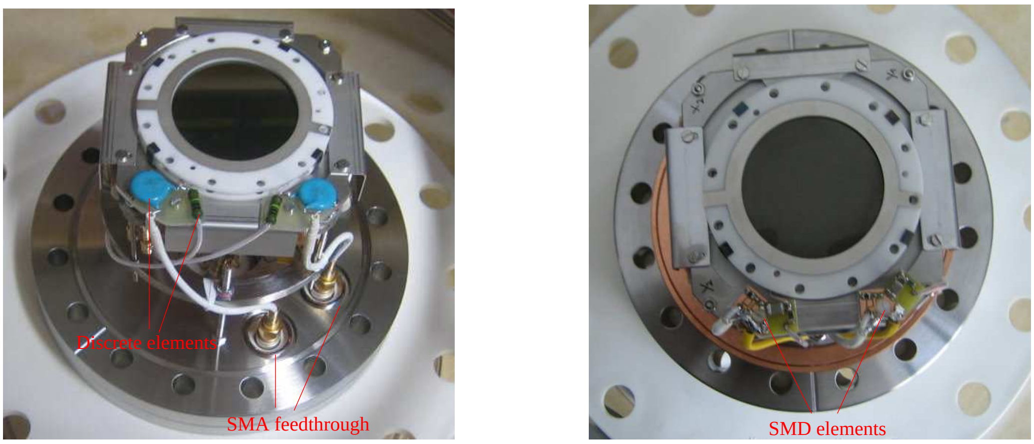

a)

b)

Figure 2.37: Setup with discrete elements a) and SMD elements b). To minimize extra cable length effects, the electronic circuits are placed as close to the detector surface as possible.

The derived MCP front and back signals are positive, shown in Fig. 2.38 a). An explanation is that the MCP contact plates remain positively charged in respect to the electron cloud travelling in anode direction. This fact has important sequences, since it imposes the need to invert the positive signals (Fig. 2.38 b), before they can be processed from any CFD. An inverting transformer from Philips Scientific [Phil00], model 460 with its bandwidth of up to 1.2 GHz and rise-time capability of less than 300 ps provides one possible solution. The above mentioned device has rugged construction, requires no power supplies and has a low cost. Except that, the Model 460 contains an inverting pulse transformer, packaged between male and female BNC connectors. This allows it to be easily inserted in a signal path with no additional cables required.

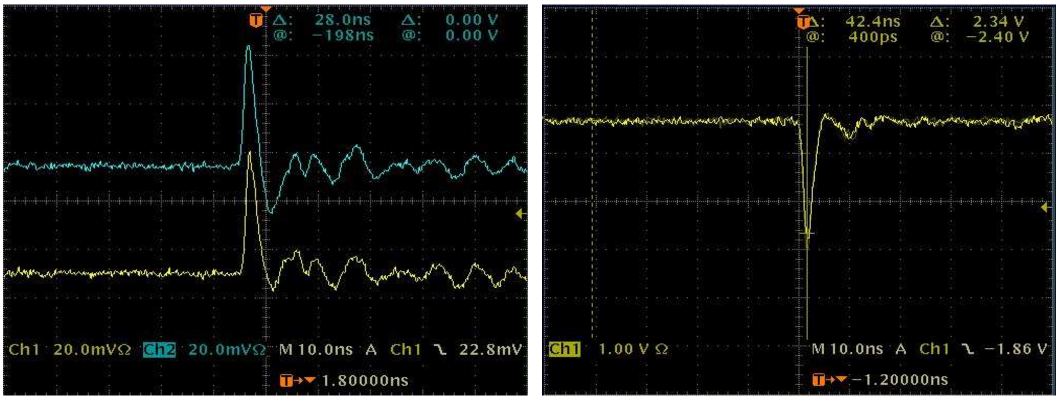

a)

b)

Figure 2.38: Oscillograph pictures of MCP back (yellow) and front (blue) signals, decoupled directly a) and a single signal inverted and boosted from ORTEC FTA 820 amplifier b).

The incorporation of the 180°-phase converter in the experimental setup is shown in Fig. 2.39.

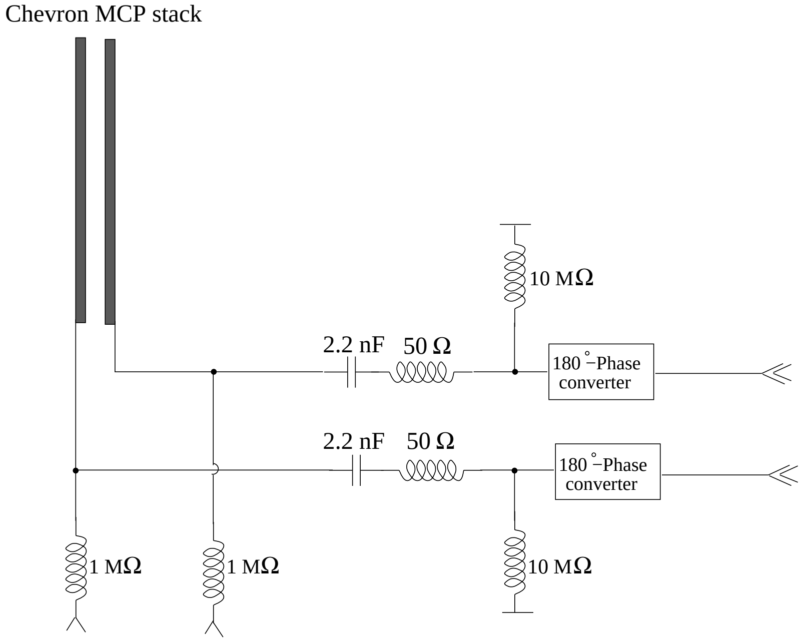

Figure 2.39: Processing the derived MCP front and back signals from 180°-Phase converters.

2.4.11 Fast transimpedance amplifier for multichannel-plate detectors

In a standard setup, the resulting MCP pulses are processed by capacitive coupled devices with low impedance (50 Ω) input. The low impedance input is necessary to preserve the pulse shape and hence the signal timing information. Since the MCP back and front signals in our setup are derived from thin rings with not well defined impedance, impedance matching problems arise. As a result, signal ringing and distortion may occur. Although it is not impossible to build 50 Ω impedance signal collectors [Wurz94], an electronic matching is the easier and cheaper solution. Therefore, a simple and fast capacitive coupled transimpedance amplifier has been developed [Schw01a].

Since we detect electrons (negative charged particles), despite all the preventive measurements, short high voltage bursts could pass through the coupling capacitor of the connected electronic device, risking damaging its electronic circuit. Therefore, the built transimpedance amplifier serves also as a protective unit against high voltage discharges.

Figure 2.40 shows the circuit diagram. The amplifier is designed to be used with a high input and a low (50 Ω) output impedance. It is without a coupling capacitor. The resistors R1 and R2 determine the operating point of the amplifier U1, the input impedance of the circuit and therefore the quality of the impedance matching. The amplifier U1 (LMH6702, National Semiconductor) is an ultra wide-band operational amplifier using inverting gain circuit. It has been optimised for exceptionally low harmonic distortion. The amplification formed by the input resistor R2 and the feedback resistor R3 does not exceed factor 4, yet improving the signal-to-noise ratio. The resistor R5 serves for impedance line matching. By mounting directly this circuit on the 50 Ω SMA vacuum feedthrough, we succeed in preserving the signal rise time and improving the CFD sensitivity, because of the additional amplification.

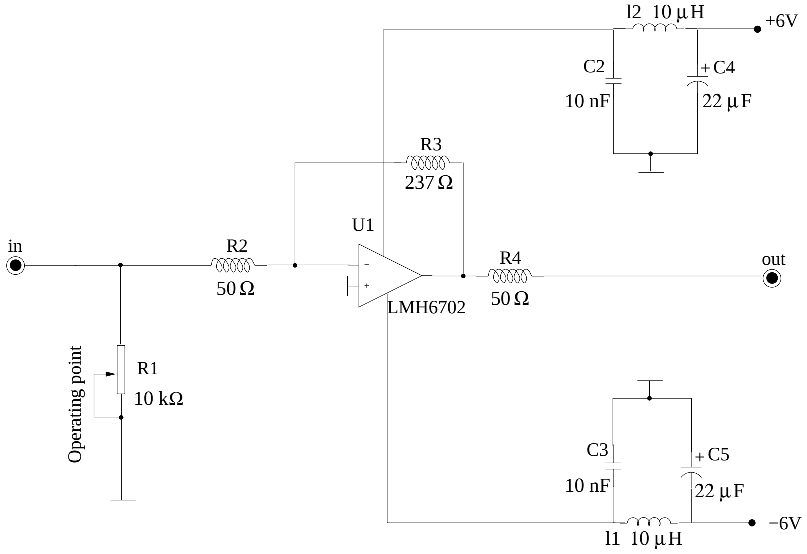

Figure 2.40: The circuit diagram.

An example of different quality impedance matched signals, depending on the operating point choice are displayed in Fig. 2.41.

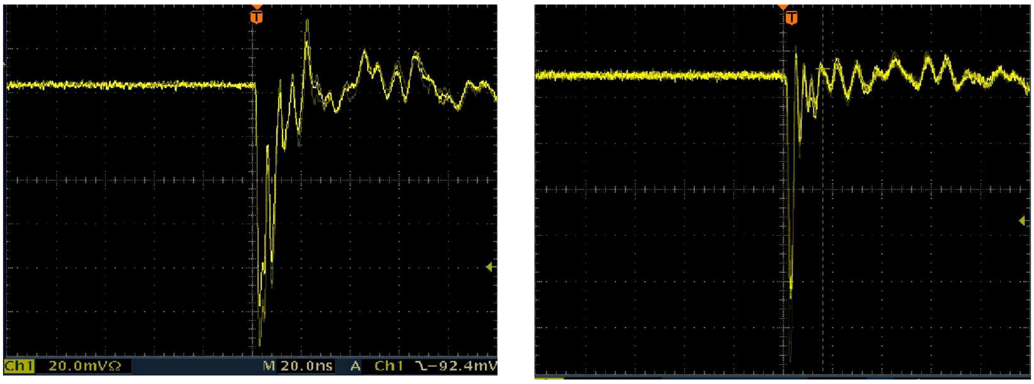

a)

b)

Figure 2.41: Low a) and improved quality b) impedance matched signals.

2.4.12 Constant Fraction Discriminator for multichannel-plate detectors

The most important property in any timing system is its resolution. It is mainly limited by fluctuations which occur in the time relation between two signals in case of time difference coincidence measurements. The source of this variations is mainly attributed to the generation of the logical signals from the different kinds of discriminators. One of the major problems faced by the experimenter in this case is the *walk* effect.

The *walk* is strongly influenced by variations in the amplitude or rise time of the detected signal. Let us process two signals with equal rise times, but different amplitudes occurring at the same time through a discriminator with fixed threshold. Because of the amplitude difference, the higher amplitude signal will produce logic signal first. The timing walk between simultaneous signals is shown in 2.42 a).

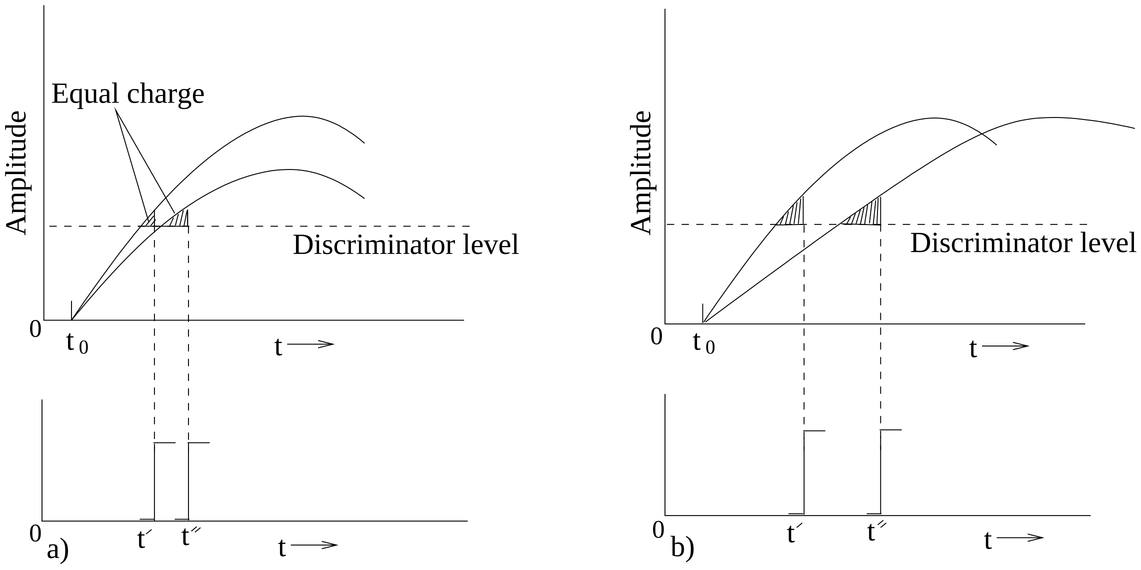

Figure 2.42: Discriminator walk. Coincident signals with different amplitudes a) or risetimes b) cross the threshold at different times.

The same effect occurs as presented in Fig. 2.42 b) if the signals are with equal amplitudes, but different rise times. The faster signal produces a logic signal first which consequently leads again to time difference in the two signals detection. An additional *walk* is induced by the finite charge which must be integrated on a capacitor to trigger the discriminator. Obviously, these undesired effects can seriously degrade the time resolution when a wide range of pulse amplitudes or signals with different rise times must be processed.
The constant-fraction discrimination, amplitude and rise time compensated (ARC) timing, and other zero-crossing techniques are highly employed for minimizing the *walk*. Here, we will shortly draw our attention on the constant-fraction timing and its derivative - ARC triggering. It is shown [Leo94, Gedk67, Gedk68], that an optimum triggering level exists providing best timing resolution. This level may be adjusted at a certain pulse height fraction independent of the amplitude, thus, producing an essentially walk-free signal. This idea forms the basis of the constant fraction triggering (CFT). The pulse shaping used by any conventional constant-fraction timing discriminator is illustrated in Fig. 2.43 a). The incoming pulse is divided into two parts. One part is attenuated to a fraction f of the original amplitude and the other part is delayed and inverted. The delay is equal to the time it takes for the pulse to rise from the constant fraction level to the pulse peak. Adding the two signals forms a bipolar signal with a zero-crossing that corresponds to the original point of optimum fraction on the delayed signal. Such discriminator delivers virtually zero walk [Meil75, Orte98], since the time of the zero crossing is independent of pulse amplitude. The result is optimum time resolution over a wide dynamic range of pulse heights. This method, however, holds, presuming that the signal rise times are equal. Another more advanced technique similar to the CFT which eliminates the condition for equal rise times is the so-called *amplitude and rise time compensation* (ARC) triggering, shown in Fig. 2.43 b).

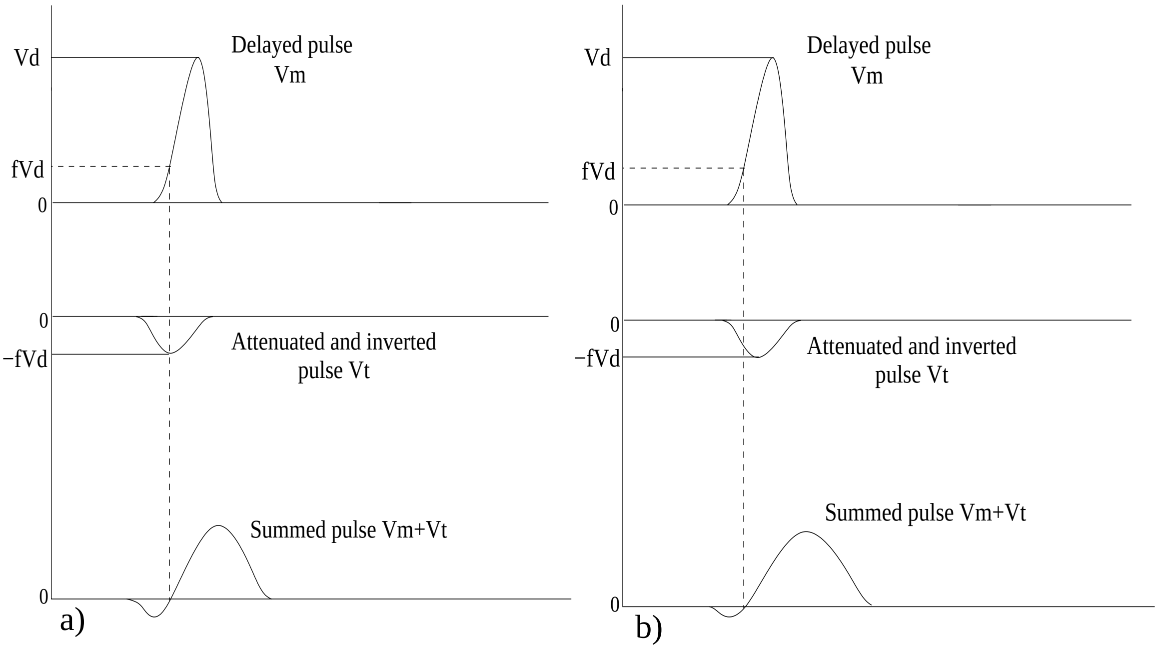

Figure 2.43: The constant fraction a) and the amplitude and rise time compensated b) techniques.

In the original CFT method, the delay must be long enough to allow the undelayed signal to reach its peak. In the ARC method, however, the delay is chosen smaller so that the zero-crossing of the summed signal occurs earlier than the signal maximum is reached. This ensures that the zero crossing depends on the earlier signals portion, thus, setting the walk effects due to different rise times at minimum. Still, the ARC timing method can not completely compensate for the rise time if the signal slope changes before the time of zero crossing. Nevertheless, we consider the latter technique to be the most optimal solution for processing the analog signals derived from our MCP detectors. This is determined mainly by the fact that due to their relatively large active diameters (∼ 40 mm), depending on the interaction position, different charge collection times may occur. That results in varying signal rise times. Moreover, the signal amplitudes obtained often remains below the 40 mV range. Processing such a signal is a challenge for any commercial CFD, since the quoted amplitude value is is often around or below the sensitivity of its threshold. Therefore, additional amplification may be needed. Introducing an external fast amplifier, however, can compromise the quality of the timing signal if its band width is not large enough. That is why, a CFD (model CFT-5388) module based on the ARC technique with very low threshold (2 mV) capabilities has been developed. Walk measurements demonstrating its qualities in comparison to other CFD modules available on the market are presented in Fig. 2.44.

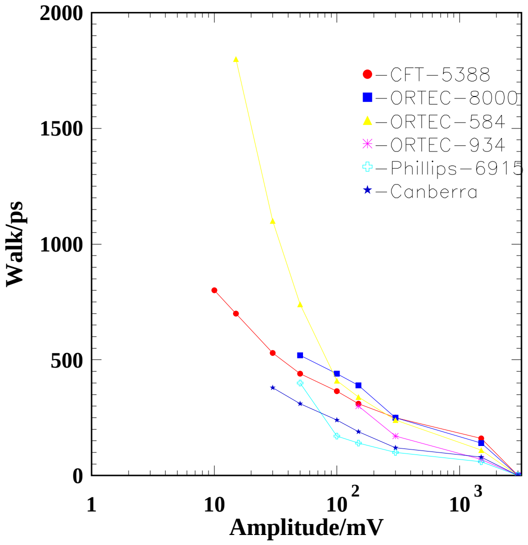

Figure 2.44: Walk represented as a function of the signal amplitude for different CFD modules. The measurements are performed by gradually attenuating the highest possible amplitude until the lowest level sensitivity threshold for a particular module is reached. The input signals have rise and fall times of approximately 1.6 ns.

Chapter 3

Data Acquisition and Control

3.1 DAQ preconsiderations

For every experiment, the choice of DAQ (Data Acquisition System) and the subsequent readout electronics plays a crucial role. This choice is determined by variety of requirements which has to be met for each particular task. Nowadays, the rapid improvement of electronics and software offers a wide spectra of solutions. The below attached Table 3.1 depicts the most popular buses available on the market.

System	VersaModule Eurocard	CAMAC	FERA	Fastbus
Architecture	Master/Slave	Master	Unidirectional	Master/Slave
Bus width	16, 24, 32, 40, 64-bit	24 bit	16 bit one way	32 bit
Data rate	>30 MB/s 80 MB/s BLT	< 1 MB/s	< 20 MB/s	< 40 MB/s
No. of slots	21	24	-	26
Power	+5 V -5.2 V +3.3 V -2 V	$\pm 6\ V \pm 12\ V$ $\pm 24\ V$	ECL	$\pm 5\ V - 5.2\ V - 2\ V$ $\pm 15\ V + 28\ V$

Table 3.1: Overview of different buses, frequently used in nuclear physics experiments.

The advantages of VMEbus become immediately apparent which explains why we employ it in our experiments. Historically, VME (VersaModule Eurocard) is established in 1981 by the companies Motorola, Mostek and Signetics/Philips and later standardized under IEEE 1014 [Schu04]. It is heavily used in the industry, military [Wran04] and the scientific research, placing it among the most popular buses. Today it is mainly maintained by VITA (VME bus International Trade Association) [Vita00], which is a large community of companies and organisations.

3.2 VME architecture

Briefly, VME is an asynchronous bus that allows for multiple bus masters, but only one arbiter. It offers the ability to plug in I/O cards in a single crate communicating with the hardware without being aware of any other cards in the crate. This is also recognised as one of the

VME strengths. The VME bus has seven daisy-chained[1] interrupt lines. The access to VME bus I/O boards is entirely memory-mapped with some physical translation between the local memory address and the VME bus address. All this is usually managed by some complex front-end computers. In our case this is CES RIO2 (Power PC CPU, 200 MHz, 64 MB RAM), running diskless under the real-time operating Lynx OS and booting from a UNIX machine using BOOTP/TFTP protocols (see Fig. 3.1). To provide an unified software interface to all I/O cards sitting in our crate, MBS (Multi-Branch System [MBS, Bart00]) has been implemented.

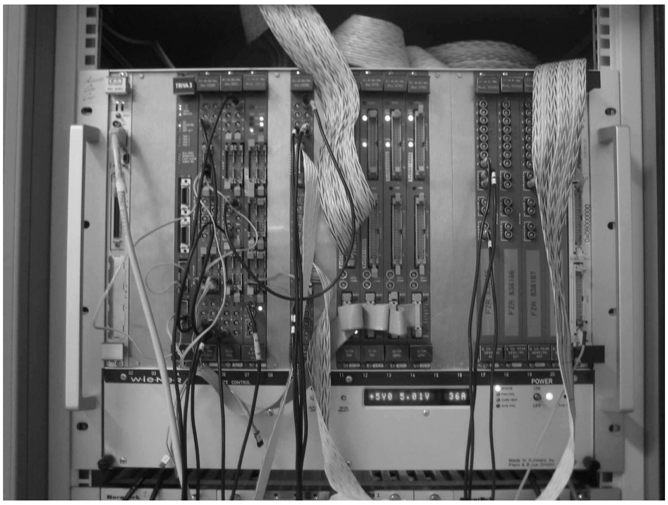

Figure 3.1: Overview of our VME crate. The RIO2 power PC is the first module in the crate beginning from left to right.

3.2.1 VMEbus functional modules

In order to describe the VME bus architecture correctly (see Fig. 3.2 adopted from [VME85]), one can use the idea of *functional modules* [Vita00]. Basically a functional module is a collection of electronic circuits residing on the VMEbus board and accomplishing a certain task.

- Master

A functional module initiating bus cycles on the Data Transfer Bus (DTB) in order to transfer data between itself and a Slave module.

- Slave

A functional module that senses DTB cycles issued by a Master and when they specify its participation, data transfer between the Slave and Master takes place.

- Interrupter

A functional module used to generate interrupt requests on the Priority interrupt bus, and on request from Interrupt handler provides STATUS/ID information.

- Interrupt handler

A functional module detecting interrupt requests from Interrupters and responding to them by asking for STATUS/ID information.

- Bus timer

A functional module measuring the duration of a DTB cycle. If this is too long, a BERR[2]

---

[1] A special type of VME bus signal line, propagating a signal level from board to board, beginning with the first and ending with the last slot. The VME bus has four bus grant and one interrupt acknowledge daisy-chains.

[2] Signal indicating unsuccessful data transfer

signal is initiated.

- Requester

A functional module demanding ownership of the DTB whenever its Master or Interrupt handler needs it.

- Arbiter

A functional module that can grant ownership of the DTB to a Requester at a time.

- Iack daisy-chain driver

A functional module which ensures that only one Interrupter responds with its STATUS/ID when an Interrupt handler acknowledges an interrupt request.

- Location monitor

A functional module dedicated to monitoring the DTB and issuing on-board signal when an access to the locations it has been assigned to watch occurs.

- System clock driver

A functional module that provides a stable 16 MHz timing signal on the Utility subbus.

- Power monitor

A functional module monitoring the status of the primary power source and signaling in case of power deviations.

3.2.2 VMEbus sub-buses

The various functional modules communicate through five sub-buses.

- Data transfer bus (DTB).

This is one of the buses sitting on the VMEbus backplane[3] and responsible for the binary data transfer between Masters and Slaves.

- Data transfer arbitration bus.

It shares the ownership of the DTB between an Arbiter module and several Requesters.

- Priority interrupt bus.

It generally passes interrupts between Interrupters and Interrupt handler modules.

- Utility bus.

This bus provides a collection of utility functions such as a utility clock and a system reset signal.

- Serial bus.

A two-wire serial bus.

3.2.3 VMEbus bus cycles

Various bus cycles are imposed upon the different sub-buses. The main ones are described below.

- Read cycle

This is a DTB cycle used to transfer 8, 16, 24 or 32 bit of data from a Slave to a Master module during every transaction. The cycle starts as the Master broadcasts an address and an address modifier. If a Slave module has to respond to them, then it retrieves the data from its storage, places it on the data bus and acknowledges the transfer. The cycle is then terminated by the Master.

- Write cycle

This is similar to the read cycle, but the data flow is from Master to Slave module. If a Slave

---

[3] A printed circuit (PC) board with 96 pin connectors and signal paths that bus the connector pins

has to respond to an address or an address modifier broadcasted from the Master, then it stores the data and acknowledges the transfer. The cycle is again terminated by the Master module.

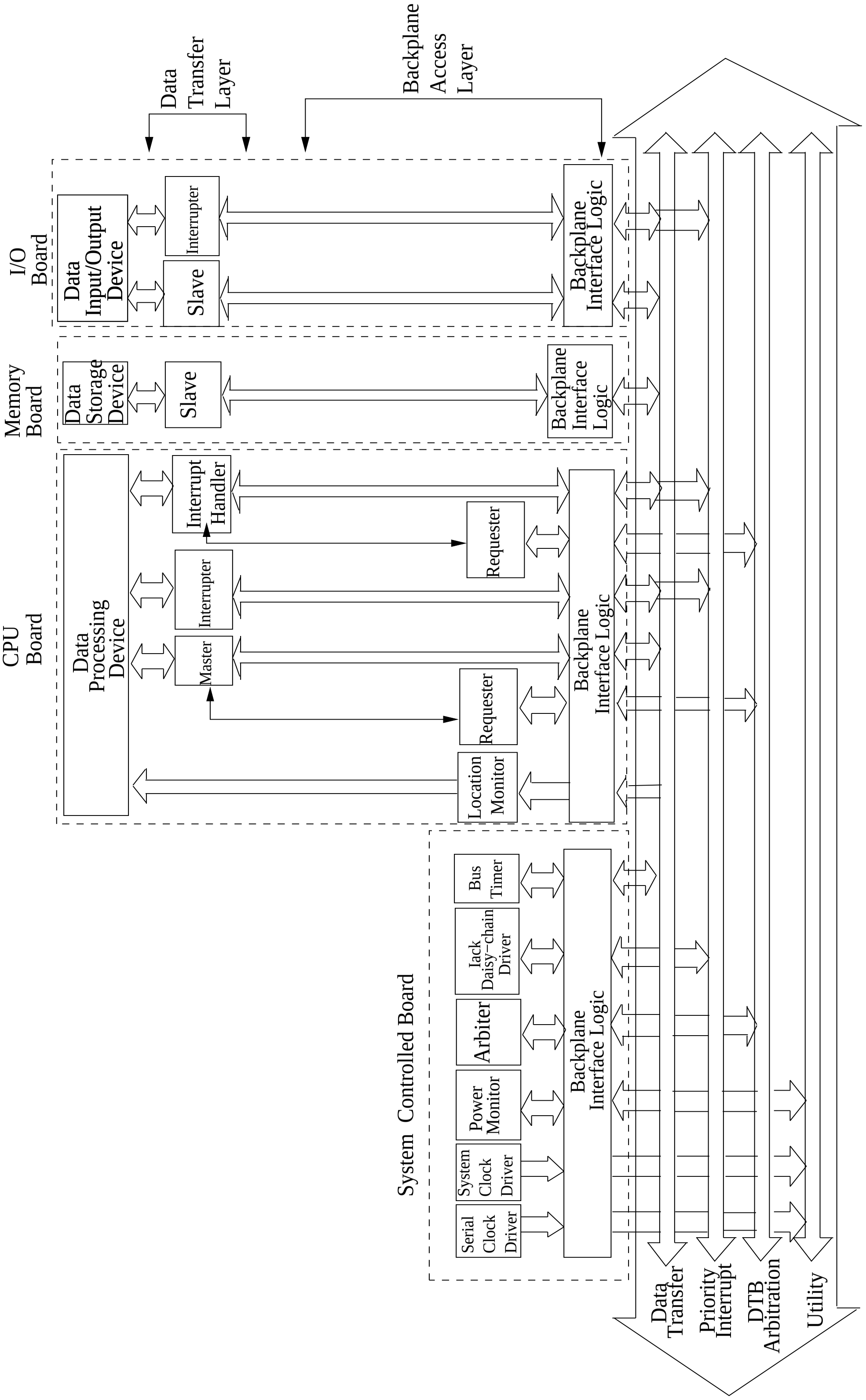

Figure 3.2: Functional modules and buses.

- Block transfer cycle

A bus cycle faster than the usual read/write cycles. It moves a data from 1 to 256 bytes in a block fashion.

- Address-only cycle

A type of cycle that broadcasts an address, but no data transfer occurs.

- Read-modify-write cycle

A DTB cycle used to read from and write to a Slave location, prohibiting any other Master to access it.

- Interrupt acknowledge cycle

A cycle generated by an Interrupt handler module when it detects an interrupt request from an Interrupter and gains control over DTB.

3.3 MBS overview

As mentioned above, MBS stands for Multi-Branch System. It is general purpose data acquisition system developed at GSI, Darmstadt [Esse98]. The software operates with the VME PowerPC platforms (CES RIO2) [Esse97], the GSI developed CAMAC processor board CVC, the ELTEC E6 and E7 VME processors, thus, meeting the requirement to be as hardware independent as possible. It can be configured for various hardware setups and is optimized for fast trigger rates and data throughput. Despite of its name, it is scalable from large hierarchical structured (multi-layered) multi-branch systems [Ydu96] to small single-crate VME or CAMAC single-branch systems. Some of the other Pros are the reliable software, various easy-to-adapt analysing tools (APE[APE], LEA [Esse00], GO4 [Adac01]), multi-analyser capability, existing interface to accelerator control, different triggers. The system can work stand-alone which means that no other computers are necessary to grab the data and store it on a local tape. MBS gives also the possibility to write the raw data to a disk. Data rates up to 3 MB/s are reported [Esse01]. The existing technical assistance at GSI has also to be mentioned.
Some of the laboratories, where MBS is installed outside GSI are: FZD, Berkley (LBL), Braunschweig (PTB), Catania University, TU Darmstadt, Freiburg University, Heidelberg (MPI für Kernphysik), ISOLDE (CERN), Crakow University, Lanzhou University, Leuven University, Madrid University, Marburg University, München (Beschleuniger Labor), TU München, Nikosia University, Rez (Nuclear Physics Institute), Santiago de Compostela University, Wuppertal University, Zürich (ETH).
The total number of the active MBS installations is more than 90 (see Fig. 3.3), and the trend is that it expands with time although difficult to predict exactly how, since the small installations change often.

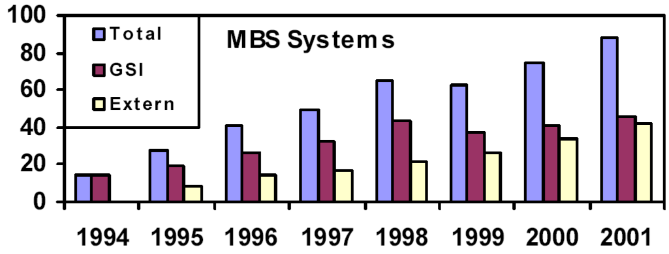

Figure 3.3: The figure after [Esse01] demonstrates the steady increase of the existing MBS installations, in and outside GSI for a given period of time.

3.4 MBS logical model

As already mentioned, MBS may expand from a Single Branch to a Hierarchical Multi Branch System, where each master collecting data from its slaves can be a slave of the next level master. The branch is a memory-mapped-address window with several slots for subevent pipes [Essel96]. The pipe serves as a control structure for a number of subevents and a data buffer as shown in figure Fig. 3.4a). The pipes are accessible from readout and collector tasks. The readout task fills one pipe with subevents. It is triggered externally by a specially designed at GSI trigger module. The collector (event building) task runs on the master CPU and copies the subevents from the pipes event by event into buffers. The events are formatted according to established GSI standard. A chain of events composes a stream. The collector basically polls on two states. The first one indicates when all required subevents are ready and the second one waits for a free buffer stream. The formatted events are further processed from different kind of client/server programs. One of them is the transport server. It operates by polling on the next stream to be filled and by copying it to an active output channel. It also resides on the master CPU and writes events to a locally attached tape or TCP channel. Another important server is the stream server. It supplies samples of data to different analysis programs running remotely which makes it suitable for monitoring purposes. The event server provides filtered events to several analysis clients. The event buffers reach the client according to the filter and selection conditions that has been set. This may turn out inconvenient especially when several analysis clients are simultaneously connected, thus, consuming too much CPU time. To overcome this problem, one optionally may run a stream server. Then a remote event server running from the client side gets connected to it and receives samples of full streams.
A stream is owned only by one task at a time, either by the collector which fills it or by the transport or event server which empties it (see Fig. 3.4b). All connections are utilized through standard TCP sockets.

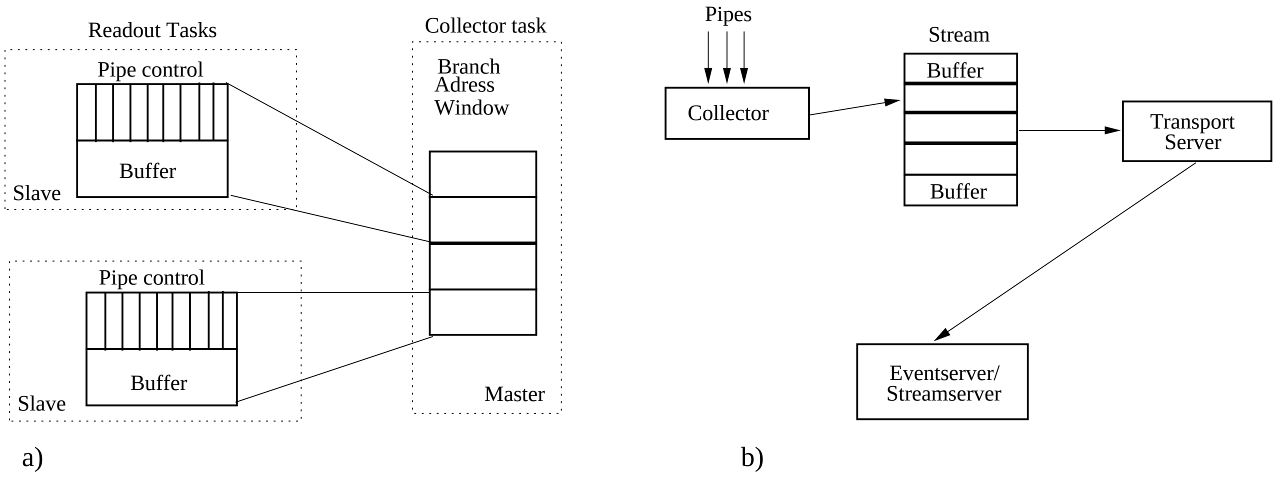

Figure 3.4: Branches and pipes a), Buffers and streams b)

The whole acquisition system can be controlled from one VT like terminal (single node system). All the commands are accepted from a command dispatcher. It serves to fork different tasks and to translate commands to them. A central routine outputs the results from these tasks on the terminal. The terminal output is also redirected to a messager logger which saves it to a log file.

A two node system (see Fig. 3.5) requires that one starts a message server and a command prompter on the master node. The prompter gives commands to start remote dispatchers and message clients. The remote message clients connect to the message server. The prompter sends commands to remote dispatchers. All communications between local tasks are managed by the Lynx message system. The remote tasks are realized through TCP connections. MBS offers some other utilities which will be mentioned here only briefly. The first one is the Information and Help which gives basic command descriptions and supplies the user with some other useful information. The Histogram Manager is a program related to handling of histograms. They are stored in a histogram data base and can be exported (dumped) in ASCII files and imported by different analysis packages.

All parameters which describe the hardware and software setups are kept in text file, which is provided by the user.

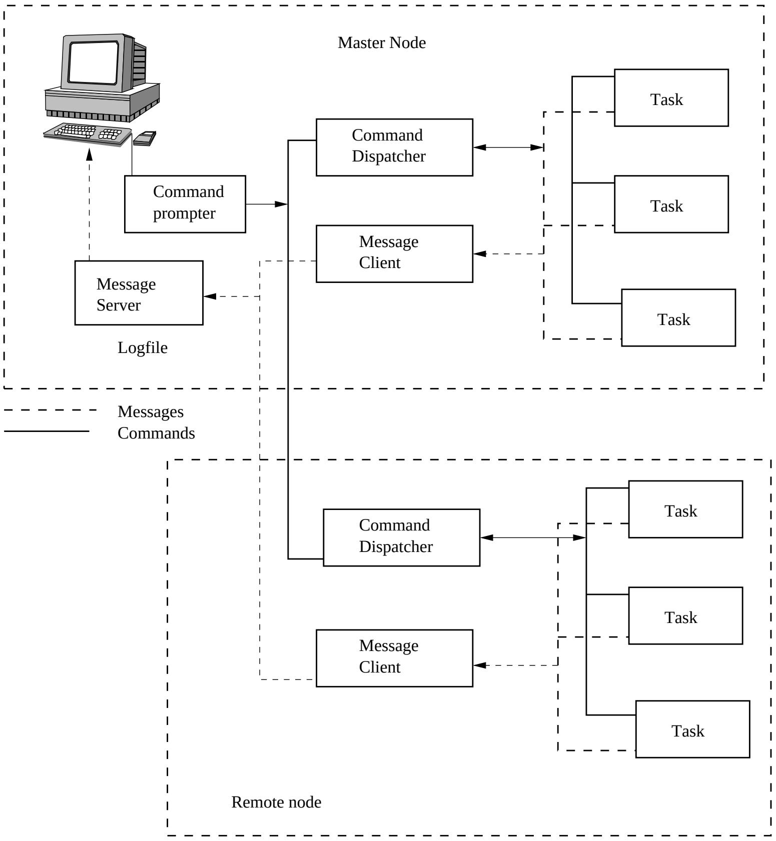

Figure 3.5: Communications between two nodes.

3.5 Trigger and synchronization

MBS meets to a great extend the requirement for hardware independency. Despite of that, there are a few modules which have to be adopted. The main one is the GSI trigger module available for VME, CAMAC and FASTBUS. Here, we are going to dwell shortly only on the main features an usual trigger module provides.

The trigger module manages the synchronization of the readout tasks and the generation of a total dead time (TDT) through a trigger bus. The trigger module (TRIVA 3 VME trigger module implemented for our experiments) controls the GO line of the Trigger BUS (TBUS), thus, starting and stopping the acquisition. There are 15 different triggers. Trigger number 14 is a signal to start the acquisition. It sets the GO bit in the trigger module. Similarly, when a command to stop the acquisition is issued, trigger number 15 is fired and the GO bit is cleared. These numbers are recognized by the readout tasks and the collector. The different trigger types (1-15) are selected through the four Master Trigger ECL-inputs available on the front panel of the trigger module. A simplified diagram which describes only the basic event synchronisation in case of only one trigger module in the system is presented in Fig. 3.6.

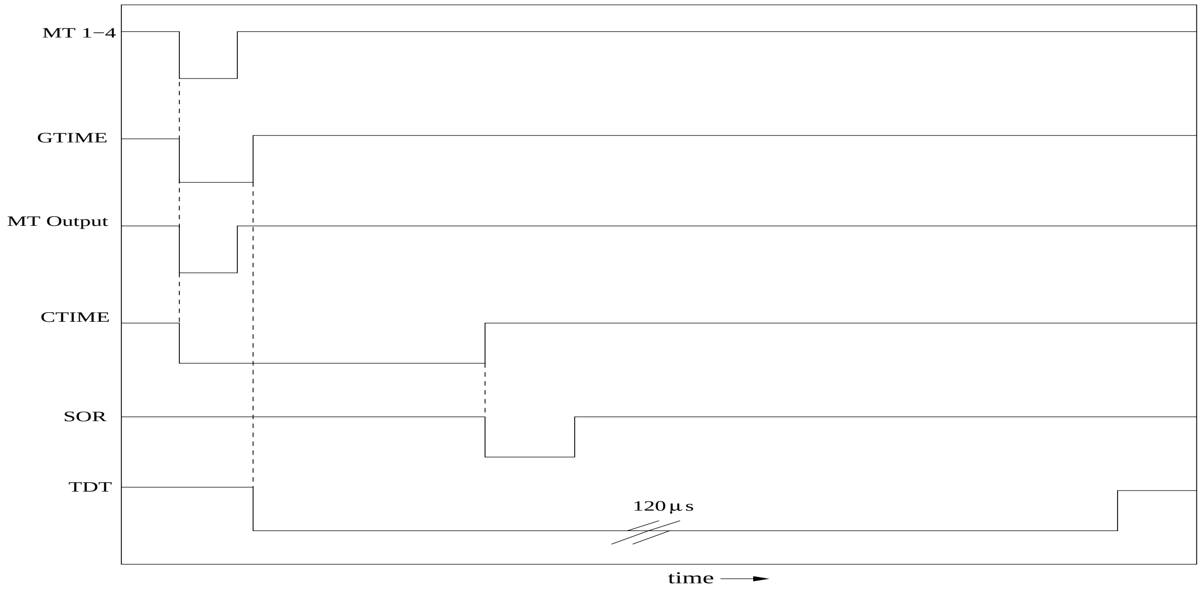

Figure 3.6: Trigger and readout sequence.

The leading edge of the Master Trigger (MT1, MT2, MT3, MT4 - four possible trigger bus signals) initiated by the experiment's fast trigger logic causes a MT (Master Trigger output). Then all the converters in the system digitizing the analog signals from the experiment like the ADCs or Time-to-Digital (TDC) converters start. It is important to mention that the first of the four Master Triggers produces a trigger Acceptance Time Window (GTIME), adjustable in the range from 40-600 ns. In order to be accepted, the other triggers must arrive during this time. Another important moment is the generation of Conversion Time Window (CTIME). It is fired by the first Master Trigger (MT1-MT4) signal and its duration is as long as the slowest converter served by the trigger module needs time for conversion. Its end initiates Start of Read-out (SOR) pulse, beginning the data readout from the converters. The end of GTIME determines the start of the Total Dead Time (TDT) which in our case is in the order of 120 μs. As will be later demonstrated, TDT imposes limitations on the maximal countrate the DAQ can accept.

3.6 Data structure

As already explained, the data taking in our VMEbus based system, happens when only trigger signal by the specially designed for that purpose - TRIVA 3 VME module is issued. The actual readout is accomplished by the RIO2 Power PC through the developed at GSI Multi-Branch

System. Most of the implemented data processing modules (TDCs, ADCs) are from the company CAEN[4]. The reason for that is twofold: the CAEN Nuclear Division is acknowledged as one of the leading companies providing a complete set of Front-End/Data Acquisition modules which comply with the IEEE Standards for Nuclear and Particle Physics, and second but not least - the relatively low cost per module channel. The retrieved from these modules data is packed in special format in the form of data words - 32 bit each. Since the data taking structure is similar for the types of CAEN VME modules implemented in our experiments, we will only overview the case of the CAEN VME V775 TDC. Its data output as displayed in Fig. 3.7, consists of Event header, Event data and End of block (EOB) data words.

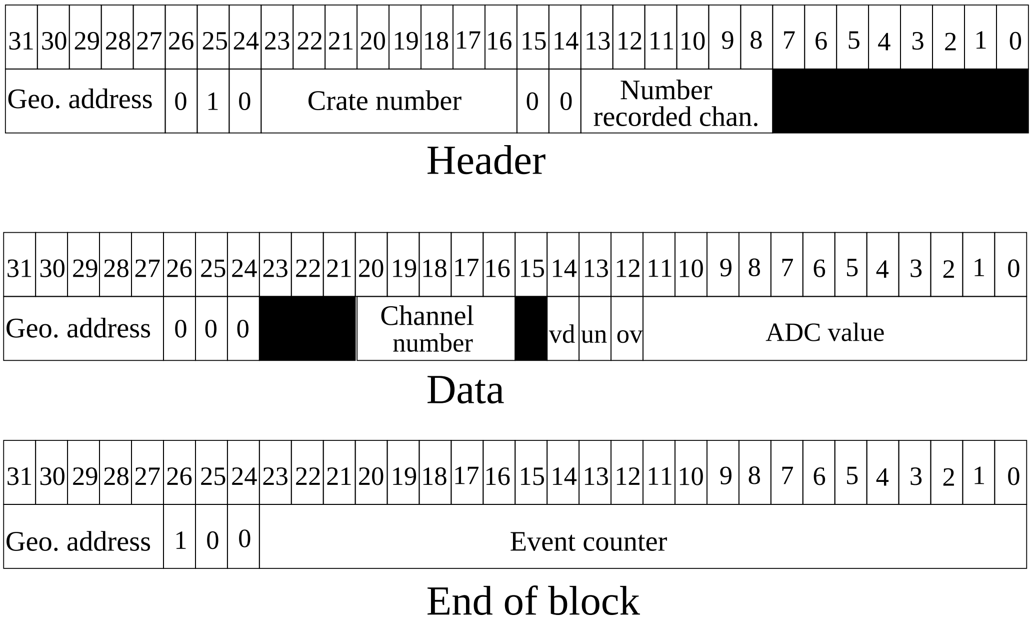

31	30	29	28	27	26	25	24	23	22	21	20	19	18	17	16	15	14	13	12	11	10	9	8	7	6	5	4	3	2	1	0
Geo. address					0	1	0	Crate number								0	0	Number recorded chan.						■							

Header

31	30	29	28	27	26	25	24	23	22	21	20	19	18	17	16	15	14	13	12	11	10	9	8	7	6	5	4	3	2	1	0
Geo. address					0	0	0	■			Channel number					■	vd	un	ov	ADC value											

Data

31	30	29	28	27	26	25	24	23	22	21	20	19	18	17	16	15	14	13	12	11	10	9	8	7	6	5	4	3	2	1	0
Geo. address					1	0	0	Event counter																							

End of block

Figure 3.7: Event structure of the output buffer organised in 32-bit words.

The last five bits (27-31) of the different types of data words point usually to the geographical address (particular VME slot) of each individual module. Bits from 24 to 26 are reserved for the type of data word - Event header, Event data or EOB. The header contains additional information about the crate number and the number of converted channels. Each data word holds extra the number of the fired channel and the converted from the TAC session ADC value. Bits 14, 13 and 12 are specific to whether the datum is valid or not, whether it is over a certain threshold fixed in a relevant register[5], and if the ADC is in overflow condition. The EOB data word supplies the amount of the stored events[6] as well.

An example of a multi-event buffer data structure is given in Fig. 3.8. The first event written in the active event buffer is relative to the N-th gate. Two channels (3 and 5) are recorded. The stored event is constituted by header, the data relative to the two channels and EOB. During gate N+1, channels 0, 7, 10 are fired. The saved event again consists of header, the data relative to the three active channels and EOB.

A special hardware register allows to access the multi-event buffer and readout the converted

---

[4] CAEN S.p.A.,Via Vetraia 11, 55094 Viareggio, Italy.

[5] V775 TDC like all the other CAEN VME modules are fully programmable and allow for a thorough user control. Specific user values can be set in special registers defined in the address space of the module.

[6] As an event is considered the presence of a TDC gate signal.

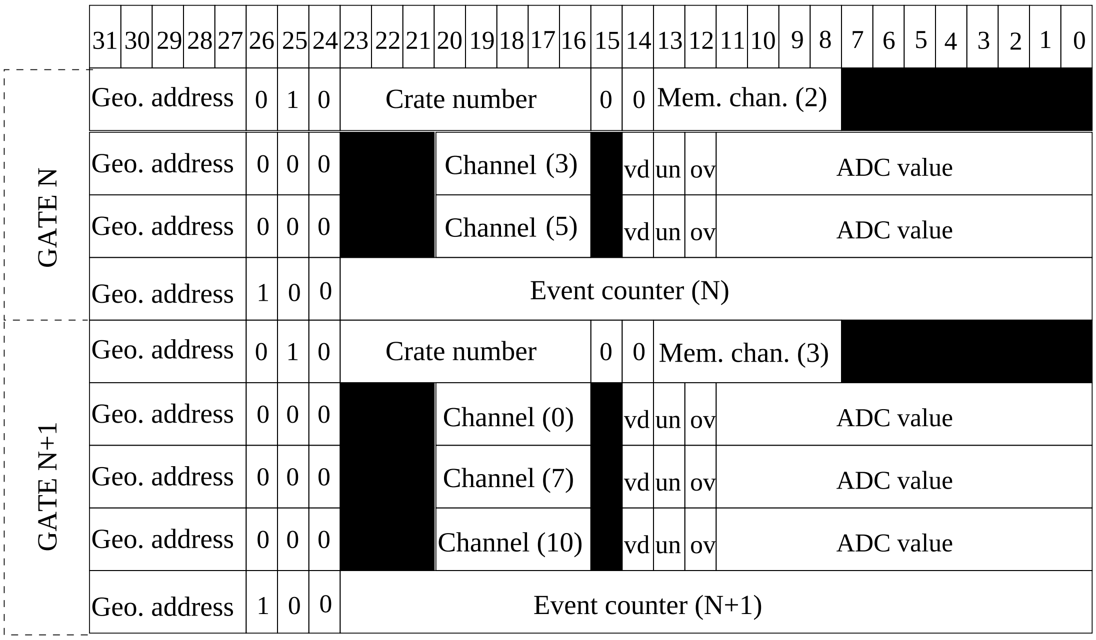

Figure 3.8: Multi-event buffer data structure example.

values. It is positioned at a certain offset relative to a user predefined module base address[7].

3.7 Dead time of non-paralyzable DAQ

When speaking about DAQ, one has also to calculate the dead time effects. Each element of a detector system has its own dead time, but it is quite often the case, when the electronics is responsible for the larger part of the effect. Two general cases are distinguished: extendable or non-extendable dead times. They are also known as the paralyzable or non-paralyzable case [Leo94, Meil75]. When the extendable case is present, the arrival of a second event during the dead time extends its duration by adding on its dead time τ starting from the moment of its arrival (see Fig. 3.9). So in case of a high count rate, a prolonged period is produced during no event is accepted. In contrast, the non-paralyzable case corresponds to a DAQ which remains totally insensitive during the dead time period. It becomes active again only then, when a time τ is elapsed.

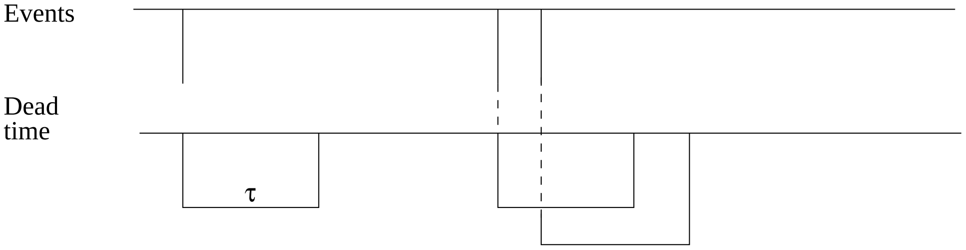

Figure 3.9: Paralyzable case.

---

[7] The base address is user adjusted by rotary switches positioned at the back plane of the VME module.

Supposing that N is the true count rate and L events are registered for a time T, then the true number of counts is:

$$NT = L + NL\tau \tag{3.1}$$

Therefore, the ratio between the number of recorded and delivered events for an unit time determines the dead time fraction R (see Fig. 3.10):

$$R = \frac{1}{1 + N\tau} \tag{3.2}$$

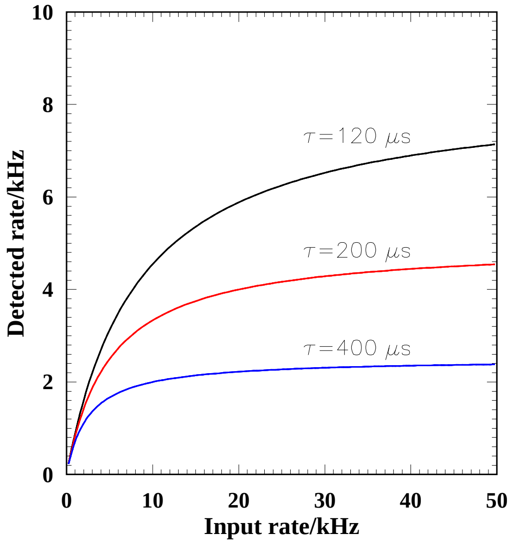

Figure 3.10: The figure after [Wagn05b] demonstrates the effect of the different dead times on the input and detected count rates. The dead time of the MBS DAQ is determined by the TDT of the TRIVA VME trigger module, which is in the order of 120 μs.

Presuming that the incident count rate is 6000/s at a dead time of 120 μs, then the dead time fraction is 58 %.

3.8 Online Control

In order to facilitate the control over the MBS DAQ, a GUI interface program, based on the Tcl/Tk[8] language has been developed. As one can see from Fig. 3.11, it accepts important VME module parameters routed to a specific MBS user setup file. On each start of the DAQ, the modules settings are translated automatically to the specific modules hardware registers. They remain constant until new changes through the GUI program are imposed. The implementation of the GUI interface program is found very convenient and time saving method, since it allows for a relatively unexperienced user to convey important DAQ parameters without the

---

[8] Tcl (Tool Command Language) is a very powerful dynamic language, suitable for desktop and web applications. Tk is a graphical user interface toolkit. It is the standard GUI not only for Tcl, but for many other dynamic languages, producing applications which run unchanged across Linux, Windows and Mac Os.

necessity to poke in a complicated C code and recompilation. This turns out to be an important argument especially during experiments, where the flexibility and the fast response of the experimenter are important issues.

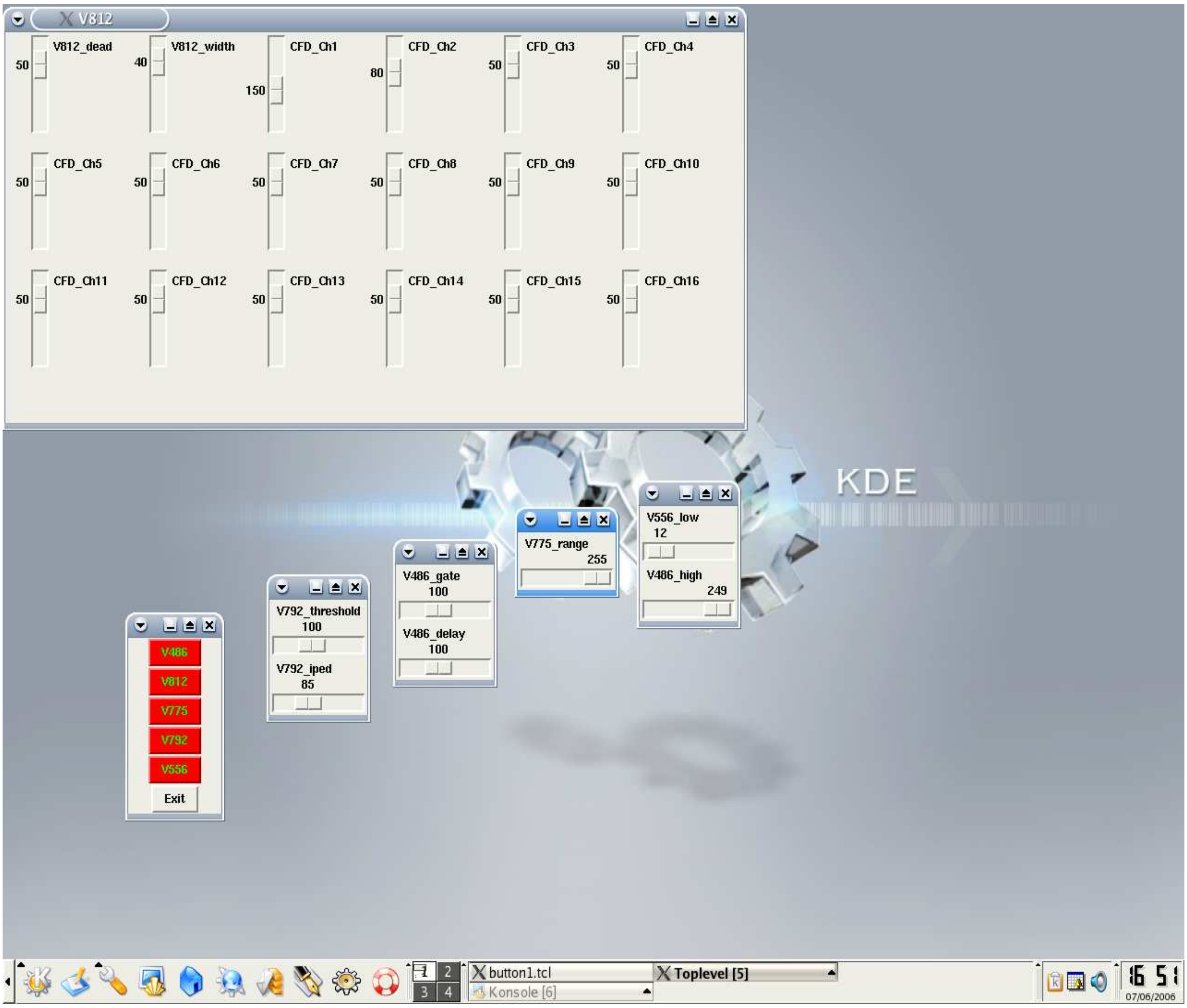

V812_dead 50
V812_width 40
CFD_Ch1 150
CFD_Ch2 80
CFD_Ch3 50
CFD_Ch4 50
CFD_Ch5 50
CFD_Ch6 50
CFD_Ch7 50
CFD_Ch8 50
CFD_Ch9 50
CFD_Ch10 50
CFD_Ch11 50
CFD_Ch12 50
CFD_Ch13 50
CFD_Ch14 50
CFD_Ch15 50
CFD_Ch16 50
V792_threshold 100
V792_iped 85
V486_gate 100
V486_delay 100
V775_range 255
V556_low 12
V486_high 249

Figure 3.11: GUI interface program.

Another development, which is also worth mentioning is the online web monitoring over the DAQ status. This is enabled through a complex Linux tcsh script generating a web page and started automatically each minute by a Cron job. It reads the MBS log files and provides the user with information of the initial start and stop of the DAQ as well as with the current VME module settings taken from the output of the above described GUI program (see Fig. 3.12).
The status of each separate VME module (the fired channel and the specific value it has delivered) is also regularly reported. This is utilised through dedicated C programs which serve their output to the permanently running Linux script. We manage also to retrieve the current

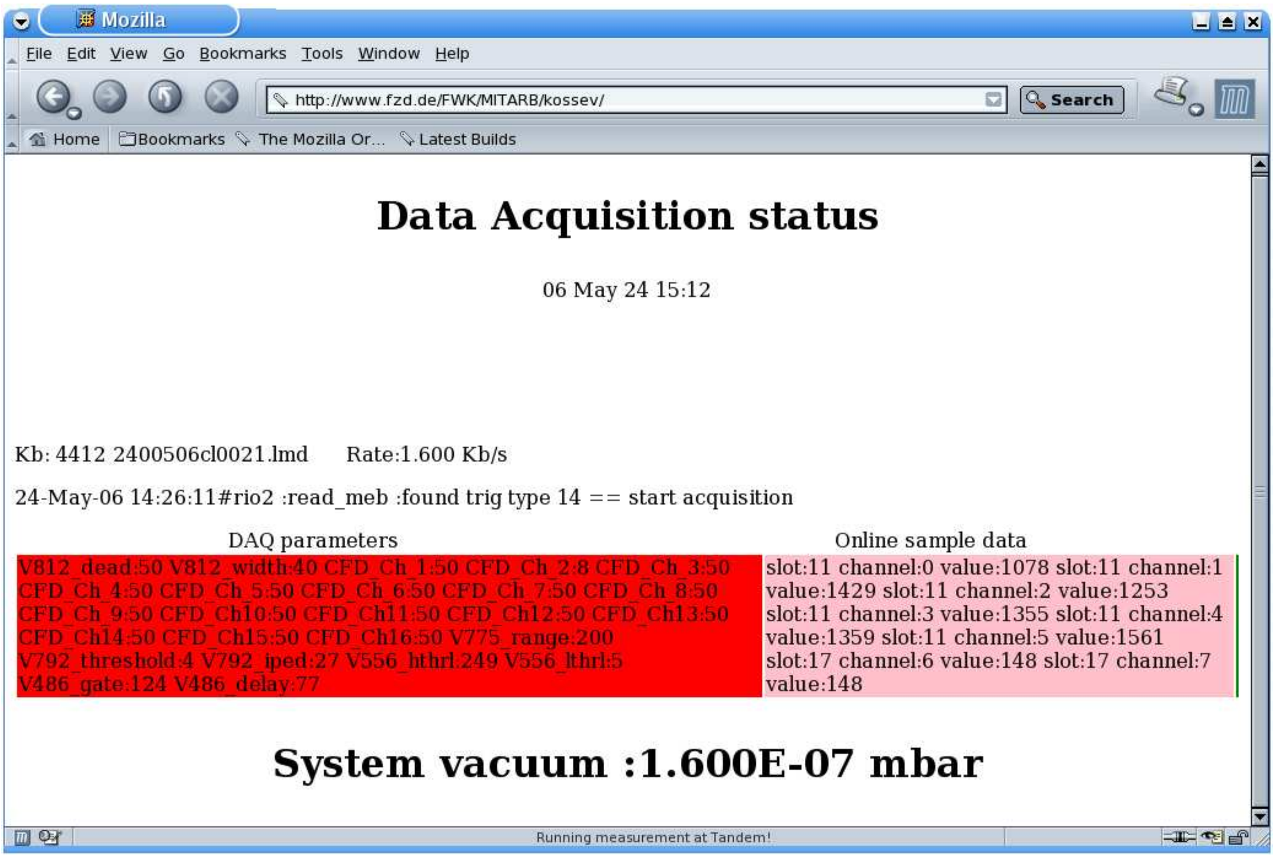

Data Acquisition status

06 May 24 15:12

Kb: 4412 2400506cl0021.lmd   Rate:1.600 Kb/s

24-May-06 14:26:11#rio2 :read_meb :found trig type 14 == start acquisition

DAQ parameters	Online sample data
V812_dead:50 V812_width:40 CFD_Ch_1:50 CFD_Ch_2:8 CFD_Ch_3:50 CFD_Ch_4:50 CFD_Ch_5:50 CFD_Ch_6:50 CFD_Ch_7:50 CFD_Ch_8:50 CFD_Ch_9:50 CFD_Ch10:50 CFD_Ch11:50 CFD_Ch12:50 CFD_Ch13:50 CFD_Ch14:50 CFD_Ch15:50 CFD_Ch16:50 V775_range:200 V792_threshold:4 V792_iped:27 V556_hthrl:249 V556_lthrl:5 V486_gate:124 V486_delay:77	slot:11 channel:0 value:1078 slot:11 channel:1 value:1429 slot:11 channel:2 value:1253 slot:11 channel:3 value:1355 slot:11 channel:4 value:1359 slot:11 channel:5 value:1561 slot:17 channel:6 value:148 slot:17 channel:7 value:148

System vacuum :1.600E-07 mbar

Figure 3.12: Online web monitoring.

system vacuum values. That turns out to be crucial for long term measurements, where one has to make sure that the vacuum conditions are always optimal.

Chapter 4

Measurements with radioactive alpha source

This chapter gives an overview of the first test experiments performed with the TOF spectrometer. Different measurements with α-particle source, demonstrating the overall performance of the setup will be presented.

4.1 First test measurements with position-sensitive multichannel-plate detector

As already discussed, for the detection of the fission fragments produced by the high-intensity photon-beam from Bremsstrahlung at ELBE, position sensitive detectors will be used. In order to study the performance of these detectors, experimental investigation and data analysis have been carried out.

An intense and a broad beam of α-particles bombards a pattern metal plate with holes (see Fig. 4.1). Only those particles penetrating the holes reach the position sensitive detector (described in Chapter 2) and form the mask image [Kose03].

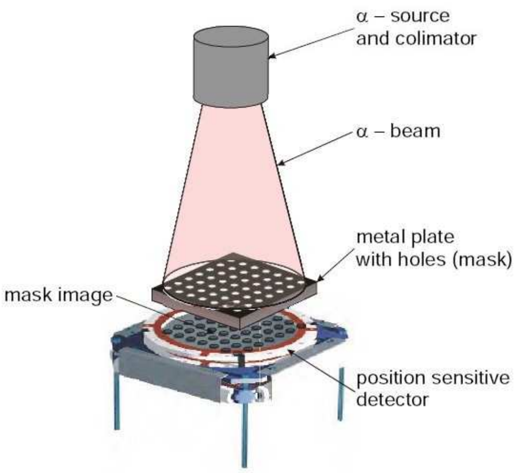

Figure 4.1: Experimental setup.

The position of the detected particles is encoded by the signal arrival time difference at both ends of each parallel pair delay-line of the position sensitive anode, for each dimension independently. The single path signal propagation time on the delay-line anode is about 0.71 ns/mm corresponding to 1.42 ns/mm in the 2D image. The time sequence of the signals is measured by V775 TDC (Time-to-digital converter) VME module and recorded by MBS DAQ. A simplified diagram of the data collecting scheme is represented in Fig. 4.2.

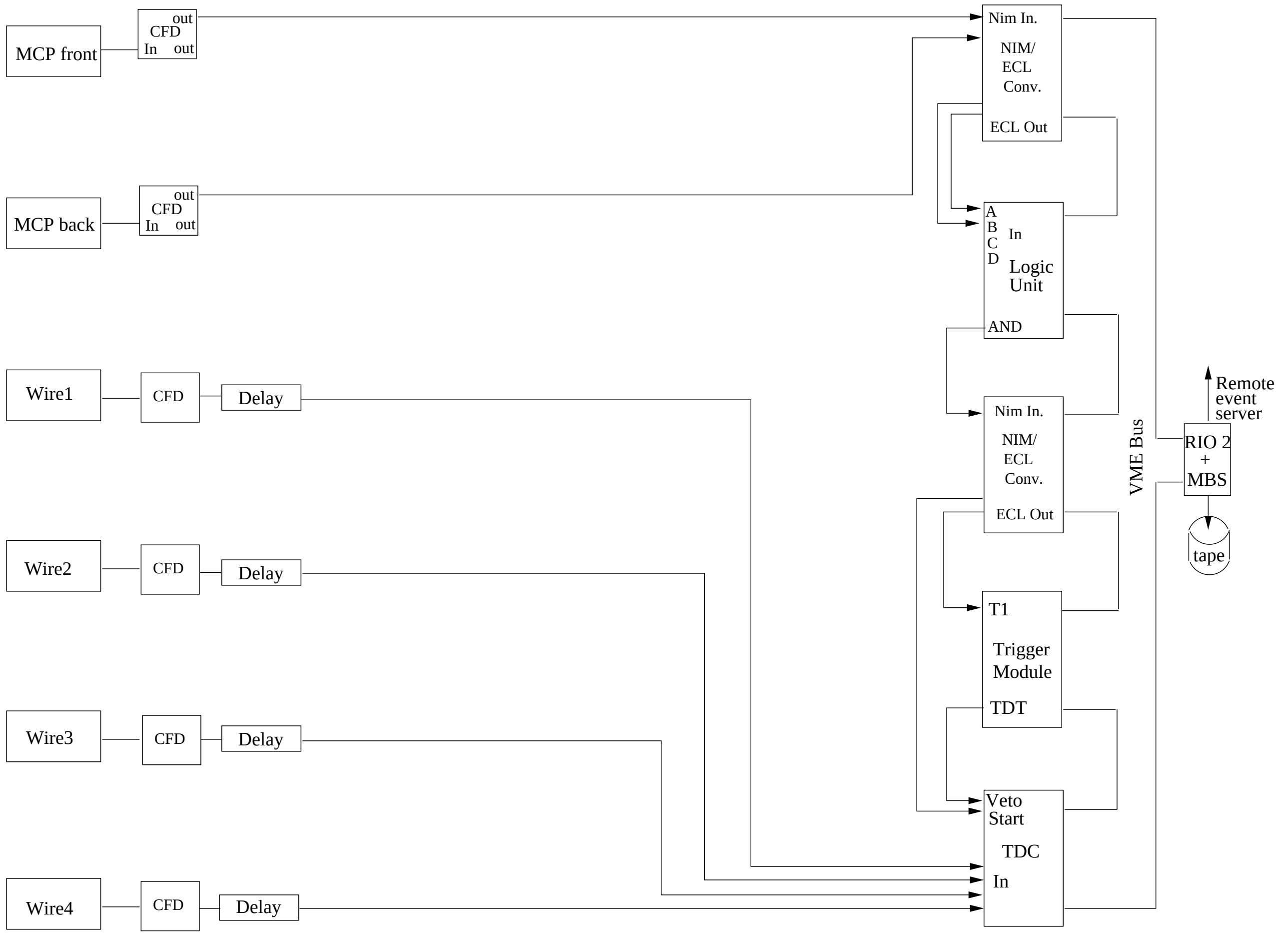

Figure 4.2: Readout scheme.

As time reference (start of the CAEN V775 TDC VME module), both MCP back and front signals in coincidence are taken. This ensures that the system is triggered only by true alpha events while strongly suppressing the uncorrelated background noise. The coincidence logic is utilised through a CAEN VME V512 logic module. After proper delay, the MCP front and back together with the anode wires logic signals produced by the CFDs, initiate stop signals in the TDCs. Data analysis of the collected lmd (list mode data) files is performed by APE.
As one could expect, the sum of the wires arrival times is nearly constant. The inaccuracy in the time sum spectrum would determine the position resolution of the system, which is found to be around 1 mm. This is shown in Fig. 4.3.
From the single wire spectra, the 2D mask image is obtained as depicted in Fig. 4.4. The detector setup is operated inside a vacuum chamber set at about 3.4×10^{-8} mbar.

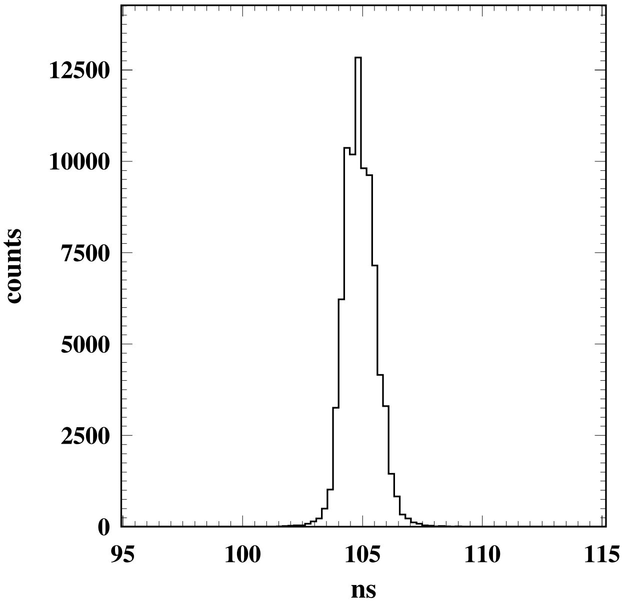

Figure 4.3: Time sum spectrum. Since the signal propagation time on the 2D delay-line anode is 1.42 ns/mm, the obtained position resolution referenced to the FWHM of the time sum peak is around 1 mm.

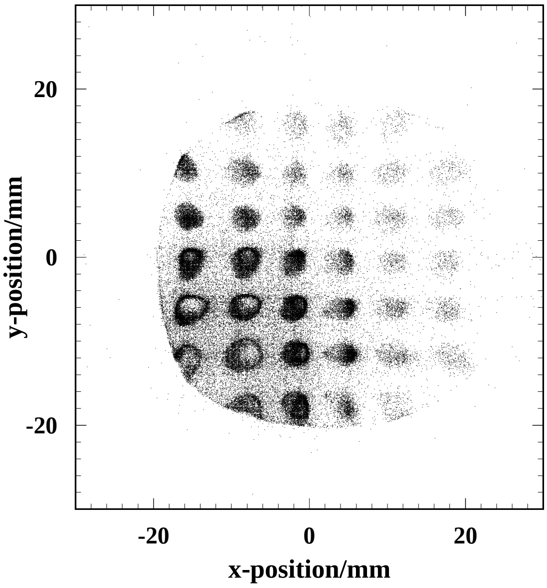

Figure 4.4: Image of a pattern metal plate with holes separated by 6 mm (center-to-center). The measurement are performed with α-particles from a mixed (^{239}Pu, ^{241}Am, ^{244}Cm) source. The left down image corner is stronger illuminated because of a slight MCP detector tilt. Some of the hole pattern images are blurred, which is probably due to distortions of the wires timing signals.

4.2 Measurements with electrostatic mirror and the accelerating potential impact

The method of the electrostatic mirror detection described in Section 2.4 is based on the SEs emission from a thin, negatively biased foil, when heavy particles are passing through. The SEs are then accelerated by the positive potential applied at the foil grids. The accelerating potential is defined as the potential difference between the grids and the foil. After acceleration, the electrons are deflected by the electrostatic mirror directly on the MCP surface. Its first part (mirror front) has the same positive potential like the electrostatic grids. This provides field free region between the foil grids and the mirror front part. The back side of the mirror (mirror back) stays at high negative bias (2500 - 3000 V), thus, accomplishing the actual deflection. Aluminised 300 μg/cm^2 PETP foil is employed for the purpose of our measurements. The setup is depicted in Fig. 4.5. Since we are detecting electrons, the MCP detector is operated in the so-called "electron detection" mode (for details see Subsection 2.4.6).

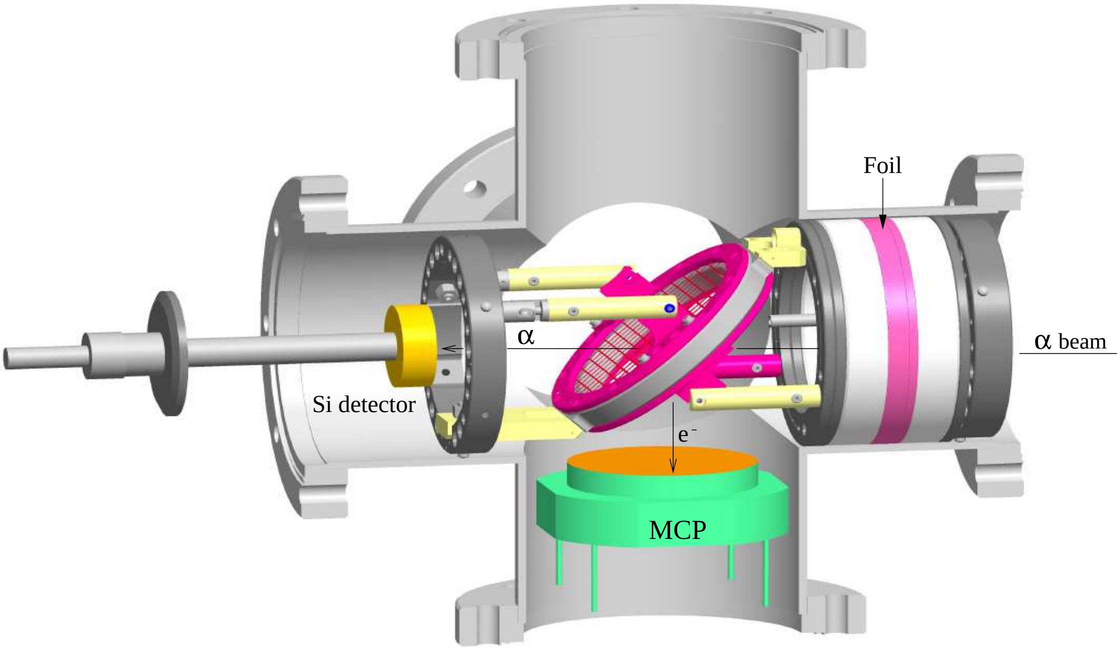

Figure 4.5: Measuring setup with electrostatic mirror. The device consisting of MCP detector, SE foil, electrostatic mirror and Si detector is operated in the so-called "forward" mode, since only the SEs emitted in beam direction are being detected.

We used α-particle source with energies from 4.72 MeV up to 7.88 MeV for our measurements. The setup comprised of a TOF-detector (SE foil, electrostatic mirror, MCP) and an EURISYS silicon detector with a sensitive area of 200 mm^2 is operated in coincidence. The coincidence technique allows us to collect those events on the position-sensitive anode which are initiated by α-particles only. The analysis of the obtained data is accomplished by software gating the events on the 2D-anode with the ADC counts retrieved from the silicon detector. Therefore, the accumulated 2D images are merely the projection of the silicon detector surface. At small accelerating potentials, the effect of the large SE angular spread becomes obvious as shown in

Fig. 4.6 a). Increasing further the accelerating voltage, contributes to the image squeezing due to the minimised SE angular spread in both x and y directions. The effect is demonstrated in Fig. 4.6 b), c), d).

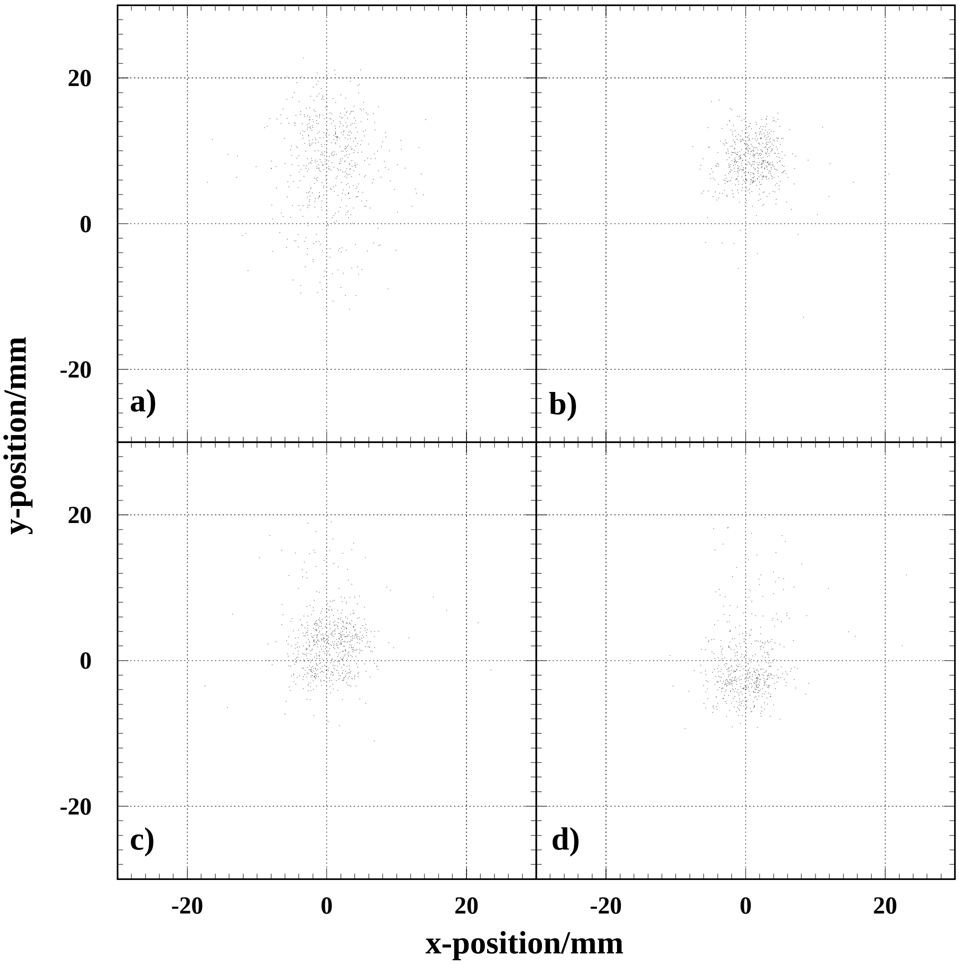

Figure 4.6: Shift of the electron spot on the position sensitive anode due to the different accelerating potentials: 0.3 kV a), 2 kV eV b), 3.7 kV c) and 4.8 kV d).

4.3 Efficiency measurements with α-particles

One of the important characteristics of the TOF detector is how efficiently it detects ions with different Z number. As already mentioned, the SE emission is a surface effect, involving only a very thin target foil material. The obtained output signal and SEs yield are proportional to the energy loss dE/dx of the incoming ion particles. So, the number of the emitted SEs is a function of the projectiles nuclear charge. This would imply, that heavier projectiles produce more SEs in the forward and backward hemisphere. The SEs emitted in the backward hemisphere have lower energy component compared to those emitted in forward direction (see Table 4.1).

Projectile	Alpha particles 9.48 MeV/u	Alpha particles 1.5 MeV/u
2π forward		
SEs $<$ 230 eV	5.7 (89%)	2.4 (86%)
SEs $>$ 230 eV	0.7 (11%)	0.4 (14%)
2π backward		
SEs $<$ 230 eV	3.0 (98%)	1.9 (96%)
SEs $>$ 230 eV	0.09 (2%)	0.07 (4%)

Table 4.1: Table after [Saro96], showing the number of the forward and backward hemispheres emitted SEs by α-particles for a 10 μg/cm^2 carbon foil.

The experimental setup and its principle of operation is the same as given in Fig. 4.5. The MCP detector discriminator thresholds are set just above the noise level. The efficiency is taken to be the ratio of the MCP anode counts over the α-particle counts in the silicon detector as a function of the applied accelerating voltage. The method consists of fixing some positive potential (+250 V) on the acceleration grids and stepwise applying negative bias on the 300 μg/cm^2 PETP foil for SE production while the mirror back side is negatively biased (-2.7 kV). Efficiency measurements for forward, as well as for backward (electrostatic mirror turned to 180°) emitted SEs have been performed [Nank04b]. The results are presented in Fig. 4.7. The efficiency of the silicon detector for α-particles is presumed to be 100 %.

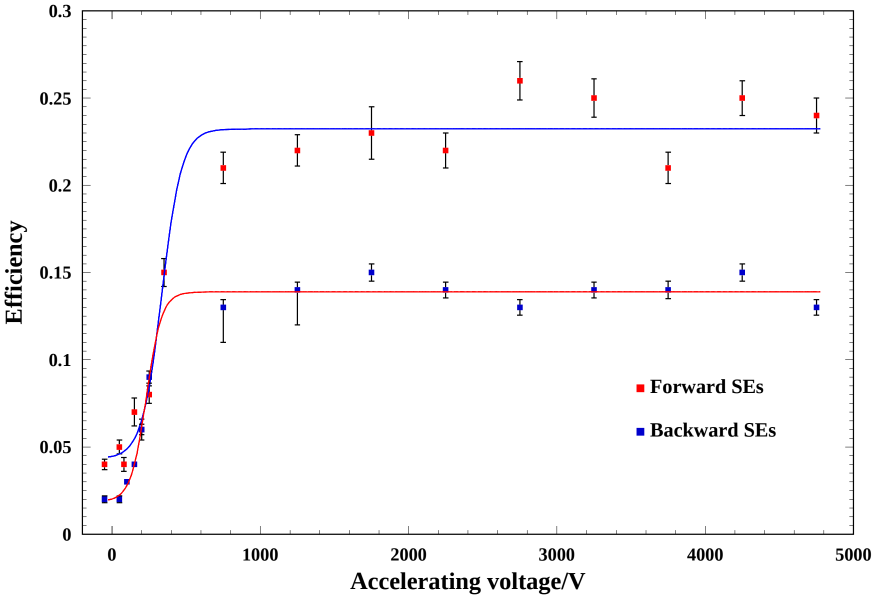

Figure 4.7: Detection efficiency for forward and backward emitted SEs as a function of the applied accelerating voltage.

We have to emphasize, that the detection efficiency of the considered TOF detector unit depends on the conditions for SE emission from the foil, the design of the detector and the parameters

of the MCP. The mostly used MCP detectors nowadays, possess insensitive areas of about 40%. This fact has two important sequences. First, almost half of the SEs do not penetrate into the MCP channels and do not create electron avalanches. Second, ternary electrons are emitted from the insensitive part of the channel plate which after a small loop have the probability to hit an active detector channel and produce a second pulse delayed by a few nanoseconds.
From Fig 4.7, one sees that a stable detection efficiency is reached at an accelerating potential of about 1 kV. This agrees well with the results reported in Ref. [Eras85]. The ratio between the forward and backward setup efficiencies taken in the saturated area approximates the ratio between the number of the liberated electrons in forward and backward direction as presented in Table. 4.1 for the SEs < 230 eV case. The larger error bars for the backward emitted electrons arise from the fact, that for this particular measurement the MCP detector sits 10 mm closer to the electrostatic mirror, thus, opening a larger solid angle. This affects the efficiency at small accelerating potentials, where the angular spread of SEs is large.

4.4 Position resolution of the Time-of-Flight spectrometer

In a real photo-fission experiment, the position information from the delay-line anode will be used to correct the TOF spectrum for different flight paths due to the initial angular distribution of the particles. In order to determine the position resolution of the setup, an experiment as depicted in Fig. 4.8 with α-particles has been conducted [Kose04].

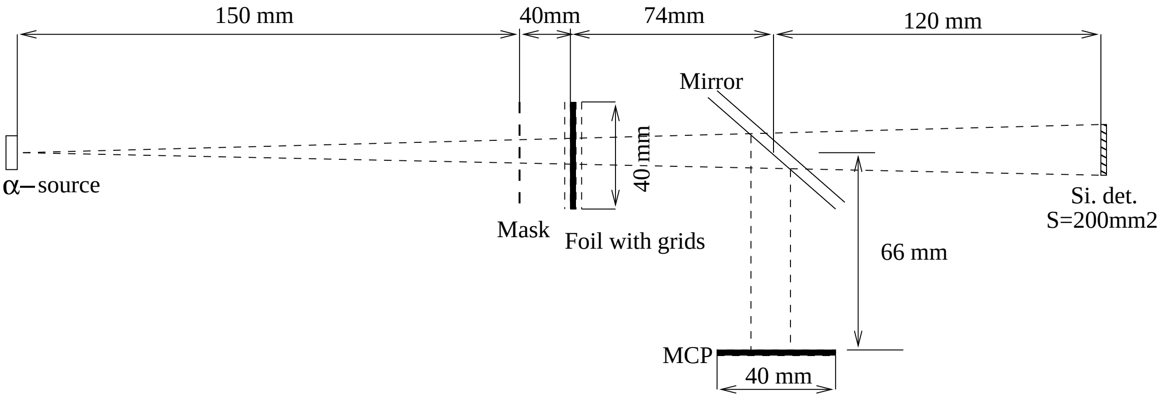

Figure 4.8: Measuring setup showing the geometrical conditions at which the experiment is performed. A mask with several apertures having diameter of 2 mm and separated by 4 mm (center-to-center) is installed in front of a thin 300 μg/cm^2 PETP foil. Only those particles emitted from the mixed (^{239}Pu, ^{241}Am,^{244}Cm) α-source passing through the mask holes could drive SEs out which after acceleration in an electrostatic field of more than 7 kV/cm are deflected by the electrostatic mirror. In such a way, a projected mask image is formed on the position-sensitive MCP detector. The α-particles are detected by a silicon detector in coincidence with the signals from the MCP stack.

An example mask image on the MCP anode is displayed in Fig. 4.9.

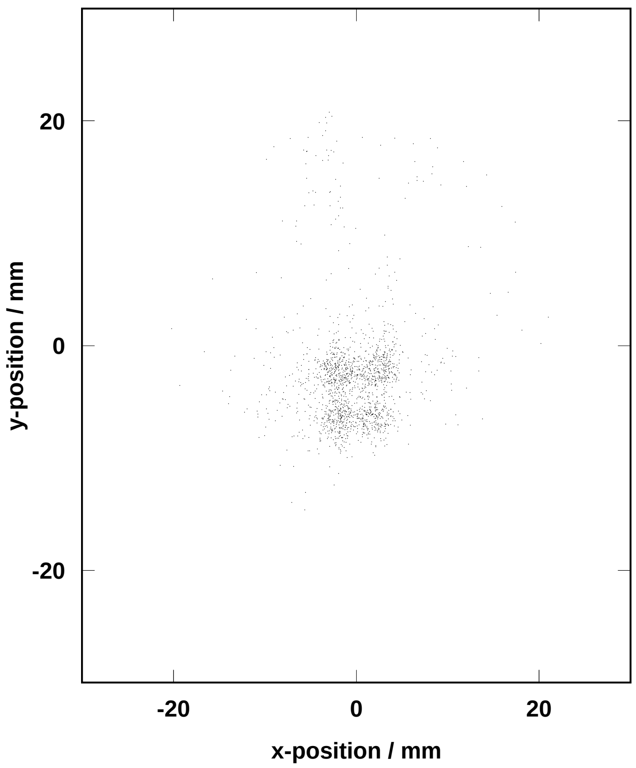

Figure 4.9: The 2D image shows projection of four apertures. As expected, the accumulated mask structure is dependent upon the solid angle determined by the silicon detector surface.

Figure 4.10 demonstrates that the position resoulution of such a device is limited by the spread of the emitted electron's velocity vectors to several mm [Kose04].

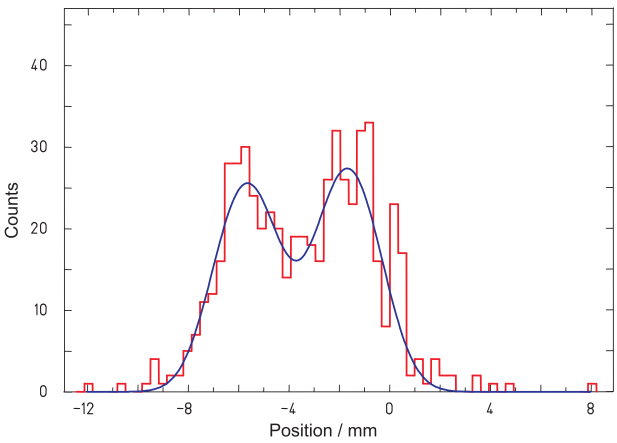

Figure 4.10: Projection of events on the y axis showing that the position resolution obtained with a Gaussian fit convoluted with a box is around 2±0.3 mm (FWHM).

It is shown that the position resolution of the setup may be improved by means of electrostatic lenses [Nank04a].

4.5 Setup for Time-of-Flight measurements

In order to learn more about the timing capabilites of the TOF spectrometer, a test setup as given in Fig. 4.11 is assembled. It basically consists of two identical TOF detectors, operated in the so-called “forward” mode. Particles, ions or fission fragments travelling in the system produce consequent signals in the first and second detector. The quality of the obtained timing spectrum supplies us with important information about the overall performance of the setup.

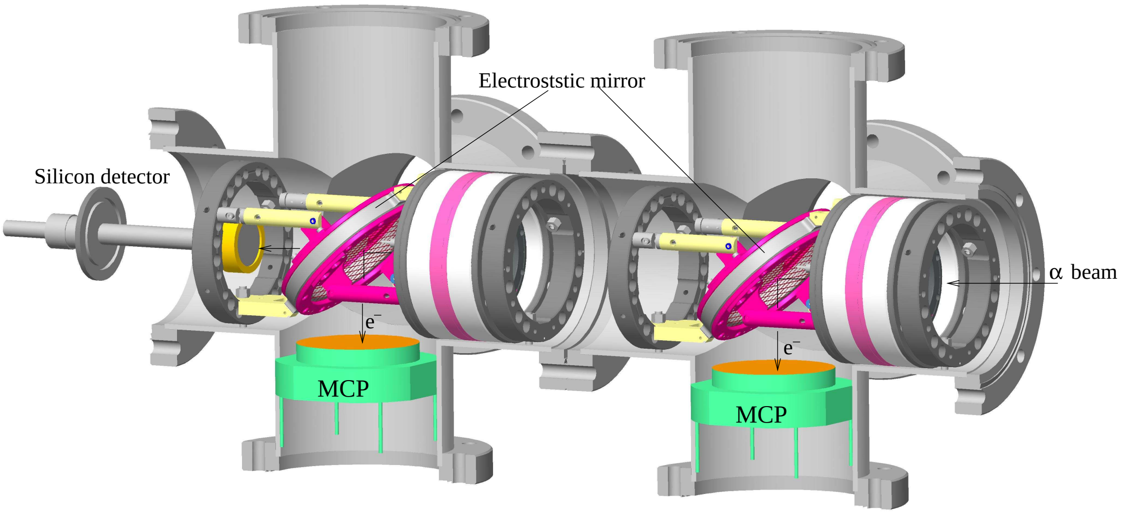

Figure 4.11: Overview of the experimental TOF setup. The two 300 μg/cm^2 PETP foils for SE production are positioned at a distance of 27 cm. Approximately 19 cm away from the second foil sits a silicon detector. The whole device is operated in a chamber set at about 10^{-8} mbar.

For the purpose of our test measurements, a mixed (^{226}Rn, ^{222}Rn, ^{210}Po, ^{218}Po, ^{214}Po) α-source is implemented. The silicon detector (EURISYS, 200 mm^2) is operated in coincidence with the two MCP detectors. This correlation additionally enables the suppression of undesired events caused by noise. The readout scheme and a time diagram of the readout signals are schematically represented in Fig. 4.12 and Fig. 4.13. The logic signals from MCPI and MCPII are fed into a VME CAEN V512 logic module. It initiates a DAQ trigger through a CAEN V512 VME NIM-ECL translator only if they come in coincidence. The trigger signal produces a gate with the help of ORTEC GG8010 Gate-and-Delay module directly supplied to an CAEN V555 VME ADC, accepting signals from the silicon detector. All the other timing signals coming from the anode wires and the MCPS, after proper delay are recorded by the CAEN V775 VME TDC. The represented readout sequence allows for simultaneous coincidence measurements between the two MCP detectors, anode wires and the energy signals derived from the silicon detector. It is also important to point out that the cable lengths and the applied electronics (analog plus digital) are chosen such as to be identical for both MCP branches.

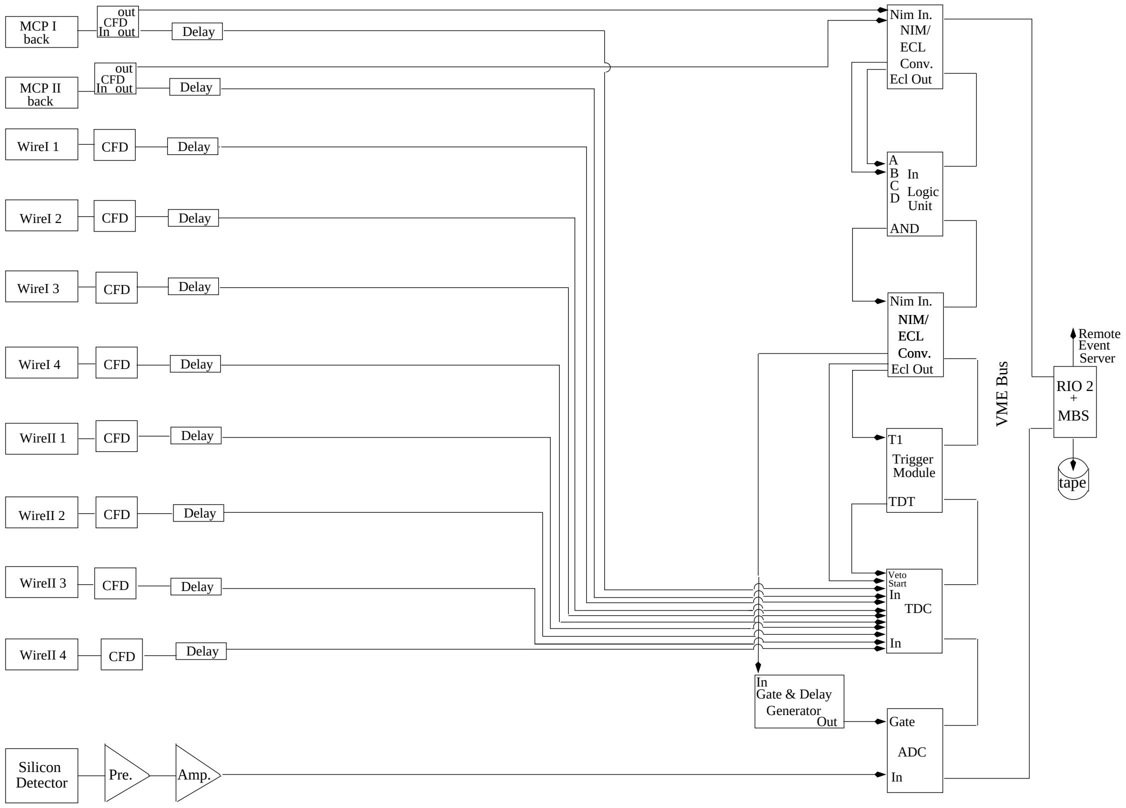

Figure 4.12: The readout scheme.

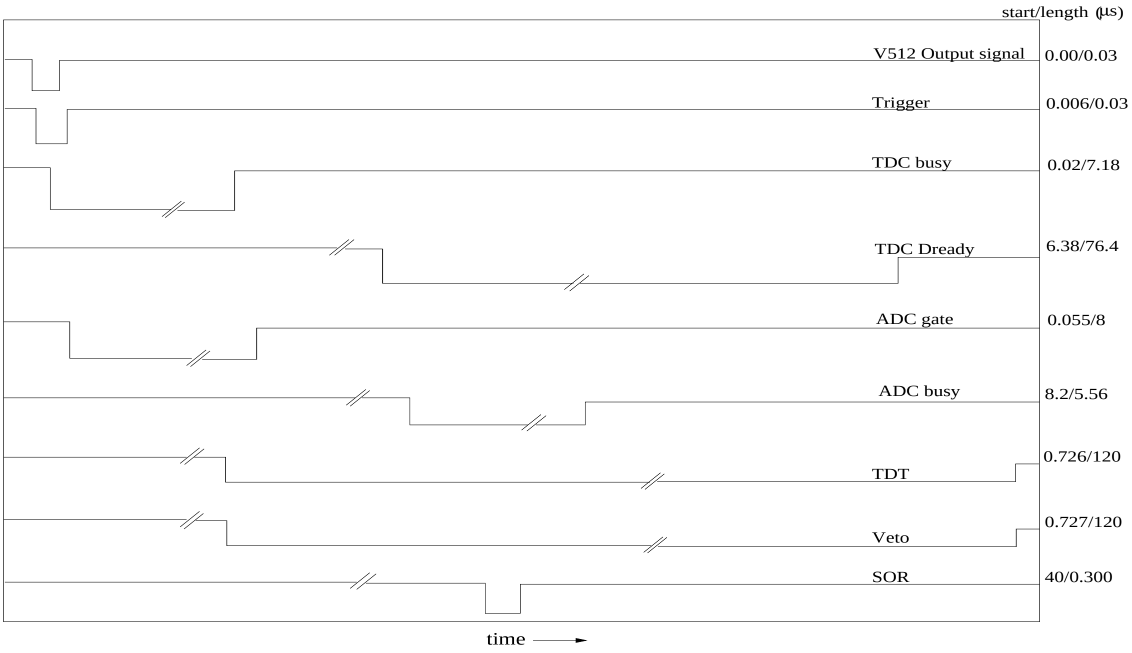

Figure 4.13: Time sequence of the readout signals.

Two resulting spectra - energy and timing are shown in Fig. 4.14.

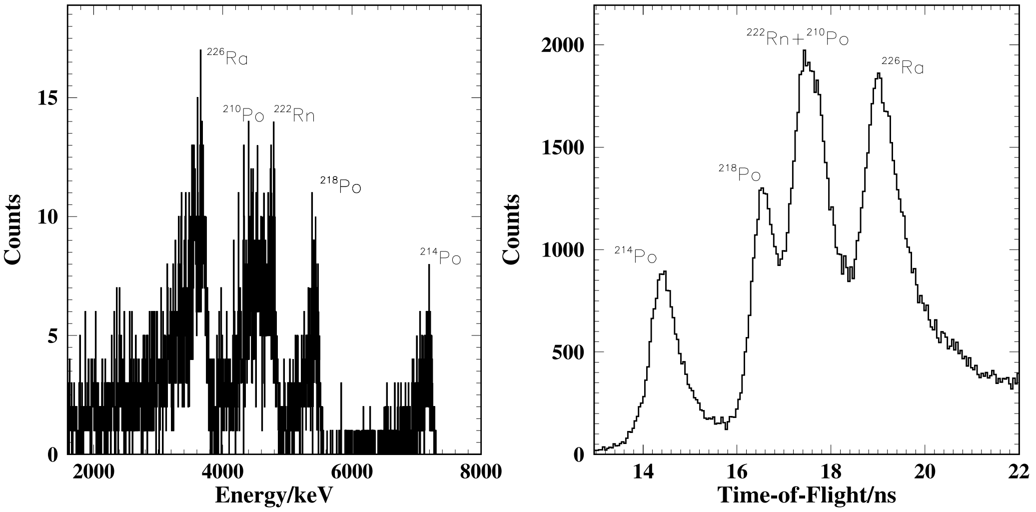

Figure 4.14: Accumulated coincident energy (left) and timing (right) spectra of the mixed α-source taken for a measuring period of 200 hours. The number of the counts in the energy spectrum (Si detector) is much less as compared to the statistics in the timing one. This is mainly due to the limited solid angle determined by the small active area of the silicon detector. The timing spectrum is obtained by taking the time difference between MCPI and MCPII signals which assuming identical MCP detectors, corresponds to a flight path equal to the distance between the two foils for SE production. The apparent timing resolution for this particular kind of experiment is found to be 330 ps (FWHM) per TOF detector.

In order to check the consistency of our results, a simulation of the α-particles TOF has been done using the SRIM code [Srim00]. A simulated timing spectrum compared with the measured one is represented in Fig. 4.15.

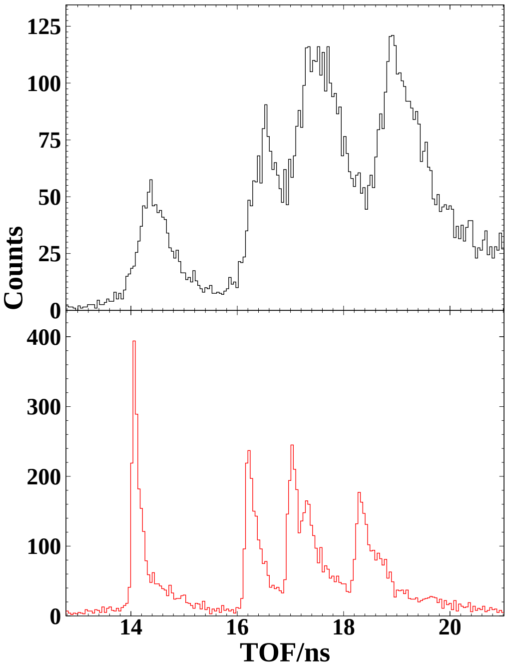

Figure 4.15: Comparison between a measured (black) and simulated (red) TOF spectra. To obtain the simulated timing spectrum, the energy spectrum from the Silicon detector, measured by putting the mixed α-source 3.5 cm directly in front of its surface is served as an input for the SRIM code. As a result, one becomes the theoretical energy distribution (energy loss, straggling and angular scattering are taken into account) of the α-particles after passing the first 300 μg/cm^2 PETP foil. This information, knowing the precise foil-to-foil distance and assuming zero-time detectors can be applied to derive an estimated TOF spectrum. Foil inhomogeneities are not considered.

The number of the experimental counts is normalised to the simulation ones. Since the simulation does not account for the detectors and electronics properties, as well as for the source energy spread, this could be an explanation for the slight deviation between the positions of the two spectra. It also indicates, that in order the system timing resolution to be improved, efforts towards better readout schemes should be made. One of them, as will be demonstrated in Chapter 5 is the incorporation of the CFD (model CFT-5388) module, discussed in Subsection 2.4.12.

Chapter 5

Measurements with heavy ion beams

In this chapter, we will focus on the experiments performed at the FZ Dresden-Rossendorf 5 MV tandem accelerator. The goal is to learn more about the response of the TOF detectors to various beams of heavy ions. We will show different detector combinations and measuring setups, answering important questions regarding the overall performance of the TOF spectrometer.

5.1 The FZ Dresden-Rossendorf tandem accelerator

The FZ Dresden-Rossendorf tandem accelerator is a vertical belt-driven 5-MV machine of the Russian EGP-10 type. Schematic drawing of the accelerator and the beam line is shown in Fig. 5.1. It is built by Efremov Institute NIIEFA, St.Petersburg (Russia) in 1972.

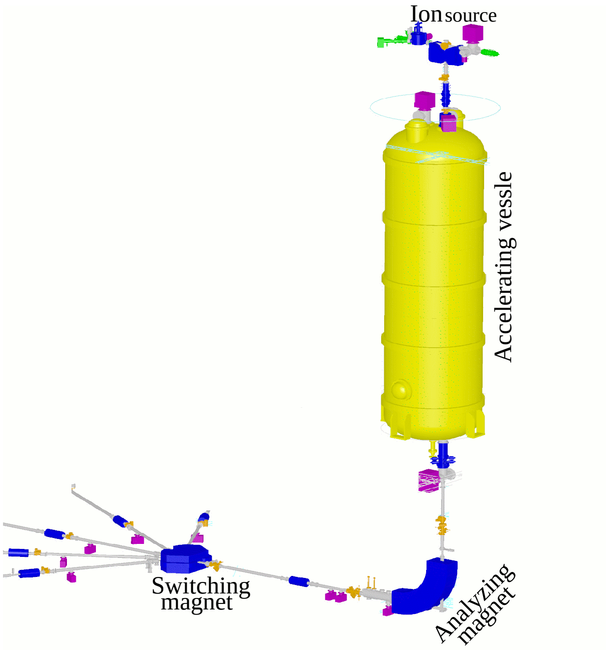

Figure 5.1: Vertical tandem accelerator of the EGP-10 type.

The accelerator is equipped with inclined-field accelerating tubes each of them 2200 mm long. A gas mixture of $CO_2 + N_2$ at pressure of 12-14 bar provides the high-voltage insulation for the accelerator column. Either CO_2 or argon gas are fed in the stripper canal. An electrostatic X-

steerer magnet behind the canal, and another XY-steer magnet after the accelerator are installed to compensate for the beam offset caused by the inclined electric field of the accelerating tubes. The terminal voltage is stabilised via a generating voltmeter (GVM) and Y-slits (with 1-mm high aperture) at the focus plane of the analyzing magnet. The post-acceleration beam transport and filtering is utilised through focusing the ions using an electrostatic quadrupole doublet and a 90° analyzing magnet with radius of curvature of 1.5 m, and $ME/q^2 = 240$ uMeV/e^2. Further momentum analysis is performed via a switching magnet with radius of curvature of 1.2 m, and $ME/q^2 = 77$ uMeV/e^2.
Some of the main accelerator parameters are summarised in the following:

- Terminal voltage: 0.8 - 4.5 MV
- Beam current: 0.001 - 10 μA
- Ion sources: Cs sputter ion source MISS-483, off-axis duoplasmatron EKTON-4
- Kinds of ions: ^{1}H, ^{2}H, ^{4}He, Li, ^{14}N, ^{15}N, O, Cl, Br and others

Since the device is located on the sight of Institute of Ion Beam Physics and Material Research, its current main fields of application are: Elastic Recoil Detection Analysis (ERDA), Rutherford backscattering spectroscopy (RBS), energy loss measurements, implantation beam line, detector development and others.

5.2 First in-beam MCP detector test measurements

A measuring setup as depicted in Fig. 5.2 has been installed at the beam line of the 5 MV FZ Dresden-Rossendorf tandem accelerator [Kose05a].

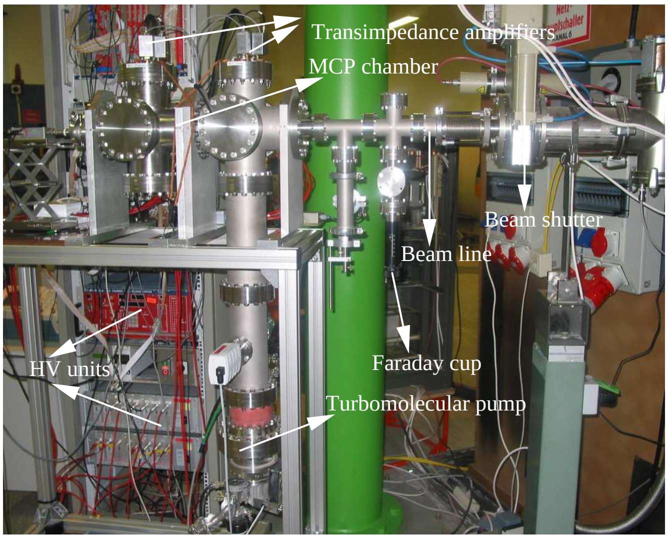

Figure 5.2: The experimental chamber containing the multichannel plates is positioned on a variable height metal stand. A hand driven Faraday cup is inserted inside the beam line before each measurement. To preserve the detectors intact, requirement for beam currents of much less than 1 pA has to be met. The achieved vacuum is better than 4.5×10^{-8} mbar. The excellent vacuum conditions guarantee stable and longterm detector operation.

The experimental device consists of two identical MCPs with foils, accelerating grids and electrostatic mirror. Its principle of operation and readout electronics were discussed in detail in Section 4.5. A 40 MeV ^{35}Cl beam passes through an aperture of 500 μm such that the beam current could be reduced to much less than 1 pA. The ion particles knock SEs out from the metallised thin foils which after acceleration by an electrostatic field of more than 7 kV/cm are deflected at 90° by the electrostatic mirrors before they produce signals in the MCP stacks. The experimental assembly is depicted in Fig. 5.3. For beam monitoring purposes, two silicon detectors - in front and behind the TOF setup are used. That enables us to probe the beam quality. The first beam monitor silicon detector is manually driven in and out of the beam line while the second one remains fixed.

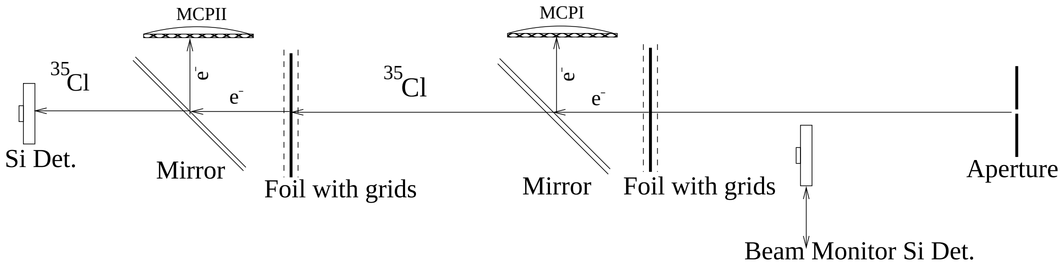

Figure 5.3: Experimental setup. The heavy ion beam comes from the right. For time reference which enables us to obtain a TOF spectrum between the two foils positioned at a distance of 27 cm, signals from the rear sides of the MCP stacks in coincidence are taken.

Two spectra - energy and TOF are presented in Fig. 5.4 and Fig. 5.5.

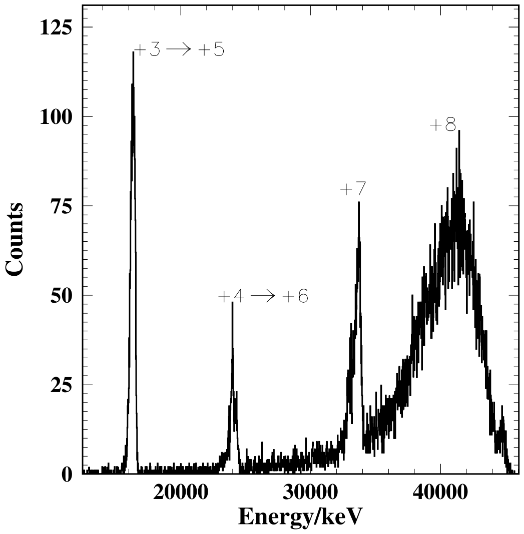

Figure 5.4: Energy spectrum of a cocktail ^{35}Cl beam measured with a 60 μm silicon detector, positioned in front of the beam aperture. The observed energy peaks correspond to different ion charge states. The arrows depict charge exchange processes inside the accelerator. The requirement for extremely low beam currents, causes sometimes beam instabilities (deviations of the accelerator terminal voltage with time). This may occasionally result in beam energy spreads of more than 10% (FWHM).

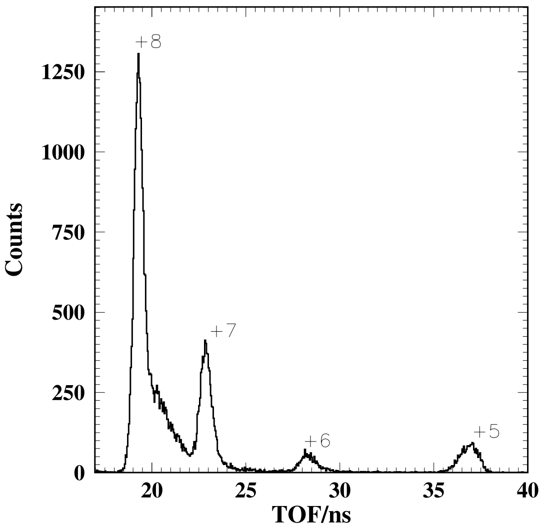

Figure 5.5: Obtained TOF spectrum between the 2 MCP detectors. To ensure equal electron transient times inside the two electrostatic mirrors, their parts (mirror front, mirror back and grids) are set at exactly the same high voltage potentials.

To prove that the measured TOF spectrum is consistent, a simulated TOF spectrum has been compared to the measured one as represented in Fig. 5.6.

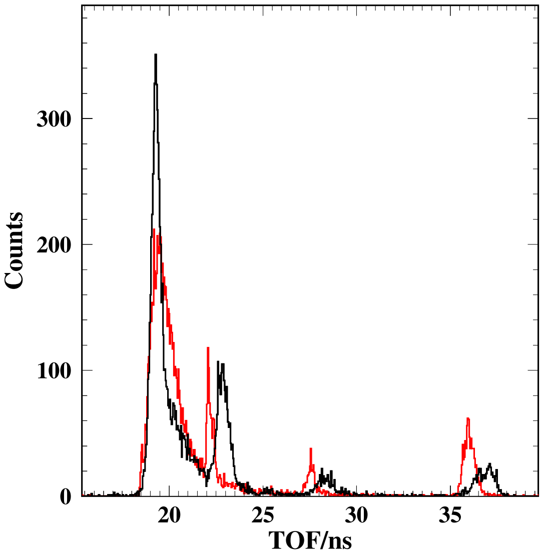

Figure 5.6: Measured (black) and simulated (red) spectra. The simulated spectrum is obtained by supplying the energy information from the silicon beam monitor detector as an input for the SRIM code. As a result, one becomes the energy distribution after the first PETP foil by taking into account the beam straggling and angular distribution inside the foil. This can then be easily converted to TOF spectrum. The simulation is done under the assumption that our MCPs have infinite time resolution and the SE foils are perfectly homogeneous which explains the slight position discrepancy between the two spectra.

5.3 Multichannel-plate pulse height distribution and the foil electron yield

In Chapter 2, we mentioned that it is most favourable to operate the MCP detectors in the so-called “Chevron” configuration. This allows us to obtain high gains of secondary electrons in the order of 10^8, simultaneously achieving peaked pulse height distributions with a quasi-Gaussian shape. The quoted value for the FWHM of such distributions is around 50 % [Wiza79].
The 5 MV FZ Dresden-Rossendorf tandem accelerator provides the necessary conditions to investigate the above mentioned effect with a test setup shown in Fig. 5.7.

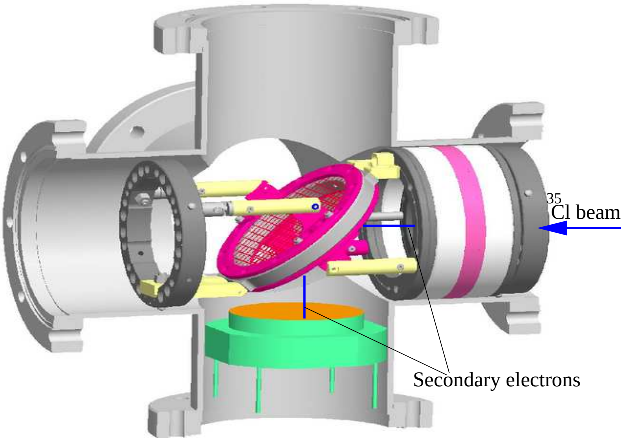

Figure 5.7: Experimental setup. The heavy ion 30 MeV ^{35}Cl beam beam ejects SEs from the PETP foil. These generate signals in the MCP detector. For the purpose of energy detection, one of the MCP signal outputs is directly fed into a charge-sensitive preamplifier.

The readout scheme is presented in Fig. 5.8. Shortly, the MCP front signals are used for DAQ trigger, whereas the signals from MCP rear side are applied for energy spectra collection. The pulse height spectrum is retrieved by a CAEN V555 VME ADC, accepting gates from an ORTEC GG8010 Gate-and-Delay module after each DAQ trigger.

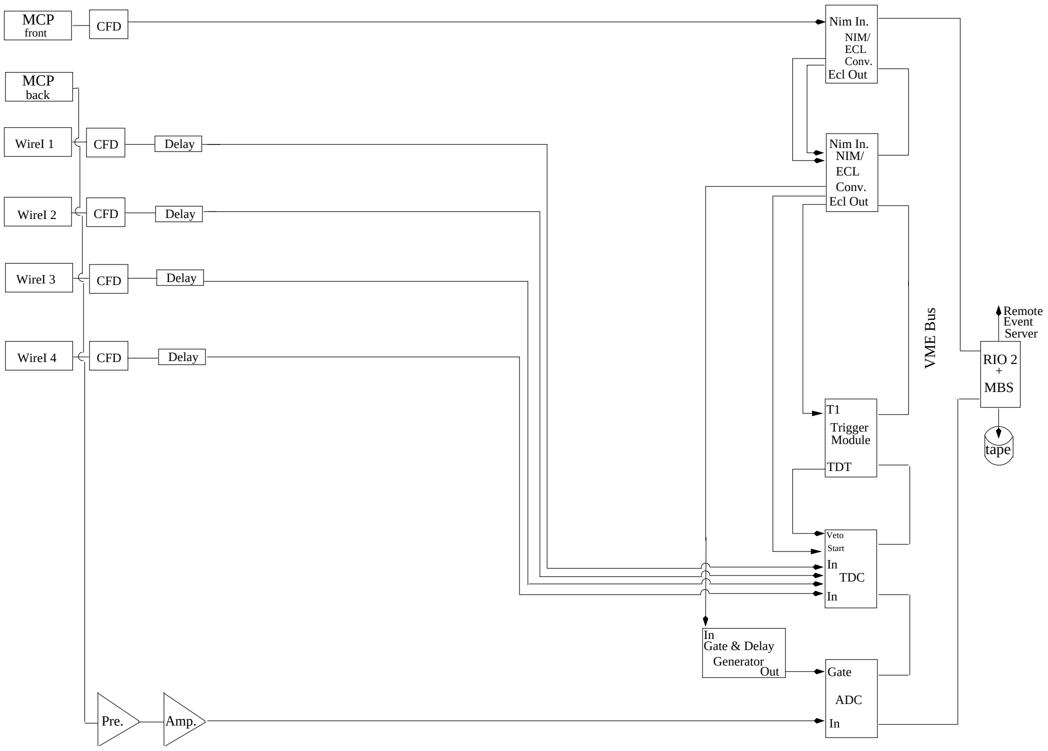

Figure 5.8: Readout scheme.

Two example spectra are shown in Fig. 5.9. The left one corresponds to a MCP pulse height distribution without beam (background measurements). The right one is obtained under beam conditions.

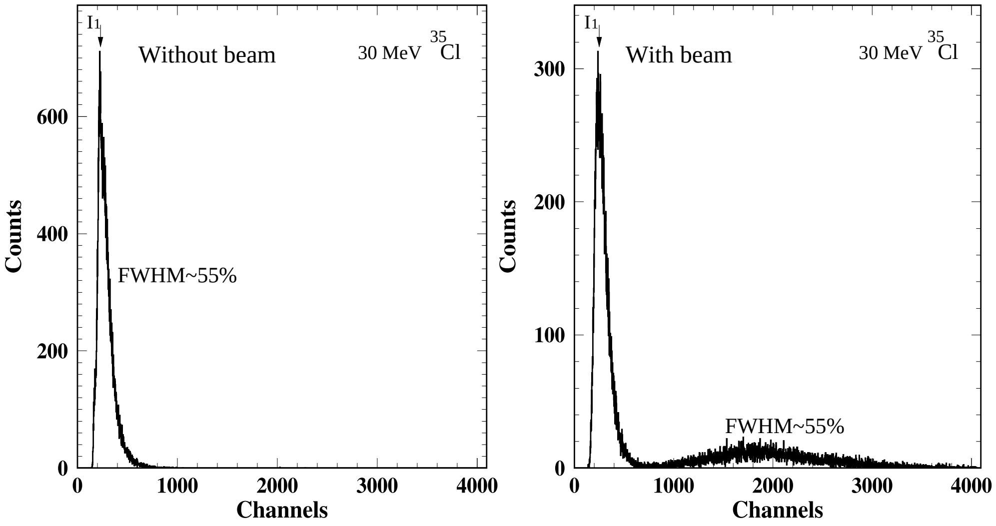

Figure 5.9: Pulse height distributions.

The difference between the two spectra is clear to see. Additional bump structure appears to the right when the beam is switched on. The pulse height distributions for the both measuring cases have FWHM around 55 %. This well matches the values reported in literature.
The distribution measured with the ^{35}Cl beam, reflects not only the probability for a single electron detection (signals caused by thermal excitations of electron inside the channel plates, random electrons possibly coming from the highly biased mirror parts and other sources of noise) which corresponds to the sharp narrow peak in the observed spectra, but also the contribution of the bunch of electrons being simultaneously ejected from the foil surface as the beam passes through (right bump structure). In other words, the pulse height of the MCP signal is proportional to the number of SEs detected. While α-particles are capable of producing much less than 10 electrons in the 2π hemisphere, a fission fragment causes the generation of a hundred and even more electrons when interacting with a thin foil [Cler73]. It is also well known that the SEs emission is strongly dependent on the nuclear charge Z of the impinging projectiles.
From the beam spectrum, one can try to deduce the secondary-electron yield g (the mean number of secondary electrons in beam direction produced by a single Cl ion) using the equation:

$$g = \langle I \rangle / (\varepsilon \eta I_1), \tag{5.1}$$

where $\langle I \rangle$ is the mean value of the pulse height distribution, I_1 the pulse height for a single electron detection, ε the efficiency of the MCP ($\approx$0.6 [Gala71]) and η the foil detection efficiency. We will show in the following sections that the foil detection efficiency reaches up to more than 90% for ions like Cl. Similar method with MCPs for obtaining electron yields is discussed in the work of K. Kimura [Kimu00].
Applying the above formalism, the derived number for the forward emitted SEs is $\gamma\approx$14 - 16. The order of magnitude of this value matches the results quoted in [Cler73], where experiments with fifty times thinner foils and surface barrier detectors have been performed.

5.4 Multichannel-plate timing with Si detectors

Here, we will present a timing setup consisting of a single mirror MCP and a Si detector.
Parameters like channel length to diameter ratio - α, pore size, active area, signal decoupling and others as discussed in Chapter 2, determine the multichannel-plate detectors timing properties. Since the silicon detectors are semiconductor devices, the factors influencing their timing capabilities are somewhat different. Among these with a predominant role is the charge collection time - T_R. It affects strongly the rise time of the collected pulses. Although a precise calculation of T_R is quite complex, an approximation formula for easily obtaining T_R for silicon detectors at room temperature is:

$$T_R \simeq W \times 10^{-7} s, \tag{5.2}$$

where W is the thickness of the depletion region measured in mm [Orte98].
A very simple relation - $W \sim \sqrt{U}$ [Knol89], where U is the applied reverse voltage, shows that the depletion depth is strongly correlated to the detector bias. Furthermore, for a planar geometry, the capacitance of the silicon detector can be expressed as:

$$C = \varepsilon \frac{A}{W}, \tag{5.3}$$

where ε has the meaning of a dielectric constant and A is the area of the depletion zone. As demonstrated in Fig. 5.10, the detector capacitance plays an important role for its timing resolution.

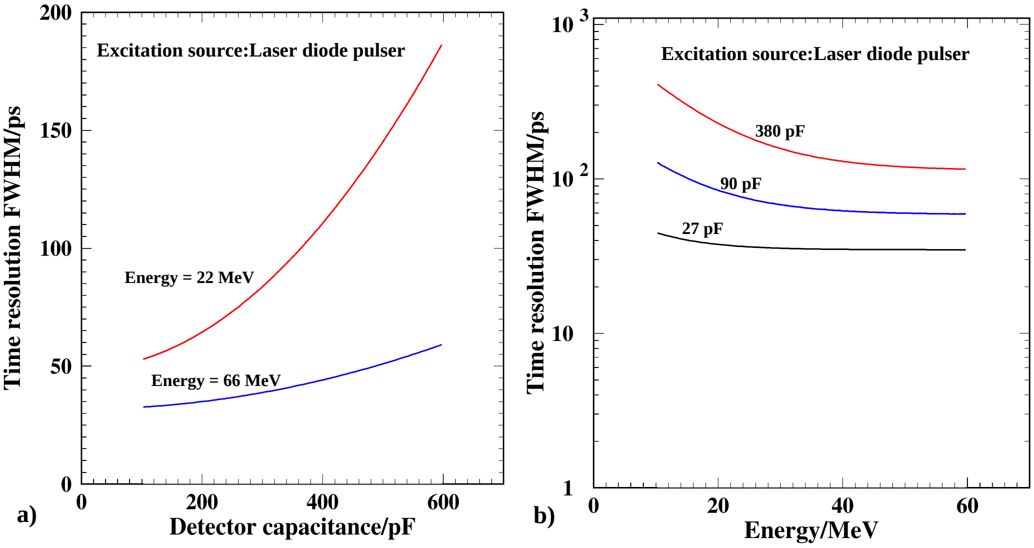

Figure 5.10: Change of the timing properties of silicon detectors in respect to their capacitance (a) or the detectable energy (b) after [Orte98]. The timing measurements are performed relative to a calibrated laser diode pulser. One sees, that lower capacitance and higher energy values result in improved resolutions.

An example voltage-capacitance characteristic curve for an ORTEC (type CA-24-1000-100) Si detector is presented in Fig. 5.11.

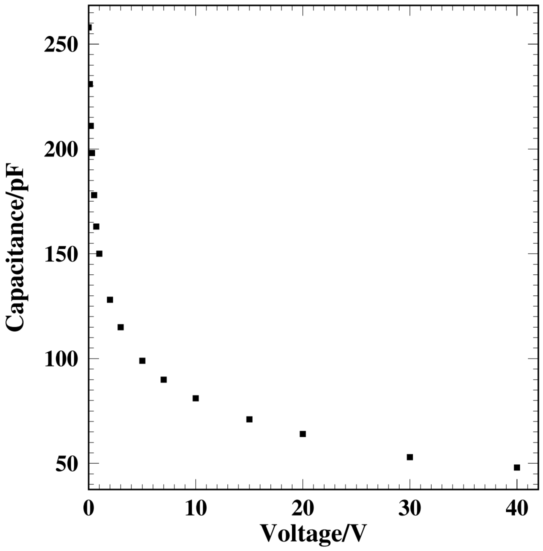

Figure 5.11: Measured voltage-capacitance characteristic curve for an ORTEC (type CA-24-1000-100) Si detector with 100 kHz high voltage generator. At bias values larger than 20 V, the capacitance drops to less than 70 pF. The uncertainty of the experimental points is 0.05 %. The detector bias is applied under air.

Because the derived signal from the silicon detector is fast and small, a fast amplifier must be employed if an ultimate timing resolution has to be achieved. For the purpose of our measurements we incorporate 2 GHz SHF 88 Wideband Amplifier[1]. The device has risetime

---

[1] SHF design, Bruchsaler Str. 15, 1000 Berlin 31, Germany

capabilities of better than 220 ps and a gain of 40. Its wide bandwidth and low noise features are due to specially selected microwave transistors. SHF 88 has a four stage bipolar amplifier design with each stage tuned for minimal ripple and a low input return loss. It is mainly applicable in the areas of optical and satellite communications, data transmission and antenna measurements.

In order to test the timing properties of a Silicon detector (type CA-24-1000-100) versus a single TOF mirror MCP detector, a readout scheme as described in Fig. 5.12 has been implemented.

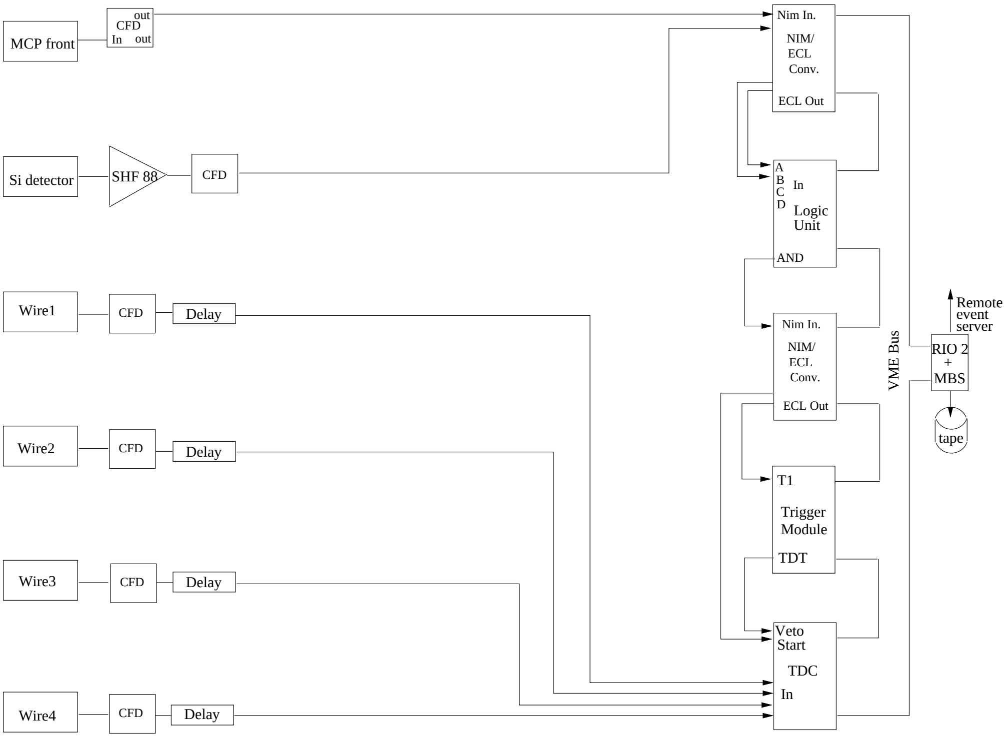

Figure 5.12: The readout scheme. The logic signals from the Si and the MCP detectors are fed into a V512 VME logic module which initiates DAQ trigger if they come in coincidence. The time sequence of the incoming signals is recorded by V775 TDC VME module.

A resulting timing spectrum taken with 30 MeV ^{35}Cl beam is shown in Fig. 5.13.

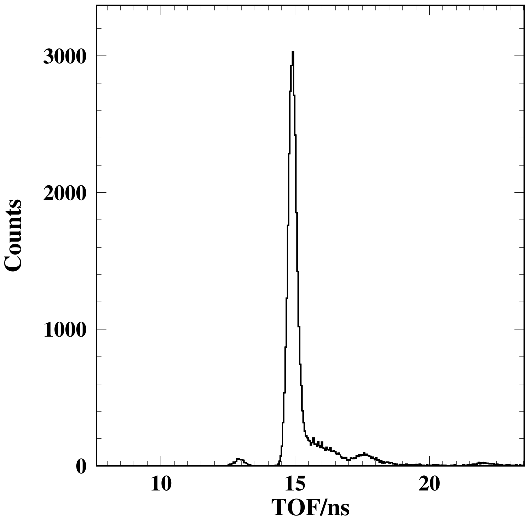

Figure 5.13: Obtained TOF spectrum between a single TOF and a Si detector for a 30 MeV ^{35}Cl beam. The resulting FWHM is in the order of 360 ps.

Similar TOF setup is discussed in the work of Vockenhuber [Chri05] *et al.*, where the quoted resolution (FWHM) between a Si and MCP mirror detector is in the order of 700 ps.

5.5 Timing setup with anode readout multichannel-plate detector

In this Section, we will discuss a setup comprised of a single mirror MCP detector and MCP with anode decoupled timing signals. The detector and its biasing scheme are overviewed in detail in Section 2.3. Among the presented measurements, we derive values for the transient times of the electrons in the mirror. Such an estimate is of importance for the TOF spectrometer. A measuring setup as shown in Fig. 5.14 has been arranged. The 40 MeV ^{35}Cl beam enters from the right. The mirror MCP is operated in "backward" mode. Electrons ejected from the SE foil are deflected by the electrostatic mirror and produce signals in the the first MCP, whereas the beam particles hit directly the small MCP detector with decoupled from a massive copper anode signals.

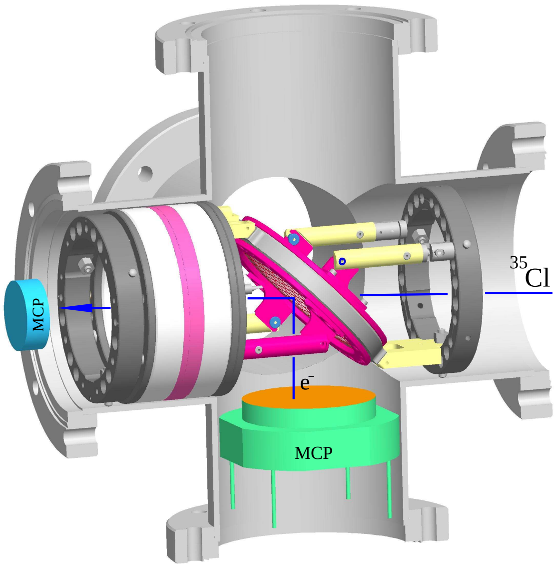

Figure 5.14: The experimental setup. The heavy ion beam comes from the right and impinges directly on the small (blue color) with diameter of 25 mm MCP, operated in Chevron mode. The detector is displayed in Fig. 2.9 and its biasing scheme is depicted in Fig. 2.10 (Section 2.3). The distance between the SE foil and the small MCP is around 6 cm. The signals from that detector are directly derived from a flat copper anode and fed into a CFD module. In such a way, it is operated in coincidence with the signals from the mirror MCP detector.

At bias voltage of +2.7 kV, the amplification in the small MCP directly hit by the 40 MeV ^{35}Cl beam becomes so large, that the obtained signals reach amplitudes of more than 5 V, which is above that what a conventional PMT usually delivers. This effect is shown in Fig. 5.15. For comparison, α-particles at the same biasing voltages and with energies between 4 and 6 MeV are capable of inducing signals of not more than 400 mV . Although the biasing scheme allows for applying voltages of up to 2.9 - 3 kV, we have never reached these values under in-beam conditions, since this could be a potential damaging risk for the particular detector and its readout electronics.

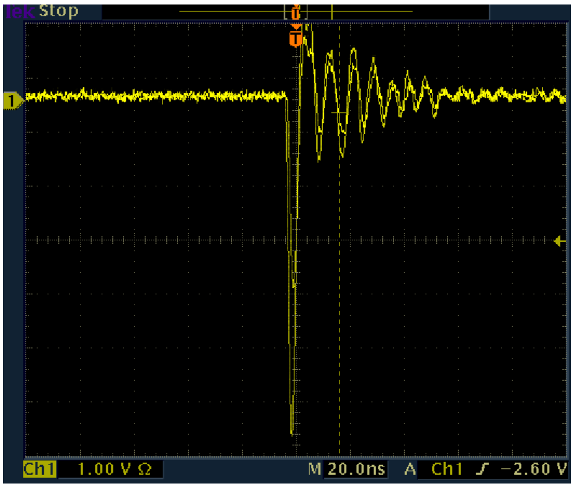

Figure 5.15: Oscillograph picture of the MCP anode signal taken with 40 MeV ^{35}Cl beam and bias voltage of +2.7 kV. The signal amplitude reaches more than 5 V.

In Fig. 5.16 a) and b), two example TOF spectra between the small and the mirror MCP for different biasing voltages applied at the small multichannel-plate are presented. An interesting effect is observed - at relatively low bias voltages, the TOF spectrum clearly registers the different beam components - Fig. 5.16 a). At higher potentials, however, a strong electron peak on the left side of the TOF spectrum emerges - Fig. 5.16 b).

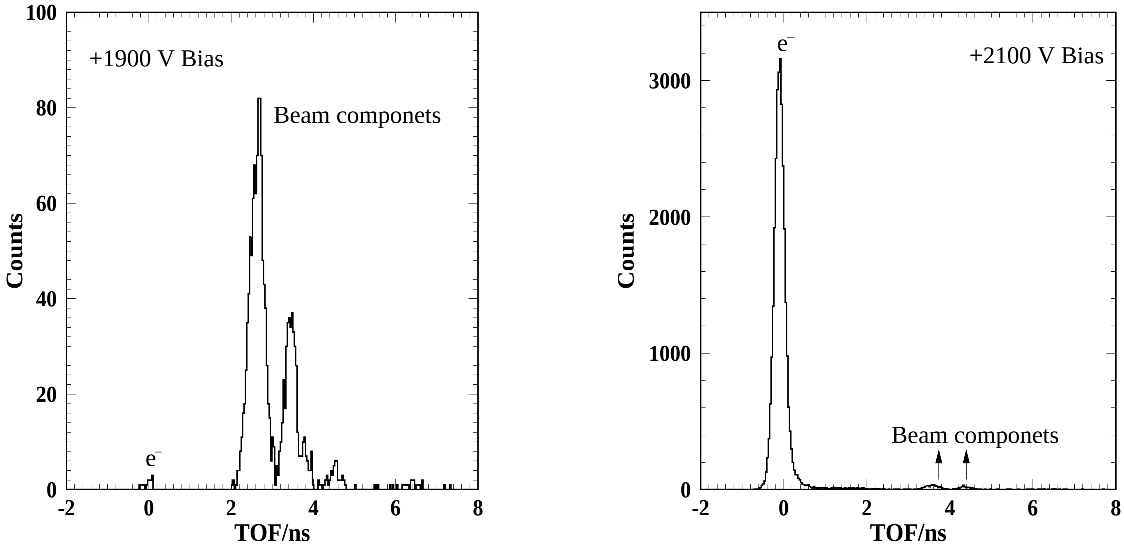

a)

b)

Figure 5.16: Observed TOF spectra between the two detectors at low a) and higher b) MCP small bias potentials.

When a ^{35}Cl ion penetrates the SE foil, a number of electrons are being liberated. These electrons are swept away by the strong electrostatic field applied between the foil and the grids.

At low bias voltages, the small MCP detects them quite inefficiently, whereas the heavy ions capable of ejecting more electrons from the MCP channel walls, generate detectable signals with a higher probability. As the MCP bias voltage goes up, the electron detection efficiency increases. The electrons which are faster and greater in number than the Cl ions reach the small MCP first and create signals in it. This results in a prominent electron peak in the TOF spectrum while the beam component is strongly suppressed - Fig. 5.16 b).

The effect of the small MCP bias voltage on the achieved timing resolution is also investigated. That is done for the case when the SE electrons are accelerated to more than 4 kV. The result is demonstrated in Fig. 5.17 a). At higher operating voltages, the number of the collected electrons n_e at the output of the chevron stack increases. This eventually enhances the timing properties of the detector in agreement with the expectation that the time resolution should be proportional to $\sqrt{n_e}$ [Wiza79].

We showed, that practically at operating voltages higher than +2100 V, only the electrons ejected from the SE foil are efficiently registered in our TOF spectrum. In this respect, it would be interesting to know what is the impact of the foil accelerating voltage on the system time resolution at fixed MCP small (+2700 V) and MCP mirror (+2900 V) bias potentials. This is shown in Fig. 5.17 b). Basically, increasing the accelerating voltage, increases the energy of the electrons falling on the MCP surface and consequently the yield of the electrons n_e coming out of the MCP channels. That causes improved timing signals and better resolution results.

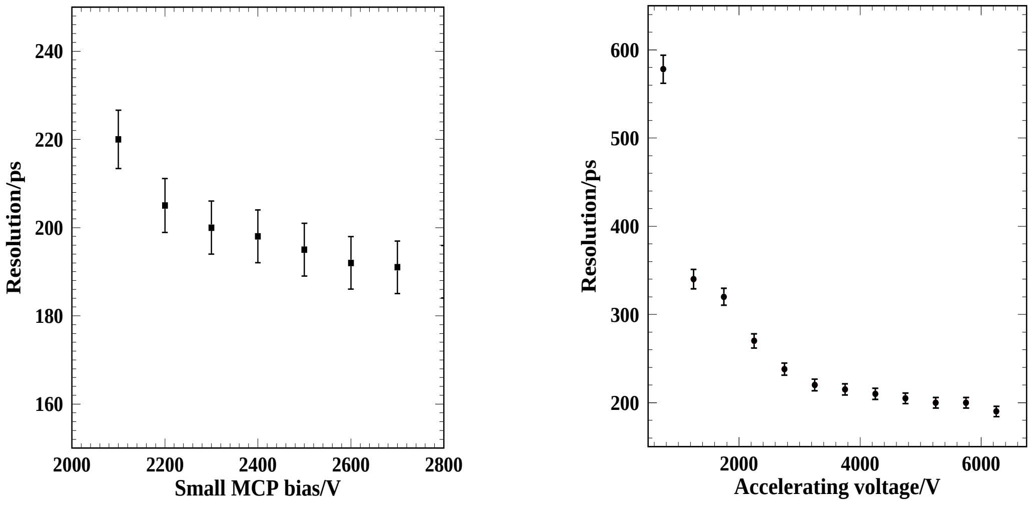

a)

b)

Figure 5.17: Effects on the observed resolutions (FWHM) in the TOF spectra depending on the small MCP bias a) and the foil accelerating voltage b). In the first case, the measurements are taken at fixed foil potential, while during the second one, the foil voltage is varied at constant bias of the MCPs. Best resolution values (~190 ps) as expected are achieved with the greatest bias and accelerating potentials applied. Unfortunately, they could not be set arbitrary high, since at some point this would cause overall system instabilities (sparks, sudden vacuum deterioration and consequent possible malfunctioning of the electronics modules).

When a Cl ion interacts with the SE foil, electrons are liberated in both forward and backward directions. These electrons are repelled by the high negative field at the very foil and attracted by the equally positively biased foil grids. This means, that a certain time must elapse, before a given electron after deflection by the electrostatic mirror reaches the MCP and produces a signal. If we know the distance between the foil and the small MCP together with the approximate flight path which the electron travels inside the mirror, the TOF spectra can theoretically serve as an estimate for the electron mirror transient times. Such a result is presented in Fig. 5.18.

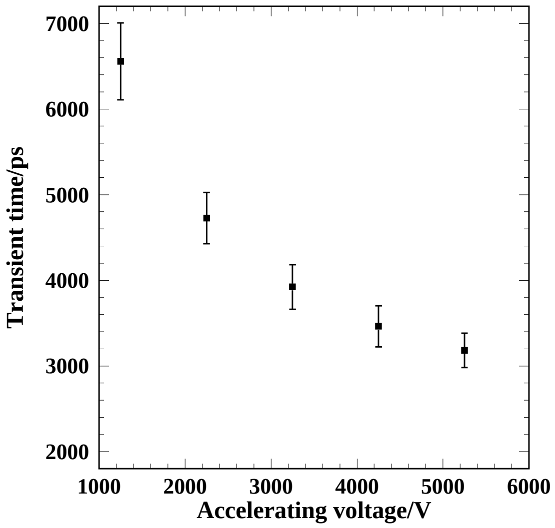

Figure 5.18: Electron transient times as a function of the foil accelerating voltage. The cable signal propagation times are equal for the two detector branches. From the picture is seen that the transient times in the mirror are in the order of several nanoseconds.

5.6 Arrangements for optimal Time-of-Flight resolution

The quality of the timing information derived from the mirror MCPs is crucial. In Subsection 2.4.11, we described the development of a transimpedance amplifier for multichannel-plate detectors. The properties of a new state of the art CFD module (type CFT-5388) based on the ARC technique with very low threshold (2 mV - 3.5 V) capabilities have been discussed in Subsection 2.4.12. These devices have been implemented for the first time in our measuring setup shown in Fig. 5.19 at the beam line of the 5 MV FZ Dresden-Rossendorf tandem accelerator [Kose06].

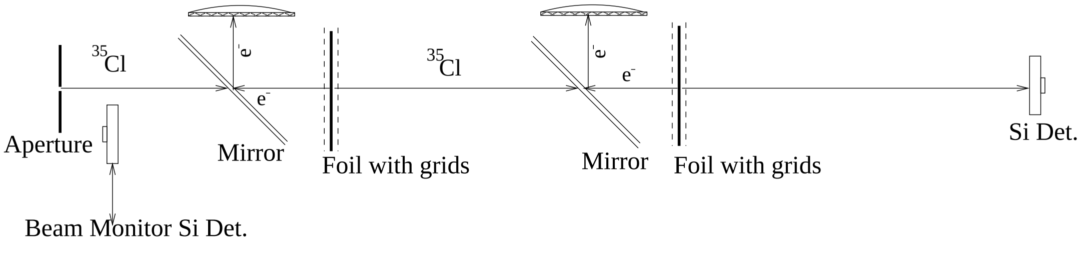

Figure 5.19: The experimental setup.

The heavy ion beam comes from the right. The two mirror MCP detectors are operated in "backward" mode. For time reference enabling us to obtain a TOF spectrum between the two foils positioned at a distance of 27 cm, signals from the rear sides of the MCP stacks processed by the transimpedance amplifiers and directly fed in the CFT-5388 CFDs in coincidence are taken. The readout scheme is the same as overlayed in Section 4.5. For beam monitoring purposes, two Si detectors - in front of the beam aperture and after the second SE foil are positioned. The operating point of the transimpedance amplifiers is adjusted in-beam conditions, and the CFD thresholds are set just above the noise level. An example TOF spectrum is given in Fig. 5.20.

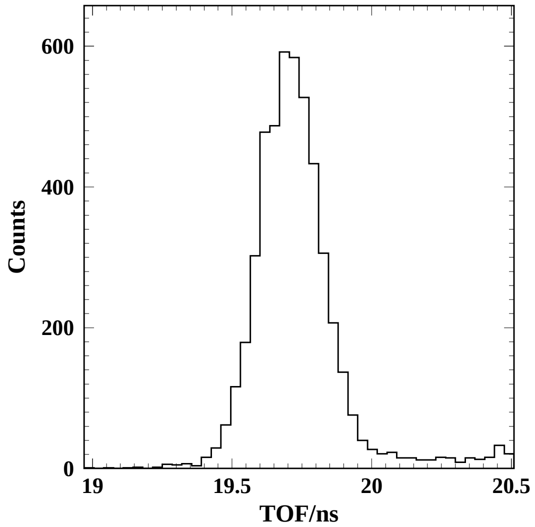

Figure 5.20: TOF spectrum between the two MCPs for a 40 MeV ^{35}Cl beam taken with transimpedance amplifiers and CFT-5388 CFDs. The foi-to-foil distance is 27 cm. The obtained FWHM results in 240 ps [Kose06, Kose07]. Assuming identical detectors, the apparent time resolution of one detector corresponds to 170 ps. It has to be mentioned that the beam quality can also affect the observed timing resolutions.

Another aspect of importance is the impact of the foil accelerating voltage on the timing resolution. Results regarding this problem are presented in Fig. 5.21.

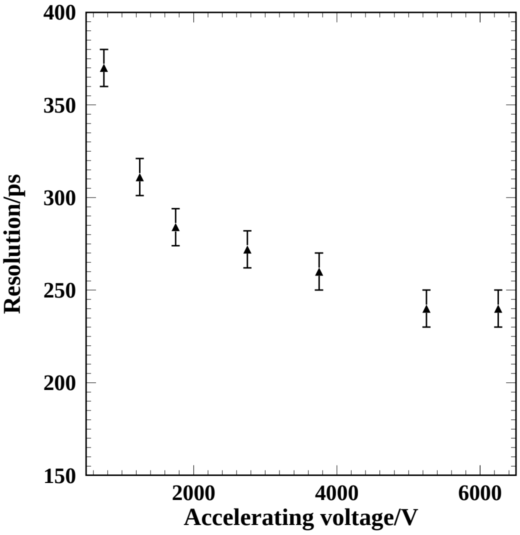

Figure 5.21: Achieved TOF resolutions (FWHM) as a function of the applied foil accelerating potentials. The mirror back side of the two mirror detectors is set at -2.7 kV. At lower accelerating voltages, most of the liberated from the foil electrons are not properly collected by the electrostatic field and simply diffuse without reaching the MCP surface. This causes signal worsening and poorer resolution results.

If $M = 2Et^2/l^2$, where M is the mass of a given particle, E denotes its energy, t the flight time and l the TOF distance, then the following relation for the mass resolving power of a single arm spectrometer with an energy detector holds:

$$(\frac{\Delta M}{M})^2 = (\frac{\Delta E}{E})^2 + (\frac{2\Delta t}{t})^2. \tag{5.4}$$

With a current time resolving power of $t/\Delta t$ of more than 70 for a flight path of 0.3 m, the separation of single (light) fission fragments with a mass resolving power of $M/\Delta M$ in the order of 40 with an energy resolution of the silicon detector of about 0.35 % should be possible.

5.7 Efficiency measurements with ion beams

As already pointed out in Section 4.3, one of the important characteristics of the mirror TOF detector is its detection efficiency. Generally, it reflects the probability a certain particle to be recorded by the MCP when passing through the SE foils. Efficiency measurements with α-particle source with energies ranging from 4.72 up to 7.88 MeV have been presented in Section 4.3. Since the number of the emitted from the foil electrons in both forward and backward directions is a function of the projectiles nuclear charge, it is expected that the heavier particles would yield more SEs. In a real photo-fission experiments the Z of the fissile elements is usually greater than 40 with energies one order of magnitude higher than that of an ordinary α-particle source.
To probe the efficiency of the mirror detector, we use a combination of different ions and energies delivered by the 5 MV FZD tandem accelerator. Efficiency measurements for forward and backward emitted from 300 μg/cm^2 PETP foil SEs have been performed. The experimental method is similar to the one described in Section 4.3. Results for ^{12}C and ^{35}Cl beams are presented in Fig. 5.22.

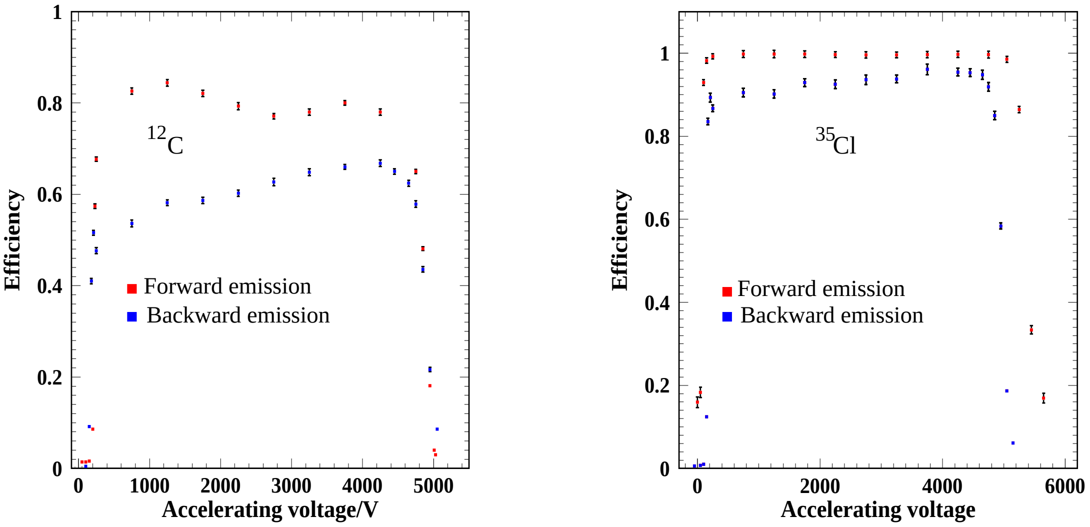

Figure 5.22: Efficiency measurements with ^{12}C and ^{35}Cl beams.

Results for efficiency measurements taken with ^{79}Br and ^{127}I beams are given in Fig. 5.23.

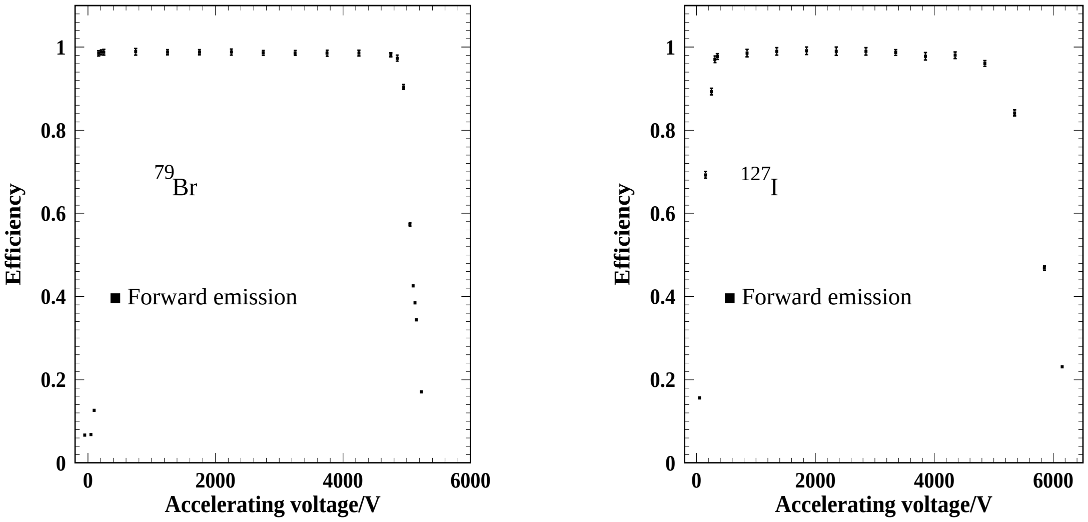

Figure 5.23: Efficiency measurements with ^{79}Br and ^{127}I beams.

The mirror back part is set at about -2.7 kV. The ^{12}C measurements are performed at beam energies of 24 MeV, whereas all the other projectiles - ^{35}Cl, ^{79}Br, ^{127}I have energies of 40 MeV. As one can see, stable detection efficiency has been obtained at an accelerating potentials of approximately 1000 V. This agrees well with results from the literature [Eras85, Krug99]. For ions with $Z > 30$, it could be concluded that the system detection efficiency is better than 90 %. The ratio between the forward and backward efficiency values for ^{35}Cl case reaches unity. Unfortunately, complete (backward efficiency) measurements for the ^{79}Br and ^{127}I cases have not been performed, since with ions of this type, the tandem machine often fails to deliver stable, reasonably low (less than 0.1 pA) currents over a certain period of time. Nevertheless, we suppose that the results would resemble those taken with ^{35}Cl beam.

At small accelerating potentials the spread of the SEs is large. They are not properly collected by the electric field and simply diffuse without being detected by the MCPs. This is basically the reason for the left slope of the efficiency curves in Fig. 5.22 and 5.23. Such mode of operation is of course not desired.

With increasing the accelerating voltage, the initial transversal energy spread gets fully compensated [Nank05] and at some point the efficiency does not change any more. One can show (see Eqs. (2.4) and (2.5)) that an 45°-tilted electrostatic mirror will reflect the SEs only if the following condition is satisfied [Nank05]:

$$\frac{\Delta V}{\Delta V_f} \geq 0.5, \tag{5.5}$$

where ΔV_f is the foil acceleration potential and ΔV denotes the mirror deflection potential. At higher accelerating voltages ΔV_f, the mirror will become transparent. Indeed, such effects is experimentally observed in a good agreement with Eq. (5.5). At high accelerating potentials, most of the SEs gain enough sufficient kinetic energy to pass through the electrostatic mirror without being deflected towards the MCP surface. This is what we call “mirror transparent” mode of operation, reflected in the right slope of the efficiency curves. Such regime of exploiting the setup is also not favourable because the probability to detect a particular event becomes relatively low. For optimal operation, voltages in the saturated (plato) area should be preferably applied.

5.8 Energy distribution spread of the secondary electrons ejected by ions from foils

As already demonstrated, the SEs ejected from the PETP play a major role in the detection of the fast heavy ions. The SEs emitted from the foil are used for a timing signal to measure the ions time-of-flight. The energy distribution and yield of SEs is a function of projectile's nuclear charge, velocity and the target material [Pfer77]. The SEs foil transport mechanism is quite complex and is theoretically as well as experimentally treated in various works [Riva03, Lanz03, Pfer77].
We have shown, that at higher accelerating potentials the electrostatic mirror becomes transparent for the SEs. The mirror transparent properties carry also another meaning. Because the efficiency drop follows stepless slope, this implies that the phenomenon reflects the SE energy distribution [Nank05]. Since the efficiency as a function of the accelerating voltage has an error function behaviour, it is expected that its standard deviation contains the standard deviation of the SEs energy distribution. Results representing the widths of the SEs' energy distribution for ions with different atomic numbers are displayed in Fig. 5.24.

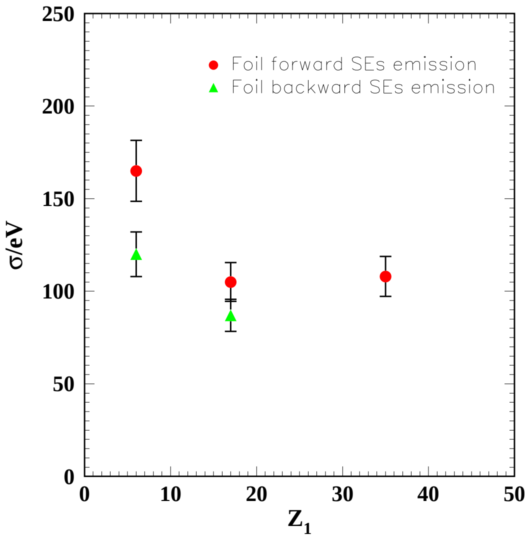

Figure 5.24: Picture partially adopted from [Nank05] showing the widths of the SEs' energy distribution for ions with different atomic numbers (Z_1) and different types of electron emission (forward and backward).

5.9 Reconstructing the secondary electron velocity distribution by means of the Time-of-Flight method

Another experimental setup for SEs' velocity and energy determination has been established as overlayed in Fig. 5.25 [Kose05b]. The ion beam knocks out electrons from the first foil in backward and forward direction. After deflection at 90° by the electrostatic mirror, the backward electrons produce a valid start signal for the DAQ system. The stop signal is generated by the forward emitted electrons, accelerated by the grid and finally deflected by the second electrostatic mirror towards the second MCP detector.

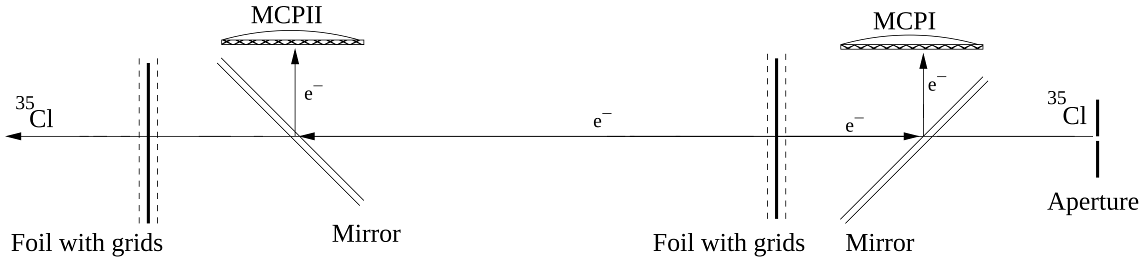

Figure 5.25: The experimental setup. The 40 MeV ^{35}Cl beam enters from the right. It is let through a cylindrical aperture with a diameter of 500 μm. The backward emitted from the first foil electrons generate signals in the first MCP, while the forward ones after travelling a distance of approximately 20 cm are reflected towards the second MCP.

For time reference which enables us to obtain the SEs TOF and convert it to velocity (see Fig. 5.26), signals from the back side of the MCP detectors are taken. The sequence of the signal arrival times is processed by CAEN V775 TDC module and recorded by MBS DAQ. The electric potentials are chosen in such a way as to ensure a field free drift region for the forward emitted from the first foil SEs, and second to prevent backward emitted from the second foil SEs to reach the adjacent MCP detector. Because the SEs are accelerated by electrostatic fields of more than 6500 V/cm, the deviation of their flight path from the optical axes of the spectrometer can be neglected. The SEs velocity distribution is taken to be the ratio of the geometrical flight path and the measured TOF adjusted for the transient time of the backward emitted electrons. Additionally, the time delay of the connecting cables is chosen to be equal for the two MCP branches. The velocity distribution of SEs has been extrapolated to zero accelerating voltage.

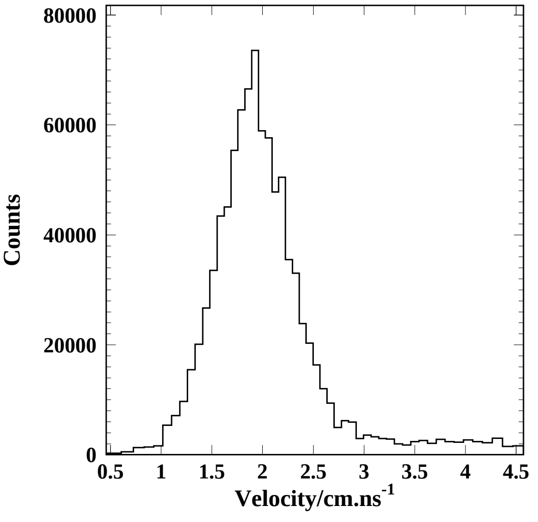

Figure 5.26: Velocity spectrum of secondary electrons ejected by 40 MeV ^{35}Cl beam [Kose05b]. The resulting mean SEs velocity closely approaches the one of the beam ions. Similar effect discussed in the work of G. Lanzanó [Lanz03] *et al.* is attributed to the so-called “convoy” electrons.

The recalculation of the SEs' velocity spectrum in energy distribution is shown in Fig. 5.27.

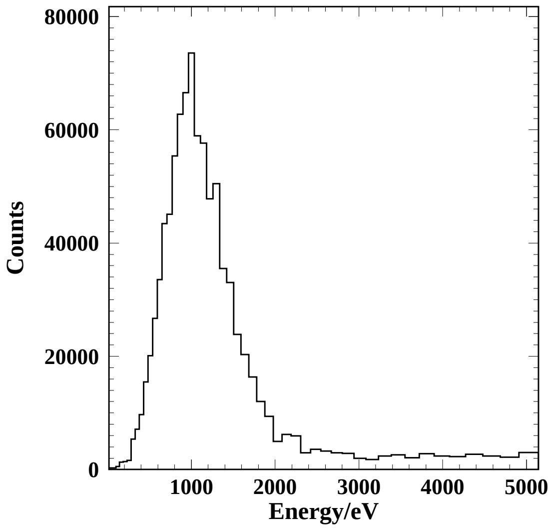

Figure 5.27: Energy spectrum of the SEs. The peak is centered at around 900 eV with sigma of approximately 300 eV [Kose05b]. We estimate that the reported value could be 15-20% less due to uncertainties of the electron flight paths. Since the backward emitted electrons generate the start and the forward emitted ones the stop signal, both forward and backward SEs' energy distributions enter in the same spread. Such a method of retrieving the spread of the secondary electrons gives similar results to the one reported in the previous section.

5.10 Position resolution with ion beams

Until now, we have discussed the sensitivity of system parameters like time resolution and efficiency, depending on the applied accelerating voltage. Position resolution measurements with α-source and their overall importance for the TOF spectrometer were outlined in Section 4.4. Here, we will shortly demonstrate the impact of different ion beams (^{35}Cl, ^{79}Br, ^{107}Ag) on the quality of the position information derived from the MCP delay-line anode, related to the foil bias and the type of electron emission. Results are presented in Fig. 5.28.

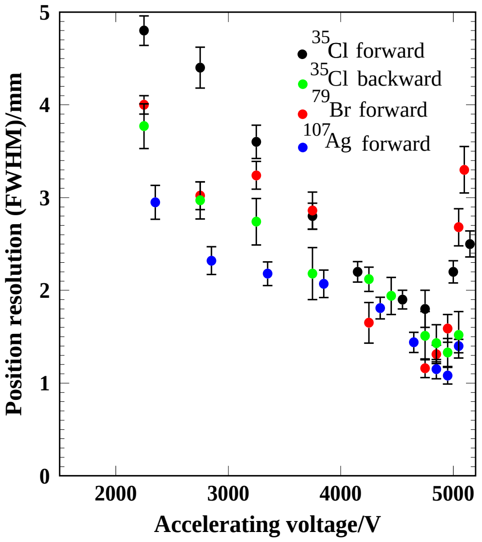

Figure 5.28: Position resolution as a function of the accelerating voltage for different ions and types of electron emission. Optimal results are achieved for accelerating voltages greater than 4 kV. This effect can be explained by strongly minimising the angular electron spread. At some point, where the electrostatic mirror becomes semi-transparent, the position resolution reaches its maximum. However, this mode of operation is not favoured, since then the system efficiency is compromised. Increasing the foil potential further, leads to degrading the position resolution. At this stage, only small portion of the SEs hits the detector which causes worsening of the MCP anode timing signals.

The ion energies for all measurements are fixed to 40 MeV. The obtained results are comparable to the one reviewed in the paper of F.Busch *et al.* [Busch79], where the impact of 5.9 Mev/u Xe-ions beam on a position-sensitive MCP setup is discussed.

Since the heavier projectiles are capable of ejecting more SEs, the position resolution tends to improve with increasing the ion Z number and the foil bias. On the other side, the accelerating potential could not be kept arbitrary high, since then the system efficiency rapidly drops down. Moreover, we have shown that increasing the accelerating potentials at some point does not improve, but even degrades the position quality information. One also possible explanation to the fact is the presence of a de-focusing mechanism arising from the field around the mirror wires [Berg89].

Chapter 6

First photo-fission experiments at ELBE accelerator

In this Chapter, the performed at the bremsstrahlung facility in ELBE accelerator experiments will be discussed. For the first time, bremsstrahlung induced photo-fission measurements with mirror type MCPs will be reported.

6.1 The ELBE accelerator

A new superconducting electron linear accelerator of high brilliance and low emittance (ELBE) has been established at the site of Forschungszentrum Rossendorf. The machine is capable of delivering continuous wave electron beams with maximum energy of 40 MeV at a maximum average current of 1 mA [Gabr00]. A 250 keV-thermionic direct current (DC) electron gun unit suits for electron preacceleration, while electron pre-bunching takes place in a two radio frequency (RF) buncher section. Two 20 MeV-superconducting linear accelerator modules serve for main acceleration. Each accelerator module utilises standing RF cavities operated at a frequency of 1.3 GHz. Two 9-cell superconducting niobium cavities are operated in a cryo-module with superfluid liquid helium at 1.8 K. Each cavity is driven by a 10 kW klystron amplifier. The maximum accelerating gradient is 15 MV/m. The basic micro-pulse rates of the accelerator are 26 and 260 MHz having pulse lengths of 5 ps. The rate of 26 MHz can be reduced by factors of 2-256. A schematic diagram of a cryostat with the niobium cavities is shown in Fig. 6.1.

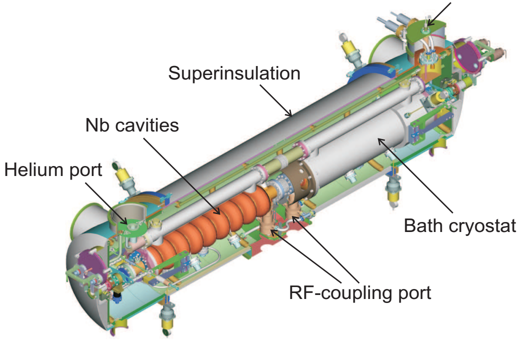

Figure 6.1: The ELBE cryogenic accelerator module [Gabr00].

Some of the ELBE accelerator parameters used at the first accelerator section are presented in the following:

- Electron beam energy: 6 – 18 MeV
- Max. average beam current: 1 mA
- Max. bunch charge: 77 pC
- Micropulse duration: 2 ps
- Micropulse repetition rate: 26 MHz
- Macropulse repetition rate: 1 – 25 Hz
- Macropulse duration: 0.1 – 40 ms / cw

6.2 The bremsstrahlung setup at the ELBE accelerator

Since the photo-fission chamber has been incorporated in the bremsstrahlung setup at the ELBE accelerator primary optimised for nuclear-resonance-fluorescence (NRF) experiments, a short description of the facility will be given.

A lay-out of the bremsstrahlung setup is shown in Fig. 6.2. The electron beam produced from the first module of the accelerator (energies up to 20 MeV) is deflected by 45° from the main beam line to the experimental area by a non-dispersive system of two dipole magnets and quadrupole magnets for beam focussing.

The bremsstrahlung is produced by means of a radiator [Wagn99] made of a thin niobium foil [Schi03a]. It transforms part of the kinetic energy of the electrons into electromagnetic radiation. The metallic radiator foil is embedded in a water-cooled holder with six radiator positions. The remaining beam portion is deflected by a 45° purging magnet [Schi03b] to an electron-beam dump.

A collimator with specially optimised geometry made of pure Al (99.5 %) [Schi02a] with a length of 2.6 m and an opening angle of 5 mrad, collimates the bremsstrahlung cone to a narrow beam. A hardener [Schi02b] positioned in front of the collimator modifies the shape of the bremsstrahlung spectrum. It is a cylindrical absorber made of aluminium with a length of 10 cm, mostly suited for absorption of low energy photons.

The photon beam after irradiating a NRF target is finally absorbed by a photon-beam dump. Its primary role is to minimize the background from scattered photons [Wagn01a]. It is made of polyethylene (PE) and shielded with 2 mm cadmium foil and 10 cm thick lead walls.

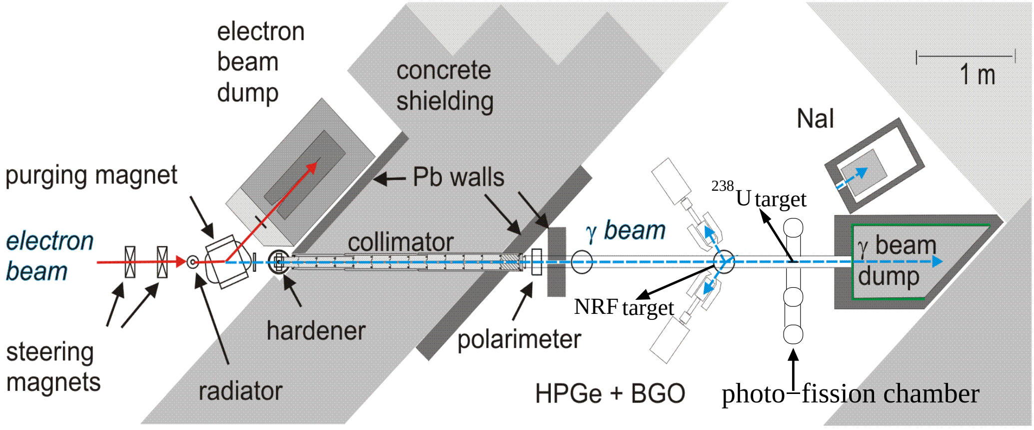

Figure 6.2: The bremsstrahlung facility at the ELBE accelerator. The photo-fission chamber is positioned close to the beam dump.

A NaI detector, placed at 25° relative to the beam axis is used for flux monitoring purposes.

For the purpose of NRF experiments, a setup of high-purity germanium (HPGe) detectors has been implemented [Schw05]. It consists of four HPGe detectors with 100 % efficiency relative to a 3"× 3" NaI detector. Two of them are fourfold segmented detectors, placed vertically at 90° relative to the beam, and the other two HPGe detectors are placed horizontally with possible varying angles from 90° to 127°. The HPGe detectors are shielded with escape-suppression shields of bismuth germanate (BGO) scintillation detectors for background reduction. For photon flux calibration, the NRF target is combined with an additional target of an isotope with known transitions and cross section for γ scattering. This calibration is used in the test photo-fission experiments also, as demonstrated in Section 6.7

The bremsstrahlung produced from electrons having a kinetic energy E_e is to some extend polarized with a maximum degree of polarization defined at an angle of μ/E_e, where μ is the rest energy of the electron. In experiments with polarised photons it is important to know the degree of polarisation of the photon. To deduce the polarization degree, a polarization monitor is being used based on the deutron photodisintegration process. Protons and neutrons are emitted preferentially in the direction of the electric field vector of the polarized bremsstrahlung. The degree of polarization can be obtained by measuring the azimuthal asymmetries of the protons. The polarization monitor setup [Schw05] comprises of four silicon detectors positioned perpendicular to the photon beam at azimuthal angles of 0°, 90°, 180° and 270° in a cylindrical reaction chamber. The detectors have a thickness of 500 μm and area of 600 mm^2. A CD$_2$ foil of 40 μm serves as a target. The distance between the deuterium foil and the silicon detectors is 11 cm. Since the energies of the incident photons are directly correlated with the measured proton energies, the proton spectra can be also used to determine the bremsstrahlung end-point energy. Example proton spectra measured with the silicon detectors at different electron-beam energies are presented in Section 6.5.

6.3 The test photo-fission setup

A test photo-fission measuring setup as shown in Fig. 6.3 has been installed in the beam line of the bremsstrahlung facility at the ELBE accelerator. In order to minimise the background contribution coming from the NRF target, the reaction chamber is nested just close to the photon-beam dump. The fission target is inserted in the beam line by means of specially designed movable holder.

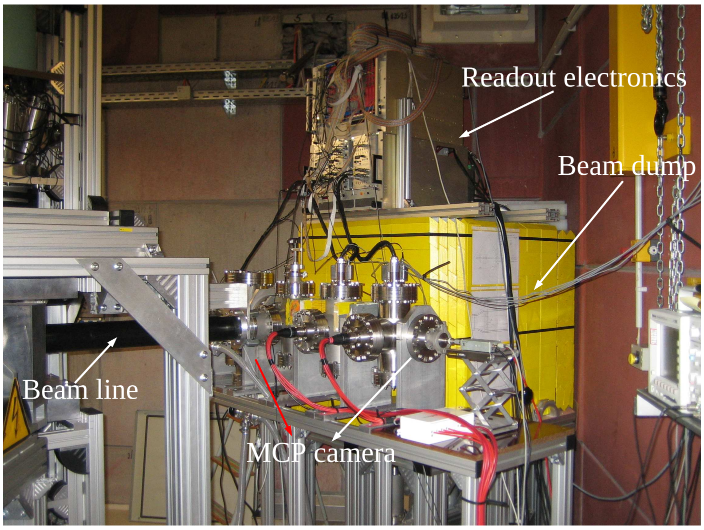

Figure 6.3: Overview of the experimental setup. The bremsstrahlung beam comes from the left. To reduce the background from the NRF target, the photo-fission chamber is positioned close to the photon-beam dump which contains the readout electronics on its top. The achieved vacuum is better than 10^{-8} mbar, which is required for the safe operation of the channel-plates.

Figure 6.4 gives a detailed overview of the measuring setup.

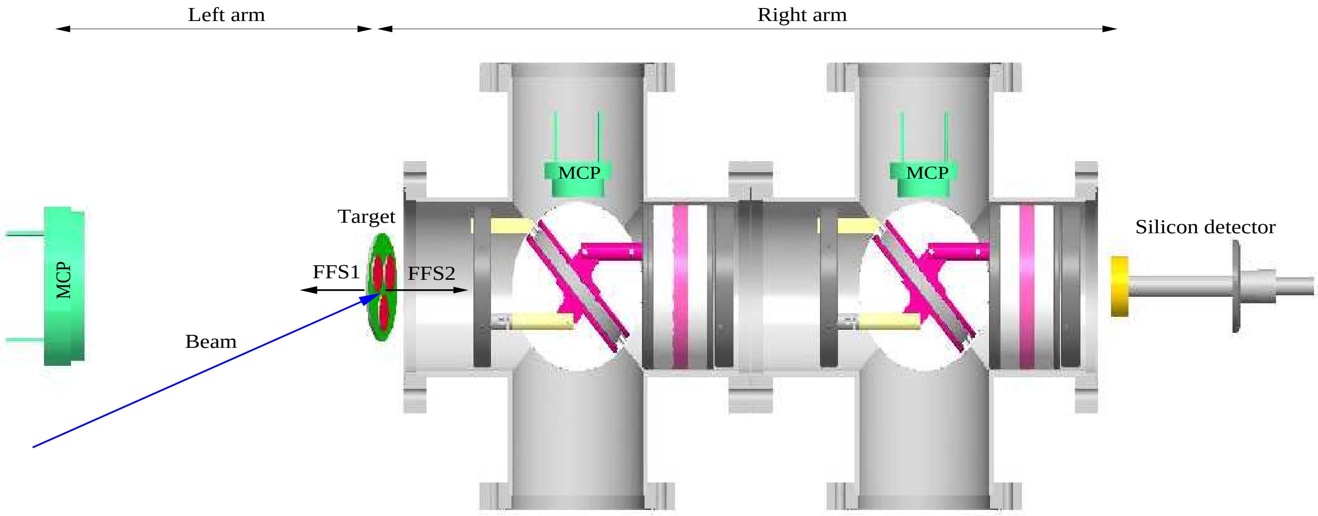

Figure 6.4: The experimental photo-fission TOF setup. It can be principally devided in two functional components - left and right arm. The left arm is an 80 mm diameter MCP detector with a position sensitive anode. It is positioned 45 cm away from the UF_4 fission target. The right arm consists of two 40 mm diameter mirror detectors, operated in "backward" mode and supplied consequently with 300 and 168 $\mu g/cm^2$ PETP foils for SE production, seperated by a distance of 27 cm. The first foil sits 36 cm from the target. Approximately 19 cm from the second foil, a 500 μm ORTEC silicon detector with an active area of 600 mm^2 has been installed.

Figure 6.5 shows the combined UF_4 fission target.

Figure 6.5: The combined fission target. It contains ^{238}U in the form of UF_4 on a 40 $\mu g/cm^2$ carbon backing. The target comprises of three elements with ^{238}U masses of 520, 550 and 650 $\mu g/cm^2$, and is supported by a special holder attached to a dedicated mechanism for insertion in and out of the beam line.

A special differential vacuum pumping approach, as revealed in Fig. 6.6, allowed for obtaining stable vacuum condition better than 10^{-7} mbar. This is also additionally contributed by the implemented copper gasket seals.

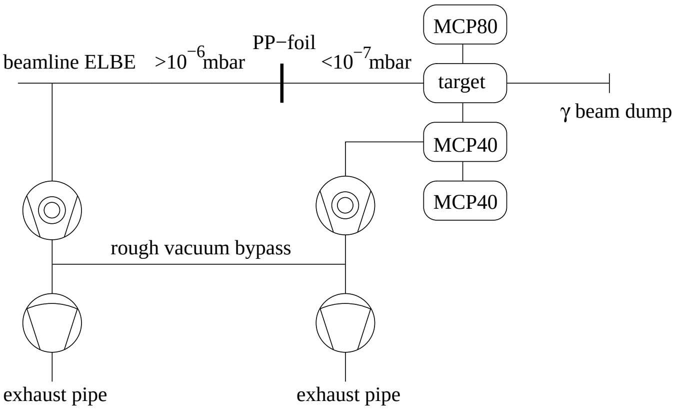

Figure 6.6: The differential pumping system. The high vacuum circuit of the fission chamber is separated from the rest of the beam line by means of a 8 μm polypropylene (PP) foil. Simultaneous vacuum drop at the two sides of the differential system preventing the PP foil from mechanical destruction when venting is enabled through rough vacuum bypass.

6.4 Readout and control

It is important to estimate the TOF of the fission fragments for the given geometry of our setup. This would enable us to adjust the micro-pulse accelerator rate in a such a way that a particular event is beeing detected within two accelerator pulses. In such a manner, a certain fission event can be theoretically correlated to the time of fission (given by the accelerator pulse with a precision better than 30 ps).
In Fig. 6.7 is presented the postneutron mass distribution of ^{238}U for different bremsstrahlung end-point energies.

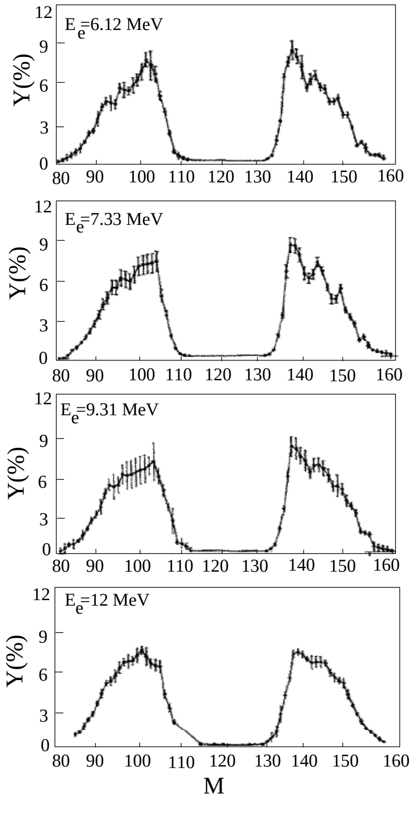

Figure 6.7: Picture adopted from [Pome94] showing the postneutron mass distribution of ^{238}U for different bremsstrahhlung end-point energies: E_e=6.12, 7.33, 9.31 and 12 MeV. The distribution yield is normalised to a total yield of 200%. The reported total kinetic energy <TKE> of the fission fragments for the last case d) is in the order of 168 MeV.

If one consideres the momentum conservation law, then: $m_1v_1{=}m_2v_2$, where m_1 is the mass of the first and m_2 the mass of the second fission fragment and v_1 and v_2 consequently their velocities. The relation can be also rewritten as: $(m_1^2v_1^2)/2 = (m_2^2v_2^2)/2$. From here, the following dependence can be derived: $m_1E_1 = m_2E_2$, where E_1 and E_2 are the kinetic energies of the first and second fission fragment. In other words: $m_1/m_2 = E_2/E_1$. Knowing that <TKE> equals 168 MeV for two particular masses m_1 and m_2 taken from Fig. 6.7, we can deduce their E_1 and E_2 values. The velocities of the fission fragments then can be expressed as follows: $v_1 = (2E_1/m_1)^{\frac{1}{2}}$ and $v_2 = (2E_2/m_2)^{\frac{1}{2}}$.

Since the left arm of the spectrometer is comprised of only one MCP detector with a target-detector distance - l_1, then: $t_1 = l_1/v_1$, where t_1 is the left arm TOF. The right spectrometr arm consists of two mirror detectors with foils, therefore the TOF of the fission fragment can be principally devided into two components: t_2 - TOF between the target and the first foil for SE production, and t_3 - TOF between the two foils. Obtaining t_2 is rather straightforward: $t_2 = l_2/v_2$. As the fission fragment penetrates the first foil, it suffers an energy loss proportional to its Z^2. This leads to a given velocity change, which is also dependent upon the particular foil thickness. To account for this effect, a SRIM simulation has be been performed taking as an input the energy of the fission particle before passing the foil and giving as a result the particle outgoing energy. In this way the theoretical TOF between the two foils can be estimated. Bearing in mind these preconsiderations, we find out that an accelerator micropulse frequency of 13 MHz (77 ns pulse separation) meets the above mentioned requirements best.

The readout scheme of the detector setup is presented in Fig. 6.8.

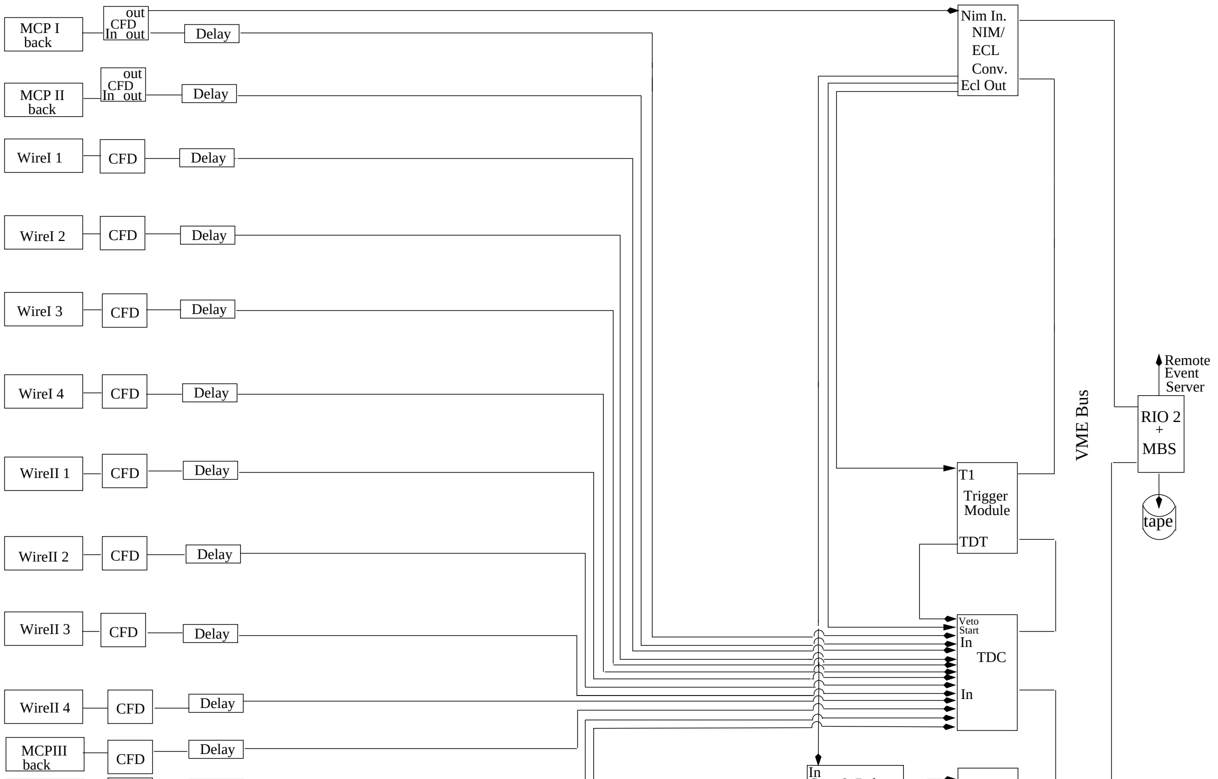

Figure 6.8: The readout scheme.

The DAQ trigger is produced by the rear side of the first mirror MCP stack. It also initiates a common start signal in the CAEN V775 VME TDC module. All the other readout signals - first and second mirror MCP back comprising the right spectrometer arm plus the MCP back from the left spectrometer arm, anode wires and the accelerator pulse after a certain delay generate TDC stops. The presence of the accelerator signal enables us to sort out only those events in the MCP detectors which have come in coincidence with it. The MCPs CFD (model CFT-5388) thresholds are adjusted in such a manner as to prevent noise events as much as possible. The in-beam trigger rate seldom exceeded 0.5 kHz. This taking into account the DAQ TDT, which is in the order of 120 μs, leads to dead time effects of less than 5 %. For monitoring purposes, a Si detector as displayed in Fig. 6.4 has been installed. It is read out by a CAEN V555 ADC accepting gates from an ORTEC GG8010 Gate-and-Delay module, fired by each trigger pulse. The gain of the ORTEC 671 Spectroscopic Amplifier is set low, such that signals from scattered electrons and γ-quanta are not recorded by the Si detector.

6.5 Determination of the bremsstrahlung end-point energy

Because the energies of the incident photons correlate with the measured by the polarization monitor described in Section 6.2 proton energies, the proton spectra can be used to determine the bremsstrahlung end-point energy. Example proton spectra measured at different electron-beam energies are presented in Fig. 6.9 a). A spectum of a mixed ^{239}P-^{241}Am-^{244}Cm α-particle source used for energy calibration is given in Fig. 6.9 b).

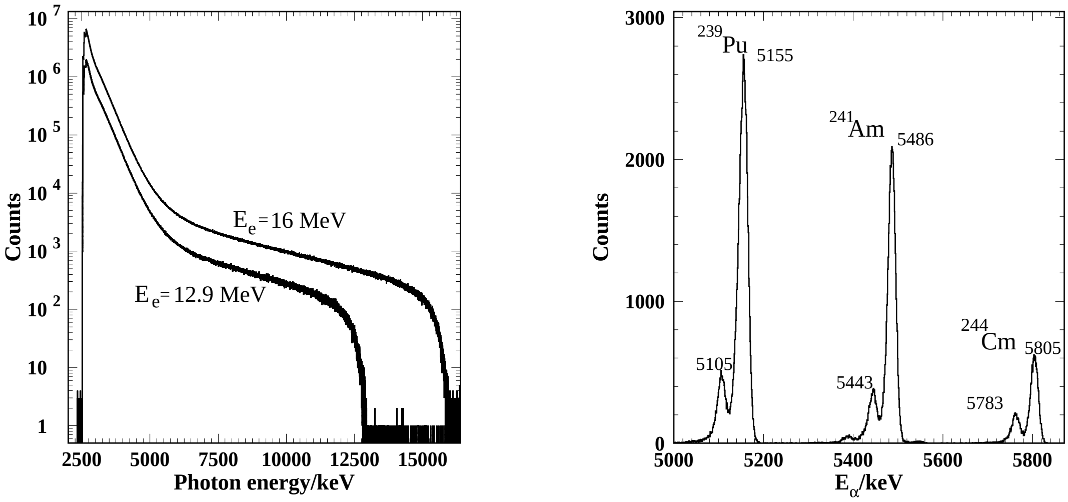

a) b)

Figure 6.9: Measured proton spectra a) at different electron beam-energies and b) of a mixed ^{239}P-^{241}Am-^{244}Cm α-particle source.

The spectrum of the incident photons $N_\gamma(E_\gamma)$ times the cross-section for the deutron disentigration σ_{dis} can be obtained by rescaling the measured proton spectrum according to: $\sigma_{dis}N_\gamma(E_\gamma){\sim}N_p(E_p)$, with $E_\gamma = E_p + E_n + E_B$. Here, with N_γ and N_p we denote the photon and proton intensities at given energies. Respectively, $E_p \sim E_n$ are the kinetic energies of the proton and neutron and $E_B = 2225$ keV is the deutron binding energy. The electron energy corresponds to the end-point energy of the rescaled photon spectrum with an uncertainty of about 0.1 MeV [Schw05].

6.6 Experimental results

The first test bremsstrahlung induced photo-fission experiments of ^{238}U at the bremsstrahlung facility of the ELBE accelerator are performed within two runs with electron energies of 12.9 and 16 MeV respectively, with typical beam currents of 460 μA. In order to obtain higher flux intensity, the first 16 MeV run is conducted without beam hardener. The second measurement has been performed with hardener parallel to a photon-scattering experiment with implemented ^{87}Rb and ^{11}B target for flux calibration purposes. The flux calibration procedure for the two bremsstrahlung end-point energies will be treated in Section 6.7.
Two example TOF experimental spectra between the mirror detectors in the right spectrometer arm are depicted in Fig. 6.10 a) and b). The flight path between the two foils is 27 cm. As expected for asymmetric fission, two distinct groups of flight times show up. The more sharply peaked distribution at the shorter flight times belongs to the light fragments, while the spread out distribution corresponds to the heavy ones. The quality of the data is demonstrated by the clearcut separation of the TOF peaks for the mean light and heavy masses. The peak to valley ratio P/V for the mean light mass is better than 14 for both measuring cases.

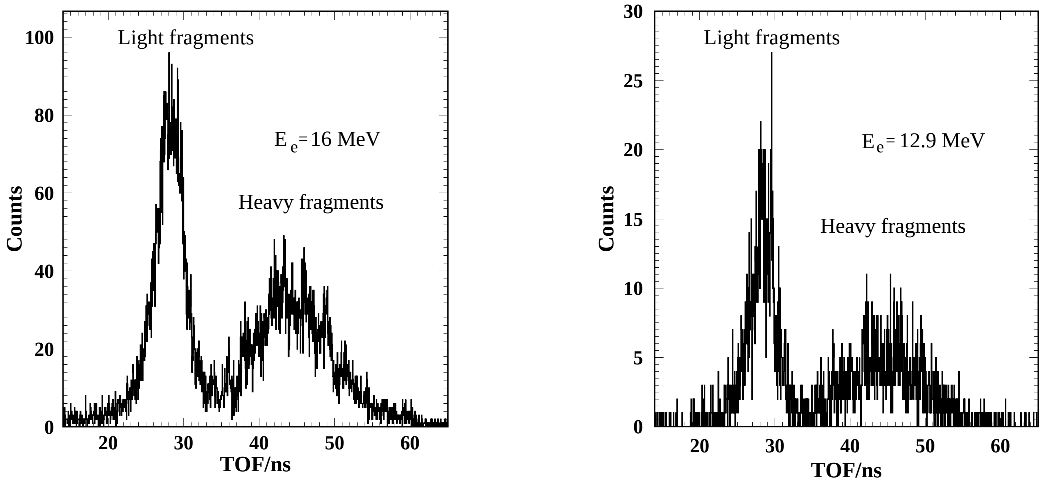

a) b)

Figure 6.10: Measured fission fragment time difference distribution spectra between the two mirror MCPs for 16 MeV end-point bremsstrahlung energy a) and 12.9 MeV b). It is assumed that the mirror MCP branches have equal cable delays and can be treated completely symmetrically. The flight path between the two foils is 27 cm. One sees a clear separation of the mean light and heavy mass TOF peaks.

Similar in form TOF spectra, obtained by the photo-fission of ^{235}U under intense neutron flux conditions with a spectrometer incorporating multichannel-plate detectors are presented in the

work of Oed *et al.* [Oed80]. For complicity, we have to mention the work of Kuznetsov *et al.* [Kuze00] as well. A fission fragment TOF spectrum from a ^{252}Cf fission source with a P/V ratio similar to the one reported above is presented. The TOF detectors are mirror MCPs and the flight distance equals 20 cm. The there described MCP assemblies consist of two rectangular plates (10×22 mm) mounted in Chevron configuration with a gain of 10^7-10^8. The signal decoupling is utilised through a flat anode directly connected to a 50 Ω cable. The particles to be detected pass through 20 μg carbon foil (10×20 mm) and all harps are reported to have transparency of 98 %. The FWHM of the TOF α-particle peak accompanying the fission events from ^{252}Cf is found to be around 400 ps.
Although the measuring time for the two experimental photo-fission runs is almost equal, the number of the collected events strongly differs. That is due to the fact that the ^{238}U photo-fission cross section reaches its maximum above 13 MeV and the 16 MeV measurement is performed without beam hardener, contributing additionally to higher flux intensities and consequently higher fission yield. In these experimental test runs, we do not aim at one-by-one fission fragments mass resolution, since this would be the purpose of a more specialised experiment, utilising a much thinner fissile source and considerable better statistics. Another approach, resulting in higher fission yield is the electron-induced fission from the direct intense electron beam of the accelerator.
In Fig. 6.11 a) and b) the fission fragment velocity distribution spectra are shown.

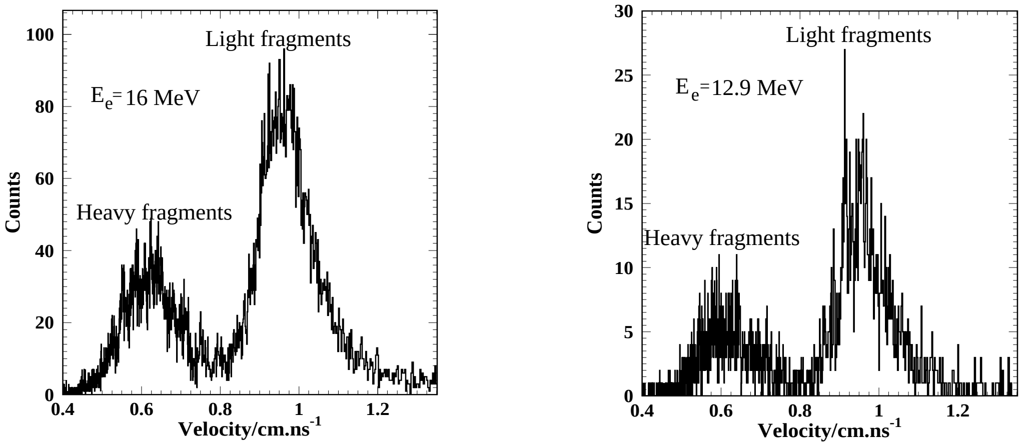

a) b)

Figure 6.11: Velocity distribution spectra for the TOF between the two mirror detectors (right arm) without SE foil and fission source energy loss correction. The ratio - v_l/v_H, where v_l denotes the mean light mass velocity and v_H the heavy one, approximates 1.5 for the two velocity spectra, which is in a good agreement with other literature studies [Milt62].

From the spectra applied above, it becomes obvious that a setup employing electrostatic mirrors with foils for SE production is suitable for photo-fission experiments with bremsstrahlung. In different setups, one could expect a larger background contribution originating from Compton electrons, pair production and scattered γ-quanta. However, the useful signal in our timing spectra is not blurred by background events, since the foil efficiency for the simultaneous electron or γ detection by the two mirror detectors, especially in the MeV region is pretty low as compared to the one for heavy projectiles. Nevertheless, one has also to point out, that the overall MCP efficiency values are strongly correlated to the individual CFD settings as well. In our case, a great effort has been made to set the CFD thresholds in such a manner as to suppress the noise events optimally. For monitoring purposes as already showed in Fig. 6.3, a Si detector has been installed behind the two foils in the right spectrometer arm. The gain of the Spectroscopic Amplifier connected to it is set as low as possible, such as to prevent the detection of γ-quanta and electrons. One example pulse-height spectrum as recorded by the 500 μm ORTEC Si detector is displayed in Fig. 6.12. Its detection efficiency for the impinging fission fragments is considered to be 100%.

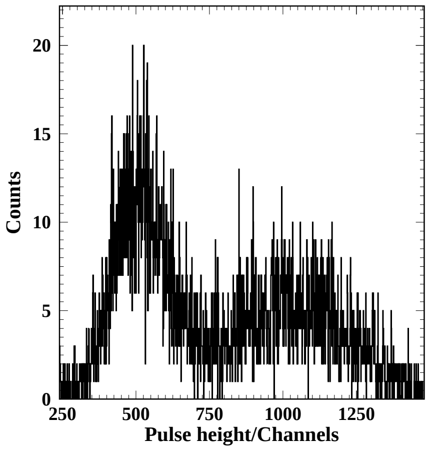

Figure 6.12: Pulse-height ADC spectrum of the fission fragments after passing the two foils for SE production. The left peak corresponds to the heavier mass fission fragments group, while the right structure to the lighter one.

It is well known, that projectiles with high Z number detected in such kind of detectors suffer a so-called pulse height defect (PHD) as compared to protons or α-particles. Therefore, their energy calibration requires an individual parametrisation of the response function to the different heavy ions. The pulse height defect worsens tremendously the resolution capabilities of the particular detector due to effects largely discussed in references like [Leo94]. Example TOF spectra gated with the right and left ADC energy peaks are given in Fig. 6.13.

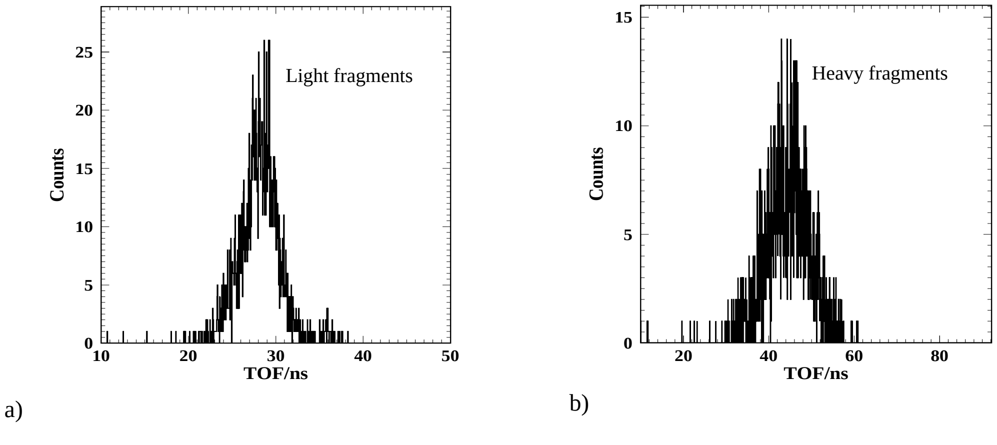

Figure 6.13: TOF spectrum gated with the right (light fragments) a) and left (heavy fragments) b) pulse-height distribution structures from Fig. 6.12.

Fragments-coincidence-scatter plot between the left and the right spectrometer arm which once again demonstrates that the observed events come from fission is presented in Fig. 6.14. Two groups of complementary fission events are well separated.

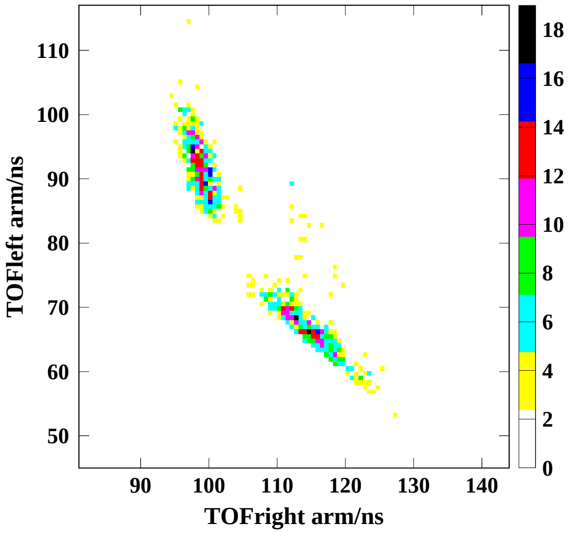

Figure 6.14: TOF correlation between the left and the right spectrometer arm.

The correlation is formed by the coincidence counts between the big - 80 mm diameter MCP (left arm) and the second mirror detector (right arm) when an accelerator signal is also present.

6.7 Determination of the photo-fission production rate

Since our first experimental tests are performed for two end-point bremsstrahlung energies, it is principally possible to estimate the photo-fission production rate and compare the obtained results with existing in literature data.
For the purpose of our calculations, we first need to deduce the correct photon fluxes as seen by the photo-fission target.
As already mentioned in Section 6.2, the NRF target is combined with additional calibration target of ^{11}B with known transitions and cross sections for elastic γ scattering. Figure 6.15 contains a ^{87}Rb spectrum with labeled ^{11}B peaks taken from the HPGe detectors positioned at 127° relative to the photon-beam direction during our 12.9 MeV measurement run. The photon flux $\Phi_\gamma(E_\gamma)$, defined as the number of incident photons with energy E_γ per unit time and area may be expressed as:

$$\Phi_\gamma(E_\gamma) = \frac{A_{\mathrm{T}}^{\mathrm{cal}}(\theta, t_{\mathrm{live}})}{\epsilon(E_\gamma,\theta) N_{\mathrm{T}}^{\mathrm{cal}} I_{\mathrm{S,T}}^{\mathrm{cal}} W(\theta) t_{\mathrm{live}} S}, \tag{6.1}$$

where $A_{\mathrm{T}}^{\mathrm{cal}}(\theta, t_{\mathrm{live}})$ denotes the total peak area of a given ^{11}B transition, $\epsilon(E_\gamma,\theta)$ is the detector efficiency, $N_{\mathrm{T}}^{\mathrm{cal}}$ shows the number of the calibration target nuclei, $I_{\mathrm{S,T}}^{\mathrm{cal}}$ is the integrated scattering cross section, $W(\theta)$ an angular correlation function and t_{live} and S are consequently the detectors live time and the projected area of the calibration target on a plane perpendicular to

the beam.
The target area density is given by:

$$N_{\mathrm{T}}^{\mathrm{cal}} = \frac{M^{\mathrm{cal}}}{m_{\mathrm{mol}}^{\mathrm{cal}}} \cdot \frac{N_{\mathrm{A}}}{S}, \tag{6.2}$$

where M^{cal} and $m_{\mathrm{mol}}^{\mathrm{cal}}$ are the mass and the molar mass of the calibration target and N_A is the Avogadro number. The NRF target is usually a disk with a diameter of 2 cm tilted under 45° relative to the beam.

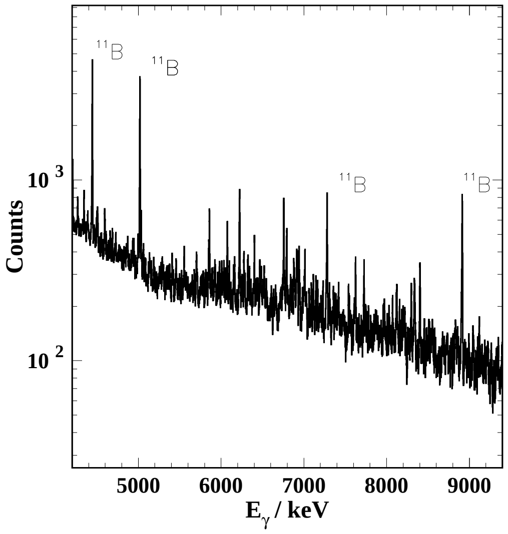

Figure 6.15: HPGe detector spectrum of photons scattered from ^{87}Rb during the irradiation with bremsstrahlung produced by electrons with a kinetic energy of 12.9 MeV. The labelled peaks are transitions in ^{11}B combined with the ^{87}Rb target for the photon flux calibration.

For the approximation of the bremsstrahlung spectrum, we apply an analytical expression, known as “Schiff formula” [Shif51]. The first relativistic calculations of the bremsstrahlung spectrum, however, have been performed by H. A. Bethe and W. Heitler (BH) in 1934 using quantum electro-dynamics. By integrating the cross section for bremsstrahlung given by BH over the azimuthal angle, L. Schiff succeeded in deriving an analytical formula for the bremsstrahlung distribution. It is known that the “Schiff formula” overestimates the bremsstrahlung end-point energy, but with a discrepancy becoming significant at electron energies below 10 MeV.
By applying Eq.(6.1), we can deduce the flux values according to the known ^{11}B transitions in the spectrum of scattered photons. We then calculate the bremsstrahlung distribution by using the “Schiff formula” for the 12.9 MeV end-point energy case and by folding it with the attenuation of the hardener. To obtain the photon flux spectral distribution $\Phi_\gamma(E_\gamma)$, we normalise it to the derived from the ^{11}B flux values. The attenuation of the photons in the Al hardener is simulated with the GEANT3 programming package[1].
However, calculating the photon flux for the 16 MeV end-point energy measurement is not straightforward, since during that run we have not implemented NRF and flux calibration targets. Therefore, we rely on the proton spectra information from the polarization monitor, described in Section 6.2. The Si detectors and the CD$_2$ foil remain unchanged for the two measuring cases. This allows us to implement the following procedure:

---

[1] The GEANT3 simulations are performed by Dr. G. Rusev.

1) Divide the collected proton spectrum for the 12.9 MeV case by the disintegration cross section σ_{dis} taken from Ref. [Beth50] and the measuring time t_{live} to obtain the distribution of the incident photons;
2) Normalise the obtained distribution to the 12.9 MeV end-point energy photon flux $\Phi_{\gamma}^{12.9MeV}(E_{\gamma})$ from ^{11}B with a normalisation coefficient B;
3) Divide the collected proton spectrum by the disintegration cross section σ_{dis} and the measuring time t_{live} for the 16 MeV end-point energy measuring case;
4) Multiply the obtained distribution with the normalisation coefficient from step 2) - B;
5) Calculate the bremsstrahlung spectrum using the "Schiff formula" for 16 MeV end-point energy and normalise it to the resulting distribution from step 4). This how the photon flux $\Phi_{\gamma}^{16MeV}(E_{\gamma})$ is deduced.
A resulting picture of the two flux distributions at the position of the NRF target for the different measuring cases is presented in Fig. 6.16.

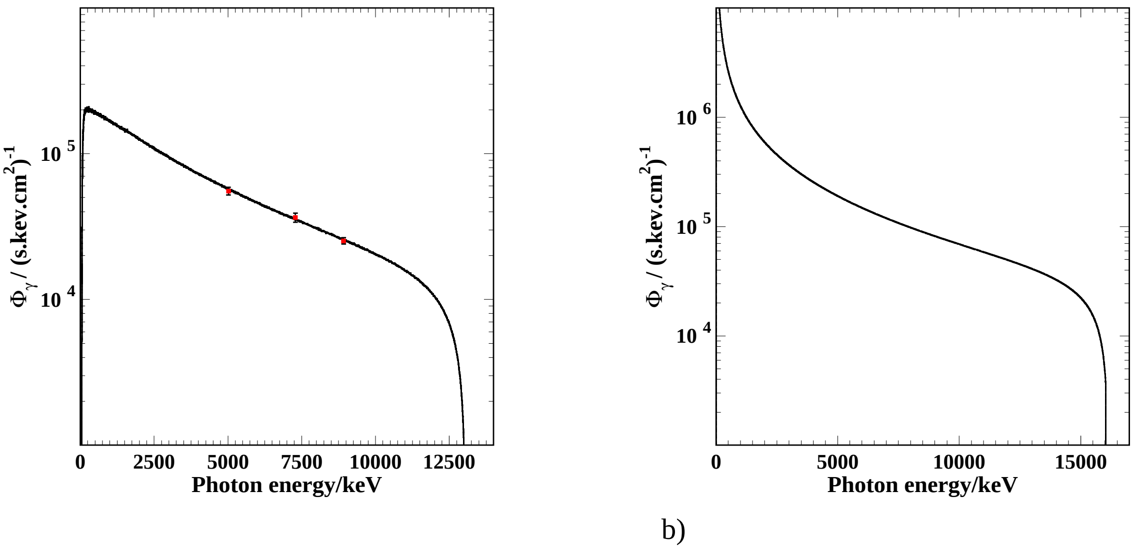

Figure 6.16: The resulting flux distribution spectra at the place of the NRF target. In Fig. 6.16 a), we see the normalised to ^{11}B flux (red calibration points), corresponding to an electron end-point energy of 12.9 MeV. In Fig. 6.16 b), we have plotted the flux for the 16 MeV measuring case, calculated according to the above described algorithm. It principally yields higher flux values as compared to the a) case. This is mainly due to the higher end-point measuring energy and the absence of hardener which additionally modifies the form of the bremsstrahlung spectrum.

Since one of our experimental runs is with included ^{11}B and ^{87}Rb targets placed at the site of the NRF setup, special considerations taking into account γ-absorption and scattering effects inside the target volumes have to be made. This would allow us to deduce the correct photon flux as seen by the fission target. Such information plus the distance of the fission target from the NRF one and its exact geometrical composition and position relative to the photon beam has been served as an input for a GEANT3 simulation. Photons with bremsstrahlung distribution are emitted from the place of the radiator along the beam collimator described in Section 6.2. The simulation outputs the ratio between the number of photons falling on the combined NRF target and those which penetrate through it without being absorbed or scattered, entering the geometrical space defined by the photo-fission target. The result of the simulation can be seen in Fig. 6.17. Similar simulation without NRF targets included, yields photon ratios between the photo-fission and NRF sites of 0.3.

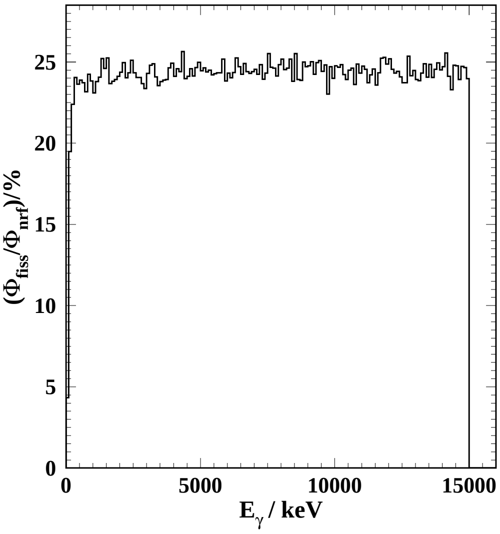

Figure 6.17: Photon ratios between the two experimental (NRF and photo-fission) sites as a function of bremsstrahlung energy. It remains relatively constant for the whole energy range except for the low energy region, where greater attenuation effects take place.

For the total number of TOF counts between the two mirror detectors (N_f) for a live measuring time - t_{live}, one can write the following equation:

$$N_f = \Phi_\gamma \sigma(\gamma, f)\Omega\epsilon(1,2)N_{\mathrm{T}}^{\mathrm{fiss}} t_{live}, \tag{6.3}$$

where Φ_γ is the photon flux, $\sigma(\gamma, f)$ denotes the photo-fission cross section for ^{238}U, Ω defines the solid angle between the target and the second mirror detector, and $\epsilon(1,2)$ shows the efficiency with which a particle is detected simultaneously by mirror detectors one and two.
The number of the target nuclei is given by:

$$N_{\mathrm{T}}^{\mathrm{fiss}} = \frac{M^{\mathrm{fiss}}}{m_{\mathrm{mol}}^{\mathrm{fiss}}} \cdot N_{\mathrm{A}}, \tag{6.4}$$

where M^{fiss} and $m_{\mathrm{mol}}^{\mathrm{fiss}}$ are the mass and the molar mass of the fission target and N_A is the Avogadro number.
The efficiency $\epsilon(1,2)$ that a given particle is recorded simultaneously in the TOF spectrum between the mirror MCPs is determined by relating the TOF to the Si detector ADC spectrum counts, and by taking into account the grids transmission factor too.
The measured event number in the TOF spectrum N_f has to be corrected for false coincidence counts, which is the product of the MCPs single triggering rates and the fission time coincidence window. Additionally one has to take into account the contribution from background events like scattered electrons and cosmics during the measuring period.
Knowing the efficiency, the opening angle, the true number of fission events, the number of the fission target nuclei and the bremsstrahlung flux distributions for the two end-point energies at

the place of the combined photo-fission target, one can estimate the experimental photo-fission production rates and compare the obtained result to other data in the form like presented in Table 6.1.

	ELBE	Caldwell
Energy (MeV)	$10^{18}\int_0^{Ekin}\Phi(E_\gamma)\sigma(\gamma,f)dE_\gamma$ (s^{-1})	$10^{18}\int_0^{Ekin}\Phi(E_\gamma)\sigma(\gamma,f)dE_\gamma$ (s^{-1})
12.9	6.72 ± 0.70	5.98 ± 0.57
16	44.94 ± 4.27	39.84 ± 4.06

Table 6.1: Measured at ELBE and compared to the data of other authors (Caldwell [Cald80]) photo-fission production rates for bremsstrahlung with end-point energies of 12.9 and 16 MeV. The obtained with monoenergetic beams photo-fission cross sections for various energies by Caldwell *et al.* are multiplied by the calculated flux distributions at the place of the photo-fission target. The resulting integrals, yield values which we compare to the experimentally deduced from Eq. 6.3 production rates. Systematic uncertainties arising from background subtraction and efficiency calibration do not exceed 7 %.

Chapter 7

Summary and Outlook

The first working prototype of a novel TOF spectrometer for fission-fragment and exotic nuclei has been built and tested successfully.

In the first part of this work, we focused on the relevant methods and techniques of building a device of such type. The functionality of the different spectrometer components was revealed in detail too. As an important part of the setup, special attention has been paid to the electrostatic mirror and its properties. An unique method for the SE foil thickness determination with α-particles was presented. Values for the mirror transmission and scattering were deduced. A dedicated SIMION 3D simulation showed that introducing serpentine like wires with pitch distance of 1 mm is capable of providing transparency of more than 97 % without significant impact on the time and position resolution. A condition for an optimum isochronous electron mirror transport has been found as well.

Since the performance of the MCP detectors is crucial, optimised schemes for their high voltage supplies have been implemented successfully. Further setup enhancement was achieved by introducing SMD signal decoupling elements close to the detectors surface. Thus, we succeeded in avoiding signal deterioration coming from the additional capacitances and inductivities caused by extra cable lengths.

Because the MCP signal decoupling originally takes place by means of rings with not well defined impedance, impedance matching problems arise, causing as a result signal ringing and distortion. An approach towards solving this problem was building a special, fast wide-band transimpedance amplifier. Using its circuit mounted directly on an MCP SMA vacuum feedthrough, a significant reduction of the signal ringing was observed, while maintaining the detector signal rise time. In order to process optimally the multichannel-plate detector signals, a new state of the art CFD based on the ARC technique with very low threshold capabilities and optimised walk properties has been developed and incorporated into the setup.

In our first laboratory test measurements conducted with α-particle source, we demonstrated the setup ability to resolve pattern images placed directly in front of the MCP or reflected by the electrostatic mirror. The obtained position resolution for the second case is in the order of 2 mm. We showed that the system detection efficiency for ions like He is less than 30 %. This is mainly due to the low number of the liberated electrons from the SE foil in the 2π hemisphere, which is estimated to be around 10 for α-particles. In a setup consisting of two mirror MCP detectors, we could successfully observe the TOF spectrum from a mixed (^{226}Rn, ^{222}Rn, ^{210}Po, ^{218}Po, ^{214}Po) α-source and compare it in a good agreement with a SRIM simulation.

Measurements performed at the FZ Dresden-Rossendorf 5 MV tandem accelerator enabled us to learn more about the response of the TOF detectors to various beams of heavy ions. The first in-beam experiments clearly showed that the applied setup consisting of two mirror detectors is capable of resolving different ^{35}Cl beam charge states. In a combination with the specially designed wide-band transimpedance amplifiers and dedicated CFDs based on the ARC technique, we managed in retrieving in-beam time resolutions of 170 ps per TOF detector and mass resolving power of around 40 for a flight path less than 0.3 m. By increasing the flight distance, we could principally manage to improve the system resolving power, but at the cost of significantly diminished detector solid angle.

The measurements with $Z > 30$ ion beams showed resulting detection efficiency values greater than 90 %. At foil accelerating potentials approximately two times larger than the mirror deflection voltage, most of the SEs gain enough energy to pass through the electrostatic mirror without being deflected towards the MCP surface. Thus, an abrupt drop of the efficiency curve was observed - the “transparent” mode of the mirror.

Some of the properties of electrons ejected from thin foils by heavy ions have been also investigated. From the MCP pulse height distribution spectra, a number for the forward emitted SEs ejected by 30 MeV ^{35}Cl beam was deduced.

A method for obtaining the SEs energy distribution widths from the drop of the efficiency curve for various ions has been proposed. Assuming that the efficiency curve as a function of the accelerating voltage follows an error function, then its standard deviation would give the standard deviation of the SEs energy distribution. Another method based on the TOF technique for reconstructing the secondary electron velocity and energy distribution was also invented. It was found that the resulting mean SEs velocity closely approaches the one of the beam ions. This phenomenon was attributed to the so-called “convoy” electrons.

The obtained position resolution for beams like ^{35}Cl, ^{79}Br, ^{107}Ag at stable detection efficiency was better than 1.8 mm. It was demonstrated that with increasing the foil accelerating voltage, the position resolution would improve due to the minimised SEs angular spread. Such mode of operation was favoured until the mirror “semi-transparency” regime was reached, after which increasing further the accelerating potential would lead to position resolution worsening. An explanation to the fact could be the deterioration of the anode timing signals or some defocusing effects arising from the mirror wires field at high accelerating voltages. A possible approach towards improving the position resolution would be the incorporation of einzel lenses in the electrostatic mirror [Nank04a]. An even more advanced solution could be replacing the electrostatic mirror with a 45° tilted foil put in a solenoid. The homogeneous magnetic field of the solenoid superimposed on the foil electrostatic accelerating field will cause SEs emitted from the foil to move on helical trajectories until they hit the position-sensitive MCP detector. Such a setup is believed to improve its position resolution down to 1mm [Boug04, Odl96] without influencing system parameters like efficiency and stability.

Test photo-fission experiments were performed at the bremsstrahlung facility in ELBE accelerator. For the first time a spectrometer of this kind was successfully employed for bremsstrahlung induced photo-fission measurements. The setup consisted of two mirror detectors (first arm) and a 80 mm diameter MCP detector (second arm) with a positioned ^{238}U target in between. TOF measurements with two end-point bremsstrahlung energies were carried out - 12.9 and 16 MeV. A clearcut separation of the TOF peaks for the mean light and heavy fission masses was observed. At these experimental test runs, we did not aim at one-by-one fission fragment mass resolution, since this would be a purpose of a more specialised experiment utilising a much thinner fissile source (minimum straggling of the fragments inside the target is required) and considerably better statistics.

It was also possible to estimate the photo-fission production rate for the two measuring cases and compare the obtained results with data from other experiments.

Another way to produce, identify and study nuclei far from stability is to use nuclear reactions at relativistic energies. The R^3B collaboration within the FAIR project at GSI [Fair06] aims to study a wide class of reactions with relativistic exotic beams. For proper identification of the primary exotic nuclei as well as the reaction products, detectors like the one described in the present thesis, possessing high resolving power are required. The final state measurements will include identification and momentum analysis of fragments in large acceptance and high-resolution mode as well as coincident measurements of neutrons, protons, gamma-rays and light recoil particles.

As future photo-fission studies consideration, one can also incorporate such a spectrometer with two symmetrical arms as a part of the newly established nToF facility at ELBE accelerator [Klug07]. Neutrons with energies of up to 10 MeV and intensities approximating 10^7 $\mathrm{cm}^{-2}\mathrm{s}^{-1}$ will be produced from a neutron radiator consisting of a liquid-lead circuit by means of bremsstrahlung photons generated from the electron beam.

Bibliography

[Adac01] J. Adamczewski, M. Al-Turany, H.G. Essel, H. Göringer. Go4: Multitasking Multithreaded Class Library. *GSI Scientific Report 2000 GSI 2001-1*, page 201, 2001.

[Adam66] J. Adams and B.W. Manley. The Mechanism of channel electron multiplication. *IEEE Trans. Nucl. Sci.*, NS-13:88, 1966.

[APE] APE; http://www-aix.gsi.de/computing/ape.htm

[Bart00] R. Barth, D. Yifei, H.G. Essel, R. Fritzsche, H. Göeringer, J. Hoffmann, F. Humbert, N. Kurz, R.S. Mayer, W. Ott and D. Schall. GSI Multi-Branch System. *Gesellschaft für Schwerionenforschung mbH, Darmstadt* , 2000.

[Beck76] G. Beck. Photodiode and holder with 60 psec response time. *Rev. Sci. Instrum.*, 47(7):849, 1976.

[Berg89] T. Bergmann, T.P. Martin, and H. Schaber. High-resolution time-of-flight mass spectrometer: Part I. Effects of field distortions in the vicinity of the wire meshes. *Rev. Sci. Instrum.*, 60(3):347, 1989.

[Beth50] H.A. Bethe and C. Longmire. The Effective Range of Nuclear Forces II. Photo-Disintegration of the Deuteron. *Phys. Rev.*, 77:647, 1950.

[Boug04] E. Bougamont, P. Bourgeois, A. Drouart, C. Mazur, L. Nalpas, E.C Pollacco, M. Riallot. A large tracking detector for low-energy ions. *Nucl. Inst. Meth.*, A 518:129, 2004.

[Burl00] BURLE Industries,Inc; http://www.burle.com

[Busch79] F. Busch, W. Pfeffer, B. Kohlmeyer. A position-sensitive transmission time detector. *Nucl. Inst. Meth.*, 171:71, 1979.

[Cald80] J.T. Caldwell and E.J. Dowdy. Giant resonance for the actinide nuclei: Photoneutron and photofission cross sections for ^{235}U, ^{236}U, ^{238}U, and ^{232}Th, . *Phys. Rev. C*, 21:1215, 1980.

[Chri05] C. Vockenhuber, R. Gloser, W. Kutschera, A. Priller, P. Steiner, K. Vorderwinkler, A. Wallner. The ΔTOF detector for isobar separation at ion energies below 1 MeV/amu. *Nucl. Inst. Meth.*, B 240:490, 2005.

[Cler73] H.G. Clerc, H.J. Gehrhardt, L. Richter, D. Janssen and K.H. Schmidt. Heavy-ion induced secondary electron emission - a possible method for Z-identification. *Nucl. Inst. Meth.*, 113:325, 1973.

[Cyri91] Cyriel Wagemans. *The Nuclear fission process*. CRC Press, Inc., 1994.

[Dera84] W.B. Colson, J. McPherson, and F.T. King. High-gain imaging electron multiplier. *Rev. Sci. Instrum.*, 44(12):1694, 1973.

[Dimi79] Dmitriyev V.D et al. A Start Detector Using Microchannel Plates. *JINR,Dubna*, 7-12290, 1979.

[Eras85] G.D'Erasmo and V. Paticchio. A transmission time detector for low energy light ions. *Nucl. Inst. Meth.*, A 234:91, 1985.

[Essel96] H.G. Essel, J. Hoffmann, N. Kurz, R.S. Mayer, W. Ott, D. Schall. The New Data Acquisition System at GSI. *IEEE Trans. Nucl. Sci.*, 43(1):132, 1996.

[Esse97] H.G. Essel, N. Kurz, W. Ott. Upgrades to the GSI Data Acquisition System MBS. *GSI Scientific Report 1996 GSI 98-1*, page 205, 1998.

[Esse98] H.G. Essel, N. Kurz. GSI Data Acquisition System MBS Version 3.0. *GSI Scientific Report 1998 GSI 99-1*, page 188, 1999.

[Esse00] H.G. Essel, N. Kurz. On-line Analysis in MBS 3.0. *GSI Scientific Report 2000 GSI 2001-1*, page 200, 2001.

[Esse01] H.G. Essel, N. Kurz. MBS Version 4.2 New Features. *GSI Scientific Report 2001 GSI 2002-1*, page 208, 2002.

[Eva65] D.S Evans. Low Energy Charged-Particle Detectors Using the Continuous-Channel Electron multiplier. *Rev. Sci. Instrum.*, 36(3):375, 1965.

[Fan01] S. Fan, A. Wagner, E. Grosse. Postneutron Yield of Bremsstrahlung-Induced Fission of ^{238}U with an Endpoint Energy of 12 MeV. *Wissenschaftlich-Technische Berichte FZR-319*, page 39, 2001.

[Fair06] An international Accelerator Facility for Beams of Ions and Antiprotons, Baseline Technical Report July 2006; http://www.gsi.de/fair/reports/btr.html

[Gabr00] F. Gabriel, P. Gippner, E. Grosse, D. Janssen, P. Michel, H. Prade, A. Schamlott, W. Seidel, A. Wolf, R. Wünsch, and ELBE-crew. The Rossendorf radiation source ELBE and its FEL project. *Nucl. Inst. Meth.*, B 161:1143, 2000.

[Gala71] M. Galanti, R. Gott, and J.F. Renaud. A High Resolution, High Sensitivity Channel Plate Image Intensifier for Use in Particle Spectographs. *Rev. Sci. Instrum.*, 42(12):1818, 1971.

[Gedk67] D.A. Gedke and W.J. McDonald. A constant fraction of pulse height trigger for optimum time resolution . *Nucl. Inst. Meth.*, 55(2):377, 1967.

[Gedk68] D.A. Gedke and W.J. McDonald. Design of the constant fraction of pulse height trigger for optimum time resolution. *Nucl. Inst. Meth.*, 58(2):253, 1968.

[Gira77] J. Girard and M. Bolore. Heavy ion timing with channel-plates. *Nucl. Inst. Meth.*, 140:279, 1977.

[Good62] G.W. Goodrich and W.C. Wiley. Continuous Channel Electron Multiplier. *Rev. Sci. Instrum.*, 33:761, 1962.

[Gues71] A.J. Guest. A computer model of channel multiplier plate performance. *Acta Electronica.*, 14:79, 1971.

[Heil85] R.D. Heil, J. Drexler, K. Huber, U. Kneissl, G. Mank, H. Ries, H. Ströher, T. Weber and W. Wilke. A compact Time-of-Flight spectrometer for electrofission studies. *Nucl. Inst. Meth.*, A 239:545, 1985.

[Henk78] P. Henkel, R. Roy and J. Wiza. High gain microchannel plates. *IEEE Trans. Nucl. Sci.*, NS-25:548, 1978.

[Iseg00] iseg Spezialelektronik GmbH; http://www.iseg-hv.de

[Kana69] M. Kanayama, T. Kono, and S. Kiyono. C-Al Parallel Plate Dynode Electron Multiplier. *Rev. Sci. Instrum.*, 40(1):129, 1969.

[Kimu00] K. Kimura, G. Andou, K. Nakajima. Surface-plasmon-assisted secondary-electron emission from an atomically flat LiF(001) surface. *Nucl. Inst. Meth.*, B 164-165:933, 2000.

[Klug07] J. Klug, E. Altstadt, C. Beckert, R. Beyer, H. Freiesleben, V. Galindo, E. Grosse, A.R. Junghans, D. Légrády, B. Naumann, K. Noack, G. Rusev, K.D. Schilling, R. Schlenk, S. Schneider, A. Wagner,F.-P.Weiss. Development of a neutron time-of-flight source at ELBE accelerator. *Nucl. Inst. Meth.*, A 577:641, 2007.

[Knol89] Glenn F. Knoll. *Radiation detection and measurement*. John Wiley and Sons, 1989.

[Kore00] http://www.kore.co.uk/mcp-faq.htm

[Kose02] K. Kosev, H. Sharma, A. Wagner. Measuring Foil Thicknesses for a Time-of-Flight Spectrometer . *Wissenschaftlich-Technische Berichte FZR-372*, page 39, 2003.

[Kose03] K. Kosev, A. Wagner, N. Nankov, K.D Schilling, H. Sharma. Test Measurements of Position-Sensitive Micro-Channel-Plate Detector. *Wissenschaftlich-Technische Berichte FZR-401*, page 21, 2004.

[Kose04] K. Kosev, N. Nankov, A. Wagner, E. Grosse, A. Hartmann, A.R. Junghans, K.D. Schilling, M. Sobiella. Position Resolution of a TOF Spectrometer for Photo-Fission Fragments and Beams of Exotic Nuclei. *Wissenschaftlich-Technische Berichte FZR-423*, page 24, 2005.

[Kose05a] K. Kosev, N. Nankov, M. Friedrich, E. Grosse, A. Hartmann, A.R. Junghans, K.D. Schilling, M. Sobiella, A. Wagner. First In-Beam MCP Detector Test Measurements. *Wissenschaftlich-Technische Berichte FZR-442*, page 14, 2006.

[Kose05b] K. Kosev, N. Nankov, M. Friedrich, E. Grosse, A. Hartmann, A.R. Junghans, K.D. Schilling, M. Sobiella, A. Wagner. Reconstructing the Secondary Electron Velocity Distribution Using the TOF Method. *Wissenschaftlich-Technische Berichte FZR-442*, page 16, 2006.

[Kose06] K. Kosev, N. Nankov, M. Friedrich, E. Grosse, A. Hartmann, K. Heidel, A.R. Junghans, K.D. Schilling, M. Sobiella, A. Wagner. Improving the Timing Properties of the Photo-Fission Setup. *Wissenschaftlich-Technische Berichte FZD-461*, page 53, 2007

[Kose07] K. Kosev, N. Nankov, M. Friedrich, E. Grosse, A. Hartmann, K. Heidel, A.R. Junghans, K.D. Schilling, R. Schwengner, M. Sobiella, A. Wagner. A high-resolution time-of-flight spectrometer with tracking capabilities for fission fragments and beams of exotic nuclei. *Nucl. Inst. Meth.*, A 594:178, 2008.

[Krug99] K. Kruglov, L. Weissman, P. Van den Bergh, A. Andreyev, M. Huyse, P. Van Duppen. A beam diagnostic system for low-intensity radioactive beams. *Nucl. Inst. Meth.*, A 441:595, 1999.

[Kuze00] A. V. Kuznetsov, E. J. van Veldhuizen, Lars Westerberg, V. G. Lyapin, K. Aleklett, W. Loveland, J. Bondorf, B. Jakobsson, H. J. Whitlow, M. El Bouanani. A compact Ultra-High Vacuum (UHV) compatible instrument for time of flight-energy measurements of slow heavy reaction products. *Nucl. Inst. Meth.*, A 452:525, 2000.

[Lanz03] G. Lanzanó, E.De Filippo, A. Anzalone, N. Arena, M. Geraci, F. Giustolisi, A. Pagano, H. Rothard, C. Volant. Recent results on fast intermediate velocity electron production induced by 19^+ 45 A MeV ^{58}Ni highly charged ions on thin solid targets . *Nucl. Inst. Meth.*, B 205:841, 2003.

[Leo94] W.R. Leo. *Techniques for Nuclear and Particle Physics Experiments A How to approach*. Springer-Verlag Berlin Heidelberg, 1994.

[Loty71] C. Loty. Saturation effects in channel electron multipliers. *Acta Electronica.*, 14:107, 1971.

[Luky86] S.M. Lukyanov, M. Lewitowicz, Yu.E. Penionzhkecich, G.G. Chubarian, D. Bazin, D. Guillemaud-Mueller, A.C. Mueller, M.G. Saint-Lauerent. Time-Zero Detector Based on Microchannel Plates and a Friable Dielectric Emitter. *JINR, Dubna*, E13-86-501, 1986.

[MBS] MBS DAQ; http://www-w2k.gsi.de/daq

[Meil75] W. Meiling. *Kernphysikalische Electronic*. Akademie-Verlag, Berlin, 1975.

[Milt62] J.C.D. Milton and J.S. Fraser. *Time-of-Flight Fission Studies on* ^{233}*U,* ^{235}*U, and* $^{239}Pu.Can.J.Phys., 40 : 1626, 1962.$

[Mult05] Multichannel Plate FAQ; http://www.sciner.com/MCP/microchannel_plate_FAQ.htm

[Nank04a] N. Nankov, K. Kosev, A. Wagner, K.D. Schilling, A. Hartmann,A.R. Junghans, M.Sobiella. Calculations for the Optimisation of the Time and Space Resolution of an Electrostatic Mirror. *Wissenschaftlich-Technische Berichte FZR-423*, page 25, 2005.

[Nank04b] N. Nankov, K. Kosev, A. Wagner, K.D. Schilling, A. Hartmann,A.R. Junghans, M.Sobiella. Efficiency of the Time-od-Flight Detector for Photo-Fission Fragments. *Wissenschaftlich-Technische Berichte FZR-423*, page 26, 2005.

[Nank05] N. Nankov, M. Friedrich, A. Hartmann,A.R. Junghans, K. Kosev, K.D. Schilling, A. Wagner. Energy distribution of Secondary Electrons by Swift Heavy Ions in Thin foils. *Wissenschaftlich-Technische Berichte FZR-442*, page 15, 2006.

[Odl96] O.H. Odland, W. Mittig, A. Lépine-Szily, G. Fremont, M. Chartier, M. MacCormick,J.M.Casandjian. A fast position sensitive microchannel plate detector for ray-tracing of charged particles. *Nucl. Inst. Meth.*, A 378:149, 1996.

[Oed80] A. Oed and P. Geltenbrot, R. Brissot, F. Gönnenwein and P. Perrin, E. Aker and D. Engelhardt. A mass spectrometer for fission fragments based on time-of-flight and energy measurements. *Nucl. Inst. Meth.*, 219:569, 1984.

[Orte98] *Modular Pulse-Processing Electronics*. ORTEC, 1997/98.

[Pare75] F. Paresce. Quantum efficiency of a channel electron multiplier in the far ultraviolet. *Appl. Optics.*, 14:2823, 1975.

[Paus00] G. Pausch, H. Prade, M. Sobiella, H. Schnare, R. Schweneger, L. Käubler, C. Borcan, H.G. Ortlepp, U. Oehmichen, H. Grawe, R. Schubart, J. Gerl, J. Cederkäll, A. Johnson, A. Kerek, W. Klamra, M. Moszyński, D. Wolski, M. Kapusta, A. Axelsson, M. Weiszflog, T. Härtflein, D. Pansergrau, G.de Angelis, S. Ashrafi, A. Likar, M. Lipoglašek. RoSiB - a 4π silicon ball for charged-particle detection in EUROBALL . *Nucl. Inst. Meth.*, A 443, 2000.

[Pfer77] K.E. Pferdekämper and H.-G. Clerc. Energy Spectra of Secondary Electrons Ejected by Ions from Solids. *Z. Physik*, A 280:155, 1977.

[Phil00] Philips Scientific; http://www.phillipsscientific.com

[Phot00] Photonis Group; http://www.photonis.com

[Poll84] E.C. Pollacco, J.C. Jacmart, Y. Blumenfeld, Ph. Chomaz, N. Frascaria, J.P. Garron and J.C. Roynette. A compact gridless channel plate detector for time-of-flight measurements. *Nucl. Inst. Meth.*, 225:51, 1984.

[Pome94] S. Pomme, E. Jacobs, M. Piessens, D. De Frenne, K. Persyn, K. Govaert, M.-L. Yoneama . Fragment characteristics for the photofission of ^{238}U with 6.1-13.1 MeV bremsstrahlung. *Nuclear Physics*, A 572:237, 1994.

[Roen00] RoentDek GmbH; http://www.roentdek.com

[Riva03] R.D. Rivarola, P.D. Fainstein. Electron emission in collisions of highly charged ions with atoms and diatomic molecules. *Nucl. Inst. Meth.*, B 205:448, 2003.

[Saro96] Šaro, S. Hofmann, H. Folger, F.P. He, V. Ninov, H.J. Schött, A.P. Kabachenko, A.G. Popeko, A.V. Yeremin. Large size foil-microchannel plate timing detectors. *Nucl. Inst. Meth.*, A 381:520, 1996.

[Scha74] P. Schagen. *Advances in image pick-up and display, vol.1*. Academic Press, New York, 1974.

[Schm66] K.C. Schmidt and C.F. Hendee. Continious channel electron multiplier operated in the pulse saturated mode. *IEEE Trans. Nucl. Sci.*, NS-13:100, 1966.

[Schu04] B.Schürmann. *Grundlagen der Rechnerkommunikation*. Friedr. Viewig Sohn Verlag/GWV Fachverlage GmbH, Wiesebaden, 2004.

[Schi02a] K.D. Schilling, F. Dönau, L. Käubler, A. Wagner, W. Neumann, Th. Riedel, and R. Schlenk. Bremsstrahlung Collimator for the NRF Set-Up at ELBE. *Wissenschaftlich-Technische Berichte FZR-341*, page 37, 2002.

[Schi02b] K.D. Schilling, A. Wagner, F. Dönau, L. Käubler, R. Schwengner, W. Neumann, and R. Schlenk. Beam Shutter and Hardener for the NRF Set-Up at ELBE. *Wissenschaftlich-Technische Berichte FZR-341*, page 41, 2002.

[Schi03a] K.D. Schilling, F. Dönau, E. Grosse, L. Käubler, R. Schwengner, A. Wagner, B. Wustmann, U. Lehnert, A. Nowak, B. Rimarzig, and R. Schlenk. Radiator for the Production of Bremsstrahlung at ELBE. *Wissenschaftlich-Technische Berichte FZR-372*, page 30, 2003.

[Schi03b] K.D. Schilling, U. Lehnert, F. Herbrand, R. Schwengner, A. Wagner, B. Caspar, M. Langer, T. Riedel, and A. Wagner II. Steering Magnets for the Production of Polarized Bremsstrahlung at ELBE. *Wissenschaftlich-Technische Berichte FZR-372*, page 31, 2003.

[Schw01a] P. Scwartze, H. Baumgärtel, and C.G.Eisenhardt. A simple and fast transimpedance amplifier for microchannel plate detectors. *Rev. Sci. Instrum.*, 72(7):3125, 2001.

[Schw02] R. Schwengner, H. Sharma, and A. Wagner. A Polarisation Monitor for Experiments with Bremsstrahlung at ELBE. *Wissenschaftlich-Technische Berichte FZR-341*, page 39, 2002.

[Schw05] R. Schwengner, R. Beyer, F. Dönau, E. Grosse, A. Hartmann, A.R. Junghans, S. Mallion, G. Rusev, K.D. Schilling, W. Schulze, and A. Wagner. The photon-scattering facility at the superconducting electron accelerator ELBE. *Nucl. Inst. Meth.*, A 555:211, 2005.

[Shar02a] H. Sharma, A. Wagner, E. Grosse. Simulations for a Double-Time-of-Flight Spectrometer for Fission Fragments . *Wissenschaftlich-Technische Berichte FZR-372*, page 36, 2003.

[Shar02b] H. Sharma, K. Kosev, A. Wagner, K.D. Schilling, A. Wagner II, W. Schulze, K. Heidel. A Time Coincidence Test Setup for an MCP Detector. *Wissenschaftlich-Technische Berichte FZR-372*, page 37, 2003.

[Shar02c] H. Sharma, K. Kosev, A. Wagner, K.D. Schilling, M. Sobiella, K. Kanaki. Secondary Electron Trajectories for an Electrostatic Mirror. *Wissenschaftlich-Technische Berichte FZR-372*, page 38, 2003.

[Shar04b] H. Sharma, K. Kosev, S. Fan, E. Grosse, A. Hartmann, A.R. Junghans, K.D. Schilling, M. Sobiella, A. Wagner. Planned Photofission Experiments at the New Elbe Accelerator in Rossendorf. *Seminar on Fission,Pont d Oye V-2003* ,edited by C.Wagemans et al., World Scientific, Singapore, page 201, 2004.

[Shif51] L.I. Schiff. Energy-Angle Distribution of Thin Target Bremsstrahlung. *Phys. Rev. 83*, page 252, 1951.

[Simi00] D.A. Dahl, SIMION 3D; http://www.simion.com

[Some69] T.A. Somer and P.W. Graves. Spiraltron Matrices as windowless photon detectors for soft x-ray and extreme UV. *IEEE Trans. Nucl. Sci.*, NS-16:376, 1969.

[Srim00] SRIM-2003; http://www.srim.org

[Tatr69] B. Tatry, J.M. Bosqued and H. Reme. Characteristics of electron multipliers used as detectors for low energy protons. *Nucl. Inst. Meth.*, 69(2):254, 1969.

[Timo74] J.G Timothy. Preliminary results with saturable microchannel array plates. *Rev. Sci. Instrum.*, 45(6):834, 1974.

[Timo77] J.G Timothy. Preliminary results with saturable microchannel array plates employing curved microchannels to inhibit ion feedback. *Rev. Sci. Instrum.*, 48:292, 1977.

[Vari00] Varian,Inc; http://www.varianinc.com

[Vitr00] Vitronit©; http://www.vitron.deA-3D

[Vita00] VITA; http://www.vita.com

[VME85] *VMEbus Specification Manual.* Revision C, 1985.

[Wagn99] A. Wagner, F. Dönau, E. Grosse, L. Käubler, K.D. Schilling, H. Schnare, and R.Scweneger. Considerations for the Bremsstrahlung-Photon Radiator at ELBE. *Wissenschaftlich-Technische Berichte FZR-271*, page 33, 1999.

[Wagn01a] A. Wagner, F. Dönau, E. Grosse, L. Käubler, K.D. Schilling, R. Schwengner, and W. Schulze. A Beam Dump for Energetic Photons. *Wissenschaftlich-Technische Berichte FZR-319*, page 40, 2001.

[Wagn05a] A. Wagner, R. Beyer, M. Erhard, F. Dönau, E. Grosse, A. Hartmann, A.R. Junghans, L. Käubler, K. Kosev, S. Mallion, C. Nair, N. Nankov, G. Rusev, K.D. Schilling, W. Schulze and R.Scweneger. The new bremstrahhlung facility at the superconducting electron accelerator ELBE. *J.Phys.(London) G*, S 1969:1972, 2005.

[Wagn05b] A. Wagner; http://www.fz-rossendorf.de/pls/rois/Cms?pOid=14474&pNid=212

[Whit91] Harry J. Whitlow, Bo Jakobsson and Division Lars Westerberg. Mass resolution of recoil fragment detector telescopes for 0.005-05 A MeV heavy recoiling fragments. *Nucl. Inst. Meth.*, A 310:636, 1991.

[Wiza79] J.W. Wiza. Microchannel plate detectors. *Nucl. Inst. Meth.*, 162:587, 1979.

[Wran04] J. Wranovics. VME:The military system stalwart adapts to address new trends. *VMEbus Systems.*, 22(4):42, 2004.

[Wurz94] P. Wurz and L. Gubler. Impedance-matching anode for fast timing signals. *Rev. Sci. Instrum.*, 65(4):871, 1994.

[Ydu96] Y. Du, H.G. Essel, F. Humbert, N. Kurz, W. Ott. Multi-Layer Multi-Branch Data Acquisition System MBS. *GSI Scientific Report 1996 GSI 97-1*, page 183, 1997.

Acknowledgement

First of all, I want to convey my thanks to Prof. E. Grosse and Dr. A. Wagner for giving me the opportunity to join the Nuclear Physics Group of the Institute of Radiation Physics of Research Center Dresden-Rossendorf.

My special thanks go to my colleagues from the Nuclear Physics group for the continuous support and fruitful working atmosphere.

In particular I wish to express my gratitude to Dr. A. Wagner who introduced me to details of different experimental techniques and supervised my work closely. I am also especially grateful for the initial support and encouragement given to me by Dr. H. Sharma. I thank to him, Dr. K. D. Schilling and Dr. R. Schwengner for useful discussions and cooperation.

Many thanks go to A. Hartmann, K. Heidel and M. Sobiella for the technical assistance.

I would like to acknowledge the colleagues from the Institute of Ion Beam Physics and Material Research for giving me the opportunity to perform experiments at the FZ Dresden-Rossendorf 5 MV tandem accelerator. Special thanks go to the accelerator crew for the smoothly running machine.

I am grateful to all my colleagues from the Institute for Radiation Physics who shared with me the shifts during the first photo-fission experiments at the ELBE accelerator.

I would also like to thank to the system administrators Dr. M. Schlett and J. Steiner and all the other people who helped me with my work.

Finally, I want to address my thanks to my family, relatives and friends for their love and encouragement.

Declaration

The work described here is all my own, except where clear reference is made to the work by others. The work in here has not been submitted for a degree, diploma or any other qualification to this or any other university.

Krasimir Milchev Kosev

Dresden
December 2007

Erklärung

Hiermit versichere ich, dass die vorliegende Arbeit ohne unzulässige Hilfe Dritter und ohne Benutzung anderer als der angegebenen Hilfsmittel angefertigt habe. Die als fremde Quellen direkt oder indirekt übernommenen Gedanken sind als solche kenntlich gemacht. Die Arbeit wurde bisher weder in Inland noch im Ausland in gleicher oder ähnlicher Form einer anderen Prüfungsbehörde vorgelegt. Die vorliegende Arbeit wurde am Forschungszentrum Dresden-Rossendorf unter der wissenschaftlichen Betreuung von Prof. E. Grosse und Dr. A. Wagner angefertigt.

Krasimir Milchev Kosev

Dresden,
den 18. December 2007